A STUDY ON THE FRAGILITY MODELING OF MID-RISE TUNNEL FORM RC BUILDINGS FOR TURKEY

by

Uğur Özen

B.S., Civil Engineering, Sakarya University, 2016

Submitted to the Kandilli Observatory and Earthquake

Research Institute in partial fulfillment of

the requirements for the degree of

Master of Science

Graduation Program in Earthquake Engineering

Boğaziçi University

2021

ACKNOWLEDGEMENT

Firstly, I would like to express my gratitude towards my supervisor Prof. Dr. Sinan Akkar for his guidance and support during my research. I gained valuable experience both in the academic field and in professional life during this dissertation. I could not complete this study without his patience and encouragement.

I also would like to thank my colleagues Mr. Haris Curic and Mr. Çağrı Dikmen for their collaboration and experiences during this research.

My special thanks to ER&E Inc and its associates to provide both moral and material supports during my studies.

Finally, my gratitude goes to my family and my friends who always encourage and support me.

ABSTRACT

A STUDY ON THE FRAGILITY MODELING OF MID-RISE TUNNEL FORM RC BUILDINGS FOR TURKEY

The mid-rise tunnel form RC buildings in metropolitan cities in Turkey and their dynamic behavior against earthquake action are investigated by deriving a representative model. First of all, the compiled blueprints of the tunnel form RC building inventory are categorized into four different groups and their fundamental features are studied statistically. The first group, which is the focus of this study represents general features of mid-rise tunnel form buildings in Turkey. Secondly, the nonlinear structural model of this building is developed based on the code requirements and guidelines to perform push-pull and pushover analysis for obtaining its simplified SDOF version in the MSc thesis of Curic (2021). The results of these two theses will complete and augment each other in a near-future collaborative work. Then, the ground motions selected and scaled to the target conditional-response spectra developed in Curic (2021) are used together with the provisions in the 2018 Turkish Building Earthquake code, 2004 Eurocode, and 2017 ASCE code to assess the structural performance of the model building (through damage states) for developing fragility curves. The observations from this study show that the performance of mid-rise tunnel form buildings can be called as satisfactory under the requirements dictated by the national and international standards. Another observation is that different engineering demand parameters give different performance assessment results. Hence, novel global and local performance demand parameters should be investigated by studying other categories (mid- and high-rise) tunnel form buildings. The variabilities in (1) engineering demand parameters, (2) structural properties such as story number, types of vertical elements, and mathematical model, and (3) the definition of limit states in both local and global performance levels have a significant effect on the fragility curves. These variabilities are taken into account for performance-based assessment.

ÖZET

TÜRKİYE’DEKİ ORTA KATLI TÜNEL KALIP BİNALARININ KIRILGANLIK EĞRİLERİNİN MODELLENMESİ ÜZERİNE ÇALIŞMA

Türkiye’deki büyükşehirlerde yapılan orta-katlı tünel kalıp binalar ve bu binaların deprem kuvvetlerine karşı dinamik davranışlarını temsil edebilecek benzeri bir model türetilerek incelenmiştir. Öncelikle tünel kalıp tipindeki betonarme yapı stoku planları derlenerek dört farklı gruba ayrılmış ve temel özellikleri istatistiksel olarak incelenmiştir. Bu çalışmanın odak noktasını oluşturan birinci grup, Türkiye'deki orta katlı tünel kalıp binaların genel özelliklerini temsil etmektedir. İkinci olarak, bu binanın doğrusal olmayan yapısal modeli, kod gereksinimleri ve standartların önerilerine bağlı olarak geliştirilerek, Curic (2021) yüksek lisans tezinde basitleştirilmiş SDOF sistem elde etmek amacıyla itme-çekme ve itme analizleri yapıldı. Bu iki tezin sonuçları, ortak bir çalışmada birbirini tamamlayacak ve gelecekte yapılacak olan çalışmaları da artıracaktır. Kırılganlık eğrilerinin elde edilmesinde (hasar durumları aracılığıyla), Curic (2021) tarafından geliştirilen yer hareketlerinin koşullu spektrumlara bağlı olarak seçilmesi ve ölçeklendirilmesi, model binanın yapısal performansını değerlendirmek için 2018 Türkiye Bina Deprem yönetmeliği, 2004 Avrupa ve 2017 Amerikan standartlarındaki gereksinimlerle birlikte kullanılmıştır. Bu çalışmadan elde edilen gözlemler orta-katlı tünel kalıp binaların performansının ulusal ve uluslararası standartlar tarafından belirlenen gereksinimler altında memnun edici sonuçlar vermektedir. Başka bir gözlemde, farklı mühendislik parametrelerinin farklı performans değerlendirme sonuçları vermesidir. Bu nedenle, yeni global ve yerel performans parametreleri, diğer kategorilerdeki (orta ve yüksek katlı) tünel kalıp binaları incelenerek araştırılmalıdır. Mühendislik talep parametrelerindeki farklılıklar (1), kat sayısı, düşey eleman türleri ve matematiksel model gibi yapısal özellikleri etkileyen değişiklikler (2) ve hem yerel hem de global performans seviyelerinde sınır durumlarının tanımındaki değişkenler (3), kırılganlık eğrileri üzerinde önemli bir etkiye sahiptir. Bu değişkenler performansa dayalı değerlendirmelerde göz önüne alınmalıdır.

TABLE OF CONTENTS

LIST OF FIGURES

LIST OF TABLES

LIST OF SYMBOLS

Ag	Gross cross-section area
fc	compressive strength of concrete
fsy	Yield strength of reinforcing steel
fu	Specified ultimate tensile strength of reinforcing steel
fy	Nominal yield strength of reinforcing steel
G	Dead loads
Gc	Shear modulus
Ig	Gross moment of inertia
lw	Width of a shear wall cross-section
Pu	Axial load on the wall
Q	Live loads
Sa	Spectral acceleration
$Sa(Ti)$	Spectral acceleration at i'th period
T_{1x}	1st mode period in translational x-direction
T_{1y}	1st mode period in the translational y-direction
Tn	Nth mode period
v_{cr}	Cracking strength
v_n	Nominal shear strength
V	Shear force
V_{cr}	Cracking strength in force units
V_n	Ultimate shear force
Vr	Residual strength
V_{s30}	The average shear-wave velocity
Vy	Yield strength
W	Total weight of the structure
γ_{cr}	Cracking shear strain
γ_y	Yield shear strain
ε_c	Concrete Strain
ε_s	Reinforcing steel strain
μ	Mean value
ν	Poisson ratio
σ	Standard deviation

LIST OF ACRONYMS/ABBREVIATIONS

ACI	American Concrete Institute
ASCE	American Society of Civil Engineers
ATC	Applied Technology Council
AvgSA	Average Spectral Acceleration
CD	Controlled Damage
CP	Collapse Prevention
CS	Conditional Spectrum
DCE	Design Considered Earthquake
DL	Damage Limitation
DS_1	Damage State 1
DS_2	Damage State 2
DS_3	Damage State 3
EC	European Code
EDF	Energy Dissipation Factor
EDP	Engineering Demand Parameter
F-D	Force-Deformation
GMPE	Ground Motion Prediction Equation
GW	General Wall
H1	Horizontal Direction 1
H2	Horizontal Direction 2
IDA	Incremental Dynamic Analysis
IDR	Interstory Drift Ratio
IM	Intensity Measure
IO	Immediate Occupancy
LATBSDC	Los Angeles Tall Buildings Structural Design Council
KOERI	Kandilli Observatory Earthquake Research Institute
LD	Limited Damage
LS	Life Safety
MCE	Maximum Considered Earthquake
MDOF	Multiple Degree of Freedom
MEU	Ministry of Environment and Urbanisation
MIDR	Maximum Interstory Drift Ratio
M-K	Moment Curvature

MSA	Multiple Stripe Analysis
MVLEM	Multiple Vertical Line Element Model
NEHRP	National Earthquake Hazards Reduction Program
NC	Near Collapse
NRHA	Nonlinear Response History Analysis
NSP	Nonlinear Static Procedure
PBEE	Performance Based Earthquake Engineering
PEER	Pacific Earthquake Engineering Research
PGV	Peak Ground Velocity
RC	Reinforced Concrete
SD	Significant Damage
SDOF	Single Degree of Freedom
SFI-MVLEM	Shear-Flexure Interaction Model
SPO	Static Pushover
SW	Shear Wall
TBSDC	Turkish Building Seismic Design Code
3D	Three Dimensional

1 INTRODUCTION

1.1 General

The majority of the population is located in metropolitan cities in Turkey such as Istanbul, Ankara, and Izmir. The population increase leads to rapid increase in newly built environments. To this end, reinforced concrete (RC) frame buildings are the most common built environment in Turkish construction practice. Another commonly used structural type is the tunnel form buildings due to their practical aspects in terms of construction time and low construction costs.

The shear walls are the main lateral as well as vertical load resisting systems in tunnel form buildings. The shear walls, as vertical structural components, are quite effective (as well as efficient) against lateral earthquake loads. Regular geometric plans of tunnel form buildings, decrease in construction time, and lesser need of skilled labour due to readily available scaffolding to assemble the construction site are the appeals in tunnel form buildings. The major objective of this dissertation is to develop the structural fragility function of mid-rise tunnel form buildings against earthquake action by considering the record-to-record variability.

A study of tunnel form building inventory is statistically investigated to define a representative model of mid-rise tunnel form building inventory in Turkey. The available data provided by the Kandilli Observatory Earthquake Research Institute (KOERI), and the Ministry of Environment and Urbanisation (MEU) are considered in this study. A total of 16 tunnel form buildings exists in the database (including 42 stories tunnel form tall building, disregarded the scope of this study). The database of inventory (see Table 1.1) includes several pieces of information regarding:

- Project names,
- Number of stories,
- Plan dimensions,
- Typical span,
- Member section dimensions (Beams, Shear wall, and Slab Thickness)
- Slab system

- Design parameters,
- Beam reinforcement ratios
- Shear wall reinforcement ratios and total shear wall areas in both directions.

Table 1.1 The tunnel form building inventory focussed on this study. (The database of KOERI and MEU)

Database	#	Building	#Story	Area (m^2)	Construction Year
KOERI	1	Ramazanoglu Apt	10	230.9	2013
	2	Bahcesehir Hill park Konutları - Blok A&D	6	384.2	2011
	3	Bahcesehir Hill park Konutları - Blok B&C	6	384.2	2011
	4	Esenyurt	15	434.8	2011
	5	Hadımkoy 2. Etap Konut, E Blokları	16	384.2	2010
	6	Hadımkoy 2. Etap Konut, F Blokları	17	552.3	2010
	7	Mısırlı	15	295.9	2015
	8	Soyak Halkalı, A blok	17	621.8	2011
	9	Soyak Halkalı, B blok	11	730.1	2011
	10	Soyak Halkalı, C blok	7	730.1	2011
	11	Bahcesehir Hillpark Konutları - Blok G	6	480.2	2011
	12	Bahcesehir Hillpark Konutları - Blok H	6	288.1	2011
MEU	13	Incek 1.Etap tip 1	25	993.6	2010
	14	Incek 1.Etap Tip 3	21	924.2	2010
	15	Incek 2. Etap Tip 1	14	699.1	2014

This dissertation will study the development of the structural fragility of mid-rise tunnel form buildings in Turkey. To this end, this report is configured such that Chapter 1 summarizes the survey about tunnel form building inventory, Chapter 2 provides the structural modeling information based on the provisions of codes and guidelines, and Chapter 3 covers the performance assessment criteria under different codes provisions. This study has also collaborated with Curic study (2021), his study, briefed in Chapter 4, includes probabilistic seismic hazard assessment (PSHA). Nonlinear analyses are conducted using Perform 3D (2018) structural analysis program and structural responses are evaluated in

Chapter 5. Finally, the fragility curves, the main aim of this dissertation, are evolved in Chapter 6 and this study is summarized and concluded in Chapter 7.

1.2 Brief Inventory Information and the Model Representing the Mid-rise Tunnel Form Buildings in Turkey

The overall features of each category are discussed further in the next paragraphs of this section. The mean values of geometrical and structural components are used to establish a representative building model of each group. The first group (6-story, 18 m in height) among these categories in Table 1.2 is studied in detail in this thesis that represents the mid-rise tunnel form buildings in Turkish construction practice. The geometric of this model building plan is shown in Figure 1.1.

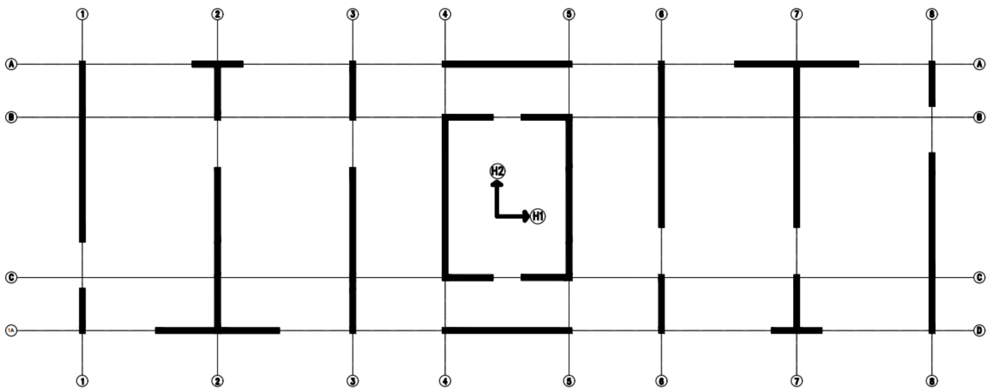

Figure 1.1 The idealized structural geometric plan

The tunnel form building inventory compiled from the databases of KOERI and MEU are investigated, and they are classified into four subgroups according to their story number (Table 1.2). The plan dimensions, longitudinal and lateral reinforcement ratios, and wall-to-floor area statistics of the buildings in these categories are also investigated.

Table 1.2 Categorization of building inventory according to story number and total building number in each category

Group	Story Number	Number of Buildings
S1	6 & 7 story buildings	5
S2	10 & 11 story buildings	2
S3	14,15,16 & 17 story buildings	4
S4	21 & 25 story buildings	2

The inventory tunnel form buildings considered in this study are shown in Table 1.1. The number of stories is compared to the number of buildings. Structural parameters are listed based on the knowledge of various information described in the previous section. Consequently, the representative model of mid-rise tunnel form in Turkey is built. Its properties and details are given in Table 1.3.

Table 1.3 The representative model of mid-rise tunnel form building

S1-Building	**Mean**	**Value accepted in the model**
Number of stories	6	6
Story Height (m)	2.99	3
Total Height (m)	18.5	18
Floor Plan Area (m^2)	453.4	453.4
Length in X Dir	37.7	37.7
Length in Y Dir	11.8	11.8
Slab Thickness (cm)	19	19
Beam (cm)	25x60	25X60
SW Thickness (cm)	23	25
Area of SWs in X Dir (m^2)	9.07	9
SW Moment of Inertia in X Dir. (m^4)	16.8	16.3
Area of SWs in Y Dir (m^2)	14.39	14.95
SW Moment of Inertia in Y Dir. (m^4)	57.5	56.2
Concrete Strength (MPa)	30	30
Reinforcing Steel Strength (MPa)	420	420

Eight different SWs pairs (a total of 16) are modeled based on the statistical information obtained from the compiled database. The SW's area and moment of inertia in Table 1.3 are considered in this study. The cross-section of SWs is modeled according to statistical investigation obtained from the database. The statistical investigation (Table 1.4) is conducted on horizontal and vertical reinforcement and stirrup spacing. The proposed shear wall reinforcement parameters are listed in Table 1.5

Table 1.4 The statistical data for SW Reinforcement

Shear Wall Reinforcement Ratio Statistics				
Parameters	**Confinement Region**	**Web**	**Stirrup Diameter/Spacing (cm)**	
Mean - μ	1.62%	0.72%	10	11
Standard Deviation - σ	0.28%	0.13%	0	2
CoV(%)	17.27	18.71	0	18.2

Table 1.5 Proposed SW Reinforcement for mid-rise tunnel form building in Turkey

Proposed Model Shear Wall Reinforcement Ratios					
Parameters		**Confinement Region**	**Web**	**Stirrup Diameter/Spacing (cm)**	
Minimum	μ - σ	1.34%	0.58%	10	15
Mean	μ	1.62%	0.72%	10	10
Maximum	μ + σ	1.90%	0.85%	10	5

The model building is assumed to be located in the Ataşehir district (40.98N, 29.13E) as the tunnel form buildings are quite dense in the residential and commercial areas in this district. Besides, this district is prone to high seismicity in Istanbul, which, as a city, is prone to severe earthquakes having characteristic magnitudes of Mw ~7 or above. As indicated, the tunnel form building stock increases day by day in this district, and hence it would be important to assess their seismic performance in terms of structural performance.

According to a study of IBB-KRADE (2020), the building types are categorized into three main groups based on their story number (see Table 1.6). There are more than 10000 tunnel form buildings in the entire İstanbul with different story numbers, and 603 of these buildings are in Ataşehir (see Table 1.7).

Table 1.6 The stock information according to story number in Ataşehir. (IBB-KRADE, 2020)

Site: Ataşehir		
Category	Number of Buildings	Percentage
1-4 Story	18774	68%
5-8 Story	7543	27%
9-19 Story	1266	5%

Table 1.7 The stock of buildings according to structure types in Ataşehir. (IBB-KRADE, 2020)

Structure Type	Number of Buildings	Percentage
Masonry	4235	15%
Concrete	22414	81%
Wood	22	0.3%
Steel	182	1%
Tunnel Form	603	2%
Prefabricated	127	0.7%

1.3 Literature Survey

Literature surveys in this study mainly focus on (1) the dynamic behaviour of tunnel form buildings, (2) the obtain information about IM-EDP pairs in terms of efficiency, practicality, and sufficiency, (3) analytical model of shear walls, and (4) development of analytical fragility curves. In this context, several studies from the literature are briefed in the next paragraph of this section.

Balkaya and Kalkan (2003) investigated multistorey tunnel form buildings. 80 different buildings are analyzed to assess their dynamic behavior and consistency of equations given by seismic codes. The results show that current seismic codes overestimate the analysis results more than finite-element analysis results. Another observation is that torsional mode has a significant effect on buildings rather than transitional modes. In another study (Balkaya and Kalkan, 2004)

The study of Yuksel and Kalkan (2006) investigated tunnel form buildings under quasi-static cyclic lateral loading. Two four-story buildings were analyzed. The material properties and reinforcement detailing in this study are identical to the buildings constructed in Turkey. The experimental and analytical results show that brittle failure may be observed in tunnel form buildings due to low reinforcement ratio

Beheshti-Aval et al. (2018) studied the effect of near and far fault ground motions on tunnel form building. The prototype plan of buildings consists of 5 and 10-story buildings as a residential building in the Tehran region. The analytical results based on IDA show that the tunnel form system has a high capacity in the seismic region subjected to far directivity near-fault ground motions. Moreover, the near-fault ground motions have a significant effect on taller tunnel form buildings. Coupling beams exceed their performance level before walls at lower performance points.

Mohsenian et al. (2021) studied the seismic performance assessment of tunnel form buildings. The buildings consist of 5 and 10-story buildings having a regular and symmetric plan. the fragility analysis is derived based on IDA results. The fragility results show that the mid-rise tunnel form buildings have higher capacity and strength. Another result is that the tunnel form building does not have significant damage under the DCE level.

The study of Kohrangi et all. (2016) states that an efficient IM leads to a decrease in dispersion. Moreover, a sufficient EDP reduces the number of analyses. AvgSA can be a good predictor for inter-story drift ratio due to the sensitivity of higher modes effects and capturing the nonlinear behavior.

The study of Xiao L et all. (2013) indicates that PGV, as IM, is the best indicator correlated with story drift ratio rather than the ones such as PGA and SA(T_1). PGV is also an efficient and sufficient IM which leads to reduce the dispersion of structural response when structure behavior is in a nonlinear region. Similarly, PGV can be selected as IM for a high-rise building affected directly by higher modes. It will provide efficiency and sufficiency in collapse analysis. Since the correlation between PGA and Sa(T_1) and IDR can reduce their effects, as the dominant period increases.

Based on the study of Eads et all. (2015) compares collapses by using AvgSa and Sa(T_1). This study offers that AvgSa is more sufficient and efficient predictor than Sa(T_1) while computing collapse risk estimation. AvgSa also captures structural response when including higher mode effects.

Hancılar and Caktı (2015) investigate which IM-EDP pairs are the best correlation. The study results show that the Sa(T_1)-MIDR pairs are more efficient than PGV in mid-rise buildings. PGV-MIDR pairs have a good correlation at mid-rise buildings and high-rise buildings. Sa(T_1) at high-rise buildings loses its efficiency compared to mid-rise buildings.

Bianchini et all. (2009) presents inelastic response using AvgSa. This study suggests that AvgSa is the best IMs compared to PGA which is variables and insufficient for scaling ground motions. AvgSa in all cases leads to low dispersion for the structure with short, medium, and large periods.

1.4 Objective and Scope

In the two last decades, the tunnel form structural type is the commonly used structural system. The building inventory numbers collected for Istanbul (IBB-KRADE, 2020) show that the tunnel form structural type is the commonly used structure after 2000 with the knowledge of construction and materials. Therefore, the rapid increase in newly built environments creates a new research interest and uncertainties. This study investigates these uncertainties and focuses on deriving fragility curves for a model that represents the mid-rise tunnel form building inventory in Turkey.

This dissertation aims to give information about (1) the tunnel form building inventory representative of Turkish construction practice and how they are categorized in terms of story number. The database of tunnel form building inventory which belongs to KOERI and MEU includes 15 representative building models. Most of the subject buildings are constructed after 2000 (see Table 1.1); (2) Perform 3D is selected to create a mathematical model. The lumped plasticity approach is considered to define the nonlinear behavior of beams whereas fiber-based analytical models are considered to mimic spread plasticity while modeling the SW elements. The nonlinear structural modeling techniques and the requirements dictated by codes and guidelines are taken into account in this study; (3) code-based nonlinear seismic performance assessment procedures are conducted. The simplified

SDOF model is derived by using the results of the push-pull analysis to capture cyclic degradation. The static pushover analysis is also conducted to define damage state limits based on code requirements because three different codes demand different demand parameters to assess structural performance; (4) this study collaborates with Curic (2021). PSHA study is performed in his study and ground motion selection and scaling are developed; Ataşehir district (40.98N, 29.13E) as the tunnel form buildings are quite dense in the residential and commercial areas in this district are selected and finally, (4) development of fragility curves for mid-rise tunnel form buildings representing the construction practice in Turkey are investigated. The variabilities which is the focus of this study directly have a significant effect on fragility curves. These variabilities can be summarized as

- engineering demand parameters,
- structural properties
- mathematical model’s approach
- the definition of limit states in both local and global performance levels

2 THE STRUCTURAL MODEL

2.1 Introduction

Nonlinear response history analysis (NRHA) is the preferred analysis type to assess the structural behaviour under earthquake loading. Its main goal is to simulate all significant modes of deformation and the onset of collapse under several ground-motion intensity levels. To achieve this, several modeling parameters such as selection of structural components, P-Delta effects, damping ratio, material properties, and consideration of modeling uncertainty in the above parameters (ATC-72, 2010) should be considered in structural modeling. In this thesis, mid-rise tunnel form buildings representing a frequently constructed residential building group in Turkey are modeled. The 6-story analytical model that represents the mid-rise tunnel form buildings is given in Figure 2.1. It is modeled by using Perform 3D V7.0.0 software package. (Computer and Structures, 2018).

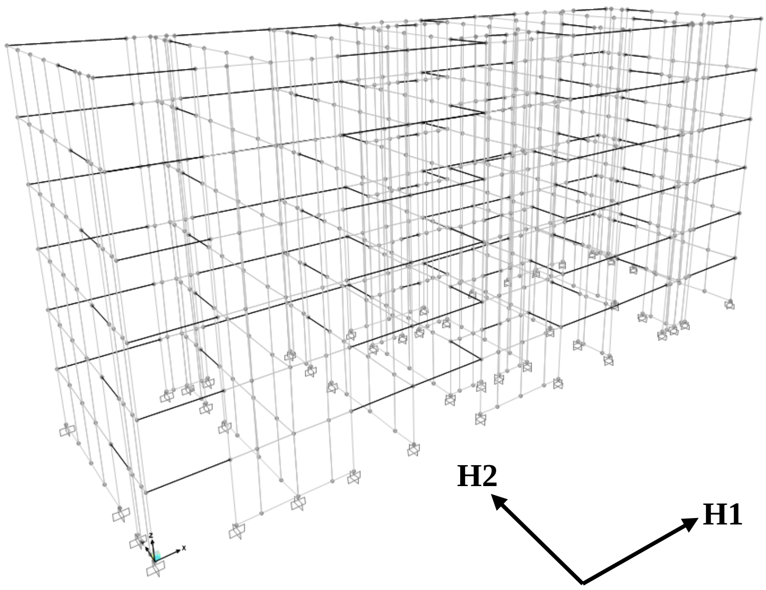

Figure 2.1: The representative analytical model of 6 stories

This chapter is associated with the design criteria of nonlinear structural behaviour and dynamic analysis of the model building. It begins with the nonlinear modelling definitions of materials and structural elements. The tunnel form buildings are composed of shear walls and beams to resist lateral loading. In other words, the analytical model in this study includes only shear wall (SW) and beam elements. The concrete and rebar strengths in the model are assumed from the design standards as there are no experimental results or specimens describing the actual expected strength levels of these materials. The lumped plasticity approach is considered to define the nonlinear behaviour of beams whereas fiber-based analytical models are considered to mimic spread plasticity while modelling the SW elements. P-Δ effects are taken into consideration in NRHA. The floor masses, as discussed in Section 2.3.1, are assigned as lumped masses at the floor centers. A concrete deck is assumed as a rigid diaphragm to model the floor without significant loss in accuracy. (PEER/ATC-72 ,2010). Hence, the nodes at each level are constrained by rigid diaphragms and the slabs are not modelled separately in the analytical model.

2.2 Types of Nonlinear Models

The lateral resisting system in this study consists of RC-SW and beam elements. The inelastic structural components can be idealized in several ways as presented in Figure 2.2. According to the tall building guidelines (NEHRP Tech Brief No:4, 2010), the inelastic component modelling requires a good understanding of its expected behaviour and it relies on reasonable assumptions and justifiable approximations. The plastic hinge model (Figure 2.2.a) is selected to model the beam element whereas the fiber section (Figure 2.2.d) is used in modeling of SW elements. The detailed information regarding modeling of elements is described in Section 2.2.1.

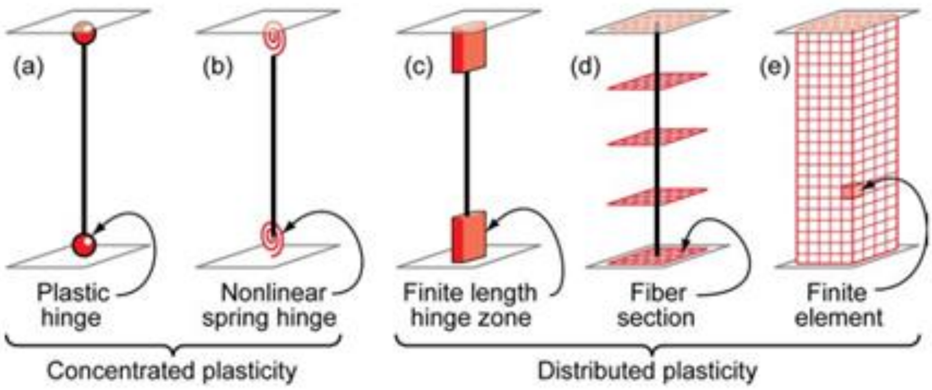

Figure 2.2: The idealized model of an inelastic structural component (NEHRP Tech. Brief No:4, 2010)

2.2.1 The Modeling of Structural Components

RC-SW is the main structural component in the tunnel form to resist lateral loads under different intensity levels. A-frame element is linked between SW elements and it aims to transfer gravity loads to the vertical elements.

2.2.1.1 Modeling of RC-SWs

Several inelastic mathematical models have been developed for RC-SWs. These models can be categorized into two groups: macroscopic and microscopic approaches according to their mathematical models. Gorgulu and Taskin (2015) compared these models with details so that the microscopic models such as finite element and multi-layer shell element are more comprehensive than macroscopic elements such as equivalent beam model and fiber type model. On the other hand, macroscopic models are preferable models over microscopic models due to computational time. Orakcal et al. (2004) indicated that a microscopic model gives more detailed information about the local response, however, this information is not beneficial in terms of efficiency and practicality in the analysis due to the increased complexity in the results.

The guideline of nonlinear structural analysis for seismic design (NEHRP Tech. Brief No:4, 2010) suggests that the fiber wall models can be more accurate than beam-column elements in capturing concrete cracking and steel yielding because the beam-column element models are not sensitive in 3D wall analysis. Therefore, the fiber element models are used to define the mathematical model of tunnel form building in this study.

The fiber element model depicted in Figure 2.3 consists of many uniaxial concrete and steel fibers, which take into consideration of fiber action that leads to the shifting of the neutral axis along the RC wall section throughout the analysis. One of the main issues in modeling fiber wall models is to capture shear-flexure interaction. Several fiber modelling approaches are performed to capture the shear-flexure interaction (Massone et all, 2006, Kolozvari et all., 2015). These models can be implemented in OpenSees software under earthquake loading.

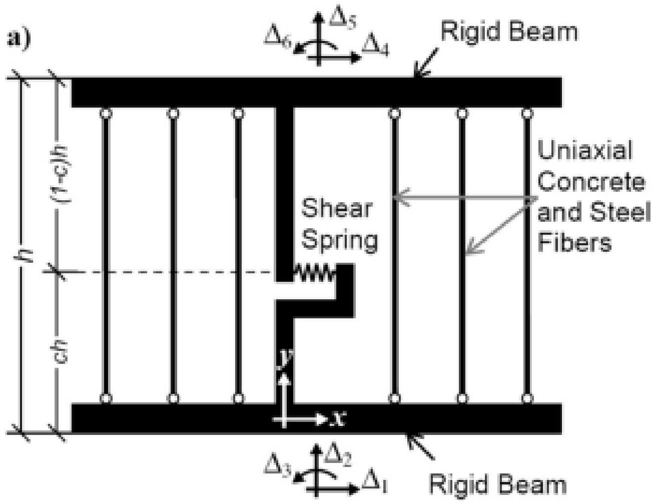

Figure 2.3: Analytical fiber wall element model (Kolozvari et all, 2018)

An experimental study conducted by Kolozvari et al. (2018) reveals that uncoupled shear-flexure interaction (Kolozvari et al., 2015) tends to overestimate the lateral load and lateral stiffness capacity when it is compared to coupled shear-flexure interaction (Kolozvari et al., 2015). Besides, the latter approach would be more accurate in results than the former approach. It should be noted that these models cannot capture failure modes resulting from buckling of reinforcing steel bars, lateral instability, and sliding shear failure along cracks.

To conclude, neither the above models nor the OpenSees software is used in the NRHA of the model building. Instead, the Perform 3D software is selected to perform NRHA that uses a hysteretic model disregarding the interaction between shear and flexure in the SW behaviour. Therefore, the accuracy of results from NRHA is limited to the modeling assumptions of Perform 3D. the following section explains the merits of the RC SW model used for modelling the model building.

In this study, RC-SWs are modelled as fiber elements of Perform3D structural analysis software because the fiber model is a reasonable alternative to capture the nonlinear behavior of walls under seismic loads. (Gorgulu and Taskin, 2015). The RC-SW model in Perform3D is divided into two models: general wall (GW) component and shear wall (SW) component. Their mathematical modelling features are shown in Figure 2.4.

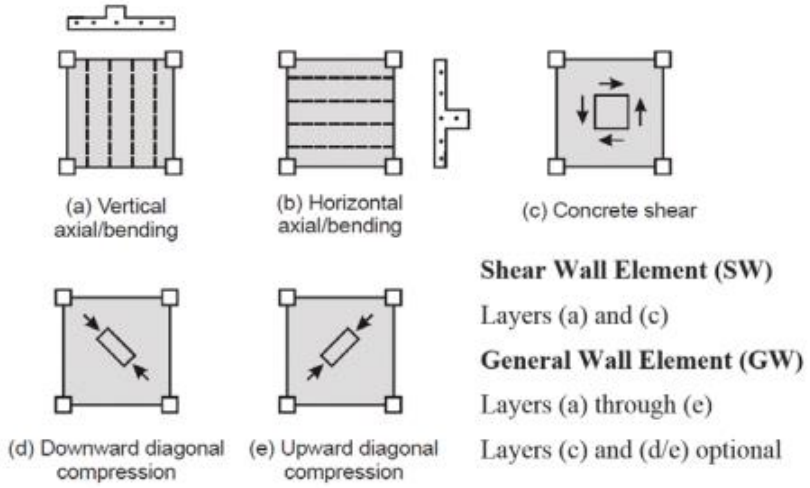

Figure 2.4: Mathematical Modelling of Wall Element in Perform 3D (Perform 3D User Manual, 2006)

GW element includes vertical and horizontal fibers (Figure 2.4a, b), which model the axial/bending behavior while SW element considers only vertical fibers (Figure 2.4a). Compared to SW element, GW element is more advantageous due to its complex formulation, however, SW element is the most used one in the analysis of SW systems as it is simple and reduces the computational effort. (Gorgulu and Taskin, 2015, Kolozvari et all, 2017, Lowes and Baker, 2018). The 6-story tunnel form building is designed by using the SW element in Perform 3D. The shear wall idealization of the cross-section used in the fiber model is depicted in Figure 2.5.

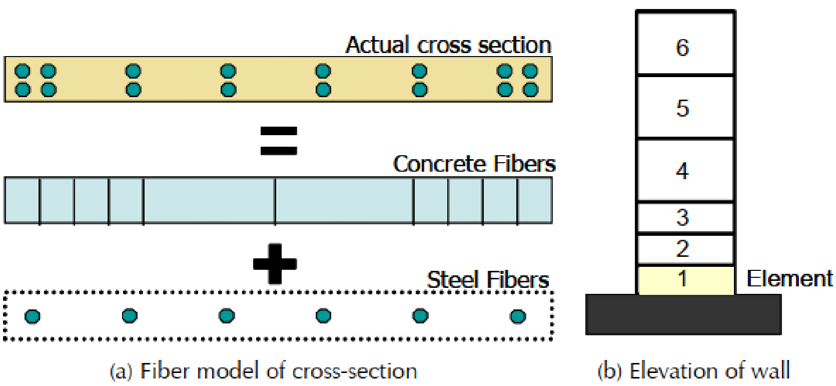

Figure 2.5: The idealization of fiber wall model (ATC 72, 2010)

The concrete fiber model (Figure 2.5) is grouped as confined and unconfined concrete materials. The constitutive models for concrete were developed many years ago. The modified Kent-Park model (Kent and Park, 1971) and Mander model (Mander et al, 1988) are the most widely used ones for the hysteretic behaviour of concrete. (Figure 2.6 a and b).

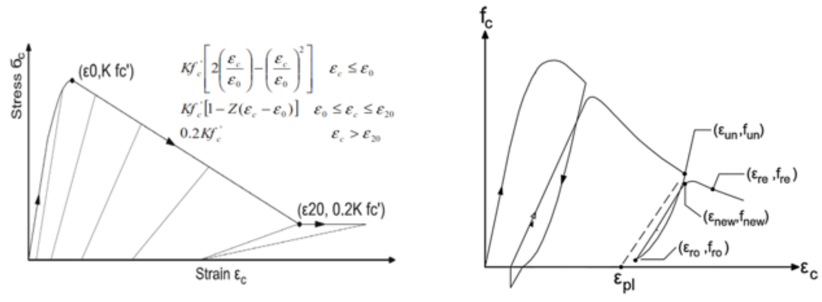

a) Modified Kent-Park constitutive model b) Mander model (Mander et al. 1988)

Figure 2.6: Concrete Constitutive Model

The hysteric Mander model (Mander et al, 1988) for confined and unconfined concrete is adopted in the building model. The model is fit as a tri-linear stress-strain relationship based on the cross-section of the shearwall. The expected compressive stress is taken as 30 MPa (nominal) and it is based on the national regulations as no experimental results are available about the concrete strength in the tunnel form RC building inventory.

The concrete constitutive model is generated according to the rules given in the Mander model (Mander et al, 1988). The idealization of the concrete model in Perform 3D is illustrated in Figure 2.7. The detailed nonlinear modeling parameters are given in Appendix A.

a

b

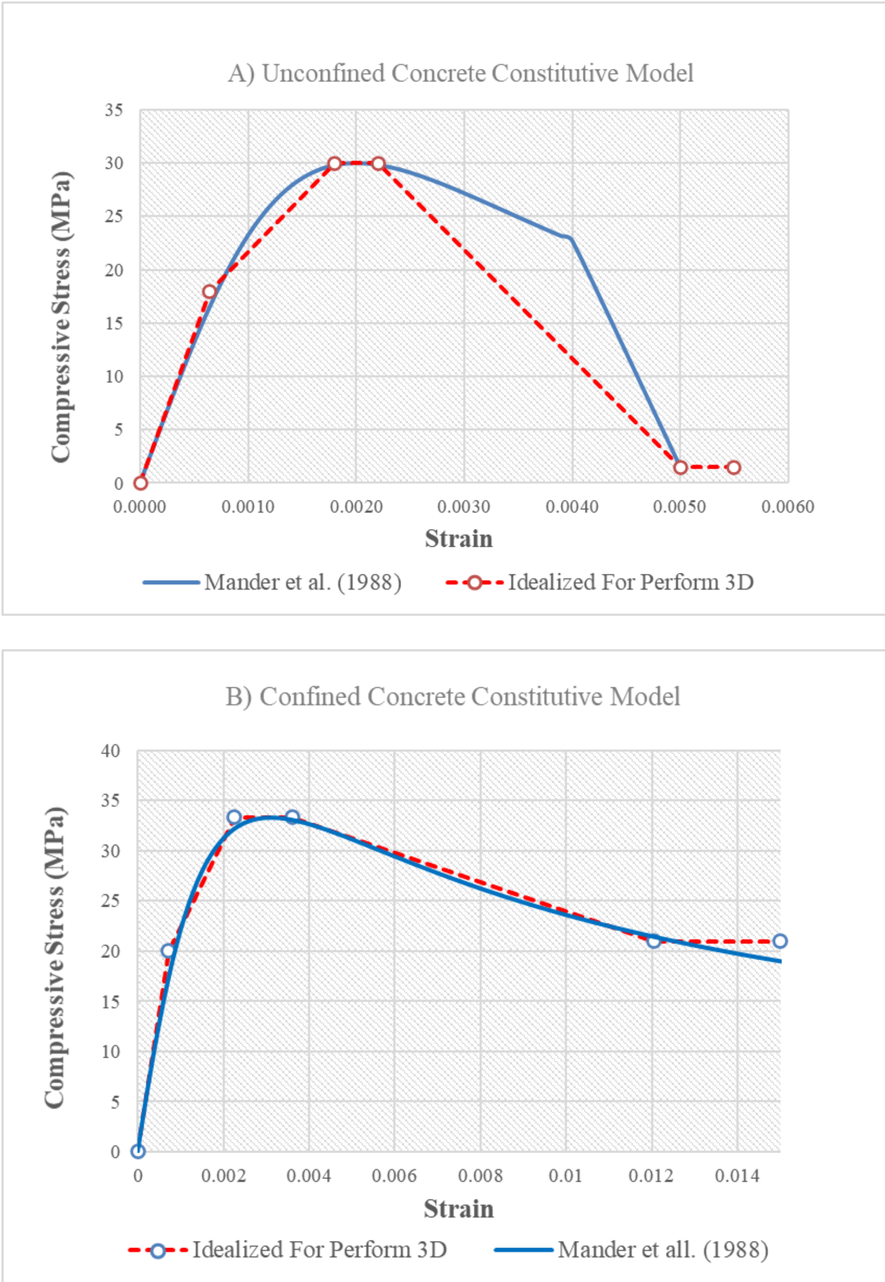

Figure 2.7: a) Unconfined concrete model, b) Confined concrete model (6-story tunnel form building)

Another important criterion that affects the dissipated (hysteretic) energy is cyclic deterioration. ATC 72-1 (2010) defines cyclic deterioration as the strength and stiffness reduction resulting from compound damages. The monotonic backbone curve representing the inelastic behavior is calibrated by the energy dissipation factor (EDF) to take into account the stiffness and strength degradation. The calibration factor EDF should be compatible with the experimental results.

Many researchers study to calibrate EDF. (Gorgulu and Taskin, 2015; Kolozvari et all, 2017 and Lowes and Baker, 2018). In essence, the EDF calibrates the labeled points shown in Figure 2.8 depending on the experimental results.

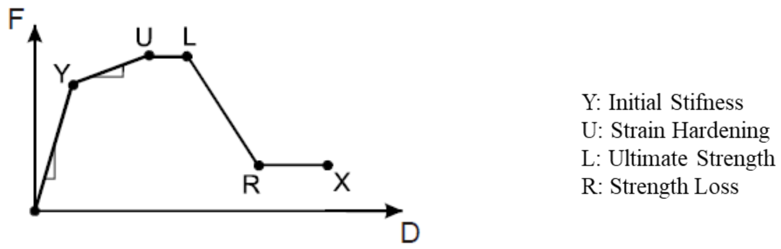

Figure 2.8. Energy Dissipation Factor Points (Perfom3D User Guide, 2006)

The EDF calibration proposed in Gorgulu and Taskin (2015) is adopted in this research. Their study calibrates EDF by performing a series of experimental tests and numerical analyses in Perform 3D. They use an RC infill wall model which is modeled as a fiber model. The modification factors are illustrated in Figure 2.9a.

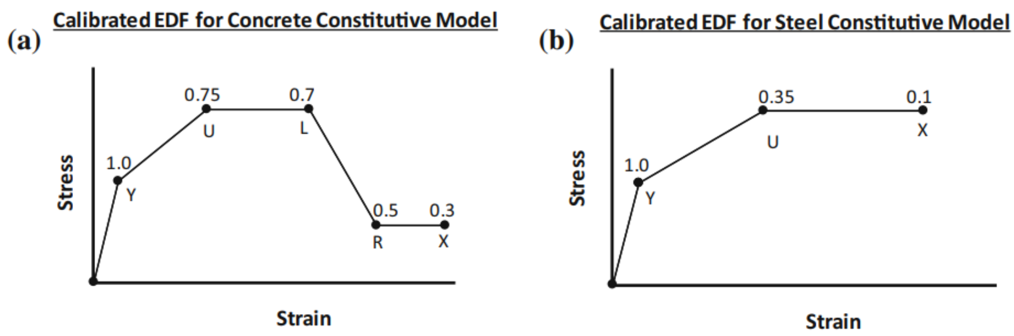

Figure 2.9: Energy Dissipated Factor a) Concrete b) Steel (Gorgulu and Taskin, 2015)

The cyclic behavior of steel is modeled by using the stress-strain relationship (Figure 2.10) proposed by Menegotto and Pinto (1973) and developed by Filippou et al. (1983). It is a widely used hysteric model to capture the cyclic reinforcement behavior under earthquake loading. The calibrated EDP for the steel constitutive model is once again adopted from Gorgulu and Taskin (2015) and the modification factors are shown in Figure 2.9b. The details of steel hysteric behavior are shown in Appendix A.

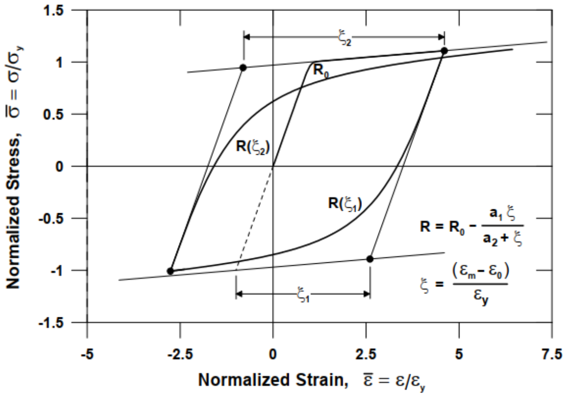

Figure 2.10. Reinforcing steel model (Menegotto and Pinto, 1973)

The shear stress-strain relationship in this study is represented by two alternative models and they are used separately in two different model buildings (Model 1 and Model 2). The shear stress relationship is modeled as linearly elastic in Model 1 by considering the Eurocode8 (2005; EC8-3) and Turkish Building Earthquake Code (2018; TBSDC-18). In this model, the shear limit of the structure is controlled by the expression (V_n) during the nonlinear analysis.

In Model 2, the shear stress behavior is represented by a tri-linear force-deformation (F-D) curve (Figure 2.11) that is adopted from ASCE/SEI 41-17 (2017). V_n represents the nominal ultimate shear strength, V_{cr} is the cracking strength and V_r denotes the residual strength.

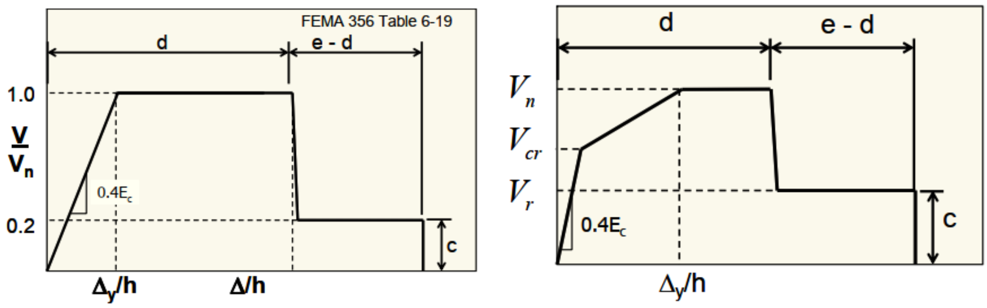

Figure 2.11. Shear force – deformation curves (ATC 72-1, 2010)

The mathematical expressions for V_n, V_{cr} and V_r are given in equations 2.1 and 2.2 based on the recommendations of codes, guidelines of nonlinear analysis, and research. (ATC 72-1,2010; ASCE/SEI 41-17 and Wallace, 2007). The following parameters are taken from the study by Wallace (2007) to determine the cracking and ultimate strength points.

$$V_{cr} = 4\sqrt{f_c'}\left[1 + \frac{P_u/A_g f_c'}{4\sqrt{f_c'}}\right]^{1/2} < 0.6V_n;\ \gamma_{cr} = \frac{V_{cr}}{0.4E_c} \qquad 2.1$$

$$V_y = V_n = A_{cv}\left(\alpha_c\sqrt{f_c'} + \rho_n f_y\right);\ \gamma_y = 0.004 \qquad 2.2$$

- P_u is the axial load on the wall.
- A_{cv} is the cross-sectional area of the wall
- f_c' is concrete compressive stress
- E_c is the elastic modulus of concrete
- α_c depicts types of a wall (e.g. squat or slender)
- ρ_n is the ratio of transverse reinforcement of the wall
- f_y is the yield stress of the reinforcement steel

The uncracked shear modulus is determined as $G_c = E_c 2(1+v) \cong 0.4E_c$ recommended by ASCE/SEI 41-17 (2017). Several studies (Orakcal et al, 2009, 2006; Wallace 2007) indicated that the increase in axial load on the wall makes the wall stronger and stiffer. In other words, the shear strength capacity of the wall is sensitive to the axial load level.

To summarize; the ultimate shear strength is set as ($V_{cu} = 1.5V_n\ at\ \gamma_y = 0.004$) based on the Orakcal et. al (2009) experimental results. The maximum shear strain is also set as $\gamma_y = 0.015$ based on the recommendation of ACI318-11 (2011). The detailed information about the shear F-D curve is provided in Appendix A.

2.2.1.2 Modeling of Frame (Beam) Element

Beam members with plastic hinges at the member ends are adopted based on the assumption of lumped plasticity model. (Figure 2.2.a). The inelastic beam behaviour is represented as a tri-linear backbone curve (Figure 2.12). The moment-curvature (M-K) analysis results and the backbone model for beam elements are provided in Appendix A.

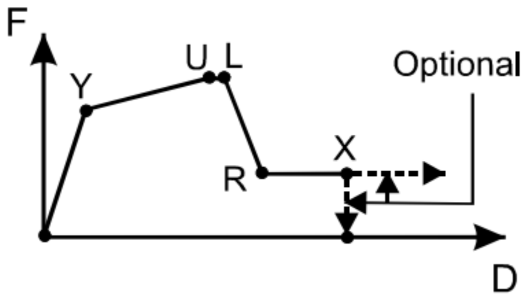

Figure 2.12: F-D Relationship in Perform 3D (Perfom3D User Guide, 2006)

The specific points (e.g. Y, U, L, and R) are derived from moment-curvature (M-K) analysis by using actual material properties and cross-section. Cyclic degradation and strength reduction are disregarded for beam members in this study.

The joint links between walls and beams are not defined. To prevent seismic instability, all beams and walls are connected with embedded beams stiffer than the beam elements in the model.

The coupling beams are modeled based on the recommendations of ATC-72 (2010). The guideline (ATC 72,2010) suggests that

a) Coupling beams are dominated by flexure if the condition is $l_n/h \geq 2.0$. So, $E_c I_{eff} \cong 0.15 E_c I_g \; and \; G_c = 0.4 E_c$ can be used for modeling.

b) Coupling beams are dominated by flexure and shear if the condition is $l_n/h \leq 1.4$. So, $E_c I_{eff} \cong 0.15 E_c I_g \; and \; G_c = 0.1 E_c$ can be used for modeling.

c) If clear span-to-depth ratio is between $1.4 \leq l_n/h \leq 2.0$, interpolation can be a reasonable approach for effective stiffness.

2.3 Important Modeling Assumptions

2.3.1 Gravity Loading Criteria

The tunnel form building model in this study is considered as a residential building. The building is initially subject to the gravity loads given in Table 2.1 before nonlinear analysis. The considered load combination is accepted as $G + 0.3Q$ where G represents all types of dead loads while Q represents the live loads. The total building mass given in Table 2.2 is derived from the above live and dead load combination. Structural mass at each floor level is assumed to act at the floor gravity center.

Table 2.1: Gravity Loads subjected to building

Load Name	Load Type	Value
Concrete Members	Dead Load	25 kN/m^3
Non-Structural Walls	Dead Load	3.54 kN/m^2
Overcoats	Dead Load	2.66 kN/m^2
Uniform Live Load	Live Load	2.0 kN/m^2

Table 2.2 Story masses at each floor

Building Type	Mass Horizontal Direction		Rotational Mass	
Tunnel Form with 6-story	840.6	kN.s^2/m	99688	kN.m.s^2

2.3.2 Effective Stiffness Definitions

The structural components are modeled as fiber elements (shear walls) and elastic beam-column elements (lumped plasticity, beams). The effective stiffness' of the structural elements consider the cracking of concrete under cyclic loading. The code provisions and design guidelines (e.g. ATC72-1, 2010 and LATBSCD, 2020) considered in this study suggest the effective stiffness values given in Table 2.3.

Table 2.3: Effective Stiffness Assumptions

Component	Axial	Flexural	Shear
Structural Walls	$1.0E_cA_g$	$0.35E_cI_g$	$1.0GA_g$
Beams	$1.0E_cA_g$	$0.3E_cI_g$	$1.0GA_g$
Coupling Beams	$1.0E_cA_g$	$0.2E_cI_g$	$1.0GA_g$

Note that effective stiffness value in fiber model is not conducted since fiber model directly consider cracking of concrete and steel yielding.

2.3.3 Other Modeling Assumptions

The Rayleigh damping procedure is implemented for defining the modal damping ratios. The critical damping is set as 2.5% at $0.2T_1$ and $1.5T_1$ points where T_1 is the fundamental mode period of the building per suggestions in ATC72-1 (2010).

As stated previously, the rigid diaphragm assumption is implemented at each node at the story level. The deck is used to transfer the gravity loads and lateral loads without significant loss of strength. This approach reduces the computational time in 3D analysis. Apart from rigid diaphragm assumption, the P-Delta effect is considered (which is also stated previously) in this study to account for negative post-yield stiffness.

2.4 Dynamic Analysis of Buildings

2.4.1 Modal Analysis

Dynamic modal properties of the building model are determined from eigenvalue analysis. The mode numbers for a variety of analyses are determined by considering the modal mass participation percentage. Vibration modes contributing to 90% of the total building mass in each principal direction are used in developing the equivalent single-degree-of-freedom system of the model building. Besides, the modal periods corresponding to these modes are used in developing the target spectra for different ground-motion intensity levels (simply hazard levels) that are used in ground-motion selection and selection for response history analyses. The equivalent SDOF systems representing the model building behaviour along each principal direction is utilized in Curic (2021) for running probabilistic risk assessment analyses of the same model building. The ground motions selected and scaled for target hazard levels are used in developing the fragilities of the model building in this study. This topic is discussed later in the thesis.

Appendix B presents the relevant modal properties (including the mode shapes) of the model building. Note that the 90% total mass contribution is reached in the 2nd mode along each principal direction in the 6-story building model. Torsional mode is disregarded.

2.4.2 Pushover Analysis

Nonlinear static procedure (NSP), known as a pushover, is performed in order to evaluate the nonlinear structural behavior and assess the damage limit states for the equivalent SDOF system according to the code provisions in ASCE/SEI 41-17 (2017), Eurocode8 (2005) and TBSDC-18 (2018). The monotonically increasing distributed load implemented along the building height is compatible with the dominant mode shape in each principal direction. The load is increased incrementally until the global dynamic instability occurs. The inelastic behavior is evaluated at each level to investigate the damage limit state points. The pushover curves are provided in Appendix B.

2.4.3 Push-Pull Analysis

A push-pull analysis is implemented to deriving the hysteretic models of the equivalent SDOF systems in principal each direction. Curic (2021) generates a hysteric model using Ibarra et al. (2005) for nonlinear SDOF response history analysis consistent with the results of push-pull curves to capture the cyclic degradation. The distributed load along the building height that is compatible with dominant modal shapes along each principal direction is used in the push (along positive direction) and pull (along negative direction) analysis. Each push follows the conditions of the previous one in terms of the building’s dynamic properties. The push-pull aims to capture the cyclic degradation resulting from component damage and the analysis results from push-pull are given in Appendix B.

3 THE DAMAGE STATE ASSESSMENT OF THE MODEL BUILDING UNDER DIFFERENT CODE PROVISIONS

3.1 Introduction

The tunnel form performances at different damage states are investigated for different code provisions. Several codes provide different performance levels in terms of structural damage. For instance, Eurocode8 (hereafter abbreviated as EC8-3) categorizes structural damage in terms of chord rotation whereas, TBSDC-18 (2018) considers strain limits. In this section, the acceptance criteria and performance levels of different code provisions are briefed. Then, the damage state limits are determined based on the code definitions of structural damage states. Three codes are used for this purpose: TBSDC-18, EC8-3, and ASCE/SEI 41-17.

3.1.1 Damage State Definitions of TBSDC-18 (2018)

TBSDC-18 defines three damage limit states under three performance points. (LD: Limited Damage; CD: Controlled Damage CP: Collapse Prevention, Figure 3.1). The structural performance is assessed by utilizing strain limits of concrete and reinforcement steel. The given limit states assume ductile members whereas, brittle failure is not permitted.

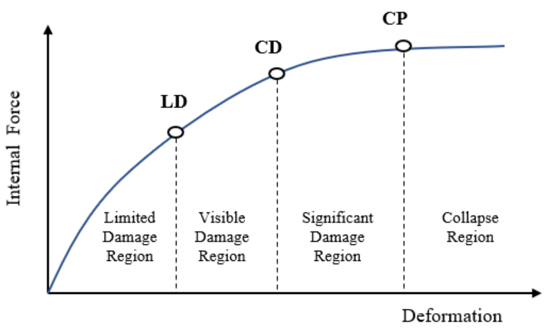

Figure 3.1: TBSDC (2018) Performance Points

3.1.2 Damage State Definitions of EC8-3 (2005)

EC8-3 defines structural performance at three performance points. They are described as Near Collapse (NC), Significant Damage (SD), and Limited Damage (LD). The structure is subject to permanent drift and the vertical elements carry the vertical loads as well –creating more possibilities for collapse—. The structure must be retrofitted at Near Collapse (NC) and the structural stiffness decreases after an earthquake. There are some residual drifts at the Significant Damage (SD). According to Limited Damage (LD), no structural element is damaged. The structure is supposed to survive after such an earthquake. The component performance is assessed by means of chord rotation.

3.1.3 Damage State Definitions of ASCE/SEI 41-17 (2017)

ASCE/SEI 41-17 identifies three structural performance levels: Immediate Occupancy (IO), Life Safety (LS), and Collapse Prevention (CP). The code categorizes the structural performance levels by considering the types of structural analysis: that is, linear or nonlinear. Nonlinear assessment procedures are considered in this study. In ASCE/SEI 41-17, the component acceptance criteria are based on failure types of components. In shear walls, if walls are controlled by flexure; the acceptance criterion is based on plastic rotation. Moreover, if walls are controlled by shear; the acceptance criterion is based on lateral story drift ratio. On the other hand, beams are controlled by plastic rotation while coupling beam controlled by shear is checked by means of chord rotations. The determination of plastic hinges, lateral story drift, and chord rotations are shown in Figure 3.2.

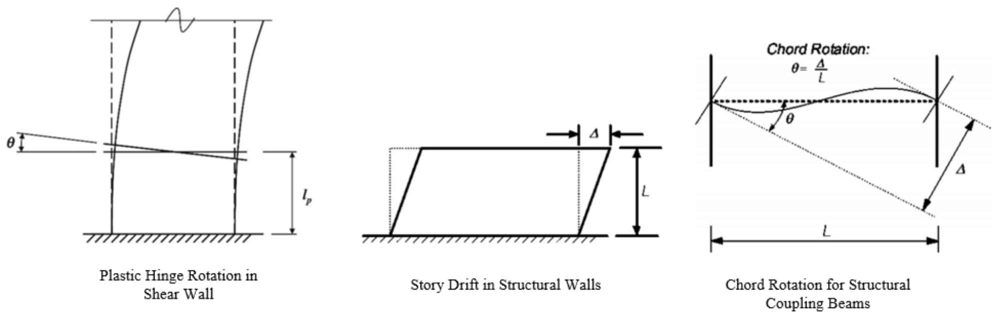

Figure 3.2. The determination of component damage (ASCE/SEI 41-17)

3.2 Performance Criteria for Nonlinear Performance Assessment

3.2.1 Damage State Limits of TBSDC-18

The damage states of structural elements are evaluated in terms of strain limits. Strain limits for structural walls and plastic rotation limits for beams are calculated according to the provisions in TBSDC-18 that are given below for convenience.

Concrete strain limits for different damage states (CP: Collapse Prevention, CD: Controlled Damage and LD: Limited Damage) are given in Eqns. 3.1, 3.2, and 3.3.

$$\varepsilon_C^{CP} = 0.0035 + 0.04\sqrt{\omega_{we}} \leq 0.018 \tag{3.1}$$

$$\varepsilon_C^{CD} = 0.75\ \varepsilon_C^{CP} \tag{3.2}$$

$$\varepsilon_C^{LD} = 0.0025 \tag{3.3}$$

$$\omega_{we} = \alpha\rho_{sh,min}\frac{f_{ywe}}{f_c} = \left(1 - \left(\frac{\sum a_i^2}{6b_0h_0}\right)\right)\left(1 - \frac{s}{2b_0}\right)\left(1 - \frac{s}{6h_0}\right)\rho_{sh,min}\frac{f_{yw}}{f_c} \tag{3.4}$$

The state of collapse prevention is limited by Eqn (3.1). It is composed of two parts: the contribution of unconfined concrete and confinement mechanism where ω_{we} (Eqn (3.4)) is the mechanical reinforcement ratio depending on the stirrup spacing (s), ratio of transverse steel (ρ_{sh}), cross-section (b_0, h_0), longitudinal reinforcement spacing (a_i), and concrete and reinforcement material properties (f_{ywe}, f_c). While control damage limit (Eqn 3.2) depends on collapse prevention limit. Limited damage state is limited by Eqn (3.3).

Reinforcement strain limits for different damage states are described in Eq. 3.5, 3.6, and 3.7 where ε_{su} is the ultimate strength of reinforcement.

$$\varepsilon_S^{CP} = 0.4\varepsilon_{su} \tag{3.5}$$

$$\varepsilon_S^{CD} = 0.75\ \varepsilon_S^{CP} \tag{3.6}$$

$$\varepsilon_S^{LD} = 0.0075 \tag{3.7}$$

Once the damage states of all structural members are identified, the overall performance (damage state) of the building is determined by considering the following definitions.

Limited Damage Performance Level:

For each principal direction of earthquake loading, at least 20% (or more) of the beams at any story level shall not be exposed to a damage. All other structural members can be in the limited damage state. No plastic hinging shall be formed on the member ends.

Controlled Damage Performance Level:

For each principal direction of earthquake loading, at least 35% (or more) of the beams at any story level shall not be in the significant damage region. The vertical structural members reaching to the significant damage region shall not be subjected to more than 20% of the total lateral force resisted by the other vertical members at the same story level. All other structural members shall be in the limited damage state.

Collapse Prevention Performance Level:

For each principal direction of earthquake loading, at least 20% (or more) of the beams at any story shall not be in the collapse prevention region. All other structural members shall be either in the significant damage or limited damage regions. The building should provide a safety margin against collapse.

3.2.2 Damage State Limits of EC8-3

EC8-3 does not propose any global damage state (or equivalently performance) limits. The performance assessment, hence the damage state limits, is evaluated by means of chord rotation. The following expressions (Eq. 3.8 and 3.9) define the ultimate chord rotation capacity and significant damage limits for both structural walls and beams.

$$\theta_{um} = \frac{1}{\gamma_{el}} 0.0172\ (0.3^{v}) \left[\frac{max(0.01,\omega')}{max(0.01,\omega)} f_c\right]^{0.175} \left(\frac{L_v}{h}\right)^{0.4} 25^{\left(\alpha\rho_{sx}\frac{f_{ywe}}{f_c}\right)} (1.3^{100\rho_d}) \tag{3.8}$$

The ultimate chord rotation capacity is based on the transverse reinforcement ratio, mechanical and material properties of the section, and longitudinal reinforcement ratio. The damage limits are calculated for beams and structural walls separately.

The chord rotation capacity is composed of parameters as follows:

- γ_{el} : 1.5 for primary seismic elements
- v : ratio of axial force and the area of the compression zone
- ω and ω' : the mechanical reinforcement ratio for tension and compression longitudinal reinforcement.
- L_v : the ratio moment/shear at the end section
- h : the depth of the cross-section
- α : the confinement effectiveness factor
- ρ_s : the ratio of transverse reinforcement
- f_{ywe}, f_c : transverse reinforcement yields strength and concrete compressive strength
- ρ_d : the steel ratio of diagonal reinforcement in each principal direction

$$\theta_{SD} = \frac{3}{4}\theta_{um} \tag{3.9}$$

The expression to compute the limit state of damage limitation (DL) is given in Eqn. 3.10 and Eqn. 3.11 for beams and structural walls, respectively at the yield point. These expressions include flexural and shear contributions.

$$\theta_y = \emptyset_y \frac{L_v + a_v z}{3} + 0.0014\left(1 + 1.5\frac{h}{L_v}\right) + \frac{\varepsilon_y}{d - d'} \frac{d_{bL} f_y}{6\sqrt{f_c}} \text{ for beams and columns} \quad 3.10$$

$$\theta_y = \emptyset_y \frac{L_v + a_v z}{3} + 0.0013 + \frac{\varepsilon_y}{d - d'} \frac{d_{bL} f_y}{6\sqrt{f_c}} \text{ for walls of rectangular, T- or barbelled section} \quad 3.11$$

where:

- $\emptyset_y$: yield curvature of the end section
- z : the length of the lever arm
- f_c and f_y : concrete strength and steel yield strength
- d and d' : the depths to tension and compression reinforcement
- d_{bL} : the mean diameter of tension reinforcement
- ε_y : the strain of reinforcement

3.2.3 Damage State Limits of ASCE/SEI-41

As in the case of EC8-3, ASCE/SEI 41-17 does not provide any global damage state limits. They are at the member level. Although the code also provides performance (damage state) limits for non-structural elements, they are not taken into consideration in this study.

As described in section 2.2.1, the shear stress-strain relationship in the second model is adopted as a tri-linear force deformation curve to represent inelastic shear behavior because the damage state limits provided by this standard categorize the structural failures as flexure and shear.

3.2.4 Summary

To summarize; the performance points corresponding to different damage states according to each standard (i.e., TBSDC-18, EC8-3, and ASCE/SEI 41-17) are taken into consideration in this study. TBSDC-18 evaluates performance levels in terms of strain limits. The expressions and formulations are given for concrete and reinforcement steel in Section 3.2.1. EC8-3 considers chord rotation capacity to assess performance points. All formulations and descriptions corresponding to three different damage state limits are given in Section 3.2.2. ASCE/SEI 41 provides damage limit states at member levels like TBSDC-18 and EC8-3. The performance evaluation is assessed with respect to structural failure: shear or flexure. The second model considering shear behavior as inelastic is built to assess structural failure: shear and flexure separately. All damage limit states points computed from formulations described in previous sections are given in Attachment C.

3.3 Damage States (Performance Points) Limits of Equivalent SDOF System

This section presents the computed performance points (damage state limits) of the equivalent SDOF systems representatives of the 6-story model building, based on the three earthquake standards discussed in the previous sections. After performing the pushover analysis along with the principal directions, the damage state limits per the provisions of each standard are implemented to determine the damage states and corresponding performance points on the pushover curve. Figure 3.3, Figure 3.4, and Figure 3.5 show the resulting pushover curves along with principal directions as well as the performance points corresponding to different damage states according to each standard (i.e., TBSDC-18, EC8-3, and ASCE/SEI 41-17).

The overall performance level is obtained according to the damage levels of vertical structural members and their distribution over the building height. The performance points shown in Figure 3.3, Figure 3.4, and Figure 3.5 are the points where the first cracking in the vertical element occurs. The threshold values in terms of engineering demand parametes are listed in Table 3.1. Finally, Figure 3.6 shows that different engineering demand parameters lead to different results under the same earthquake load.

Table 3.1 The threshold values of mid-rise tunnel form buildings at damage limit states

	X Dir (Roof Disp.(m)			**Y Dir (Roof Disp.(m)**		
EDP	**IO**	**LS**	**CP**	**IO**	**LS**	**CP**
Strain	0.115	0.251	0.310	0.071	0.155	0.192
Chord Rotation	0.033	0.226	0.277	0.032	0.142	0.183
Plastic Rotation	0.128	0.309	0.393	0.084	0.197	0.280

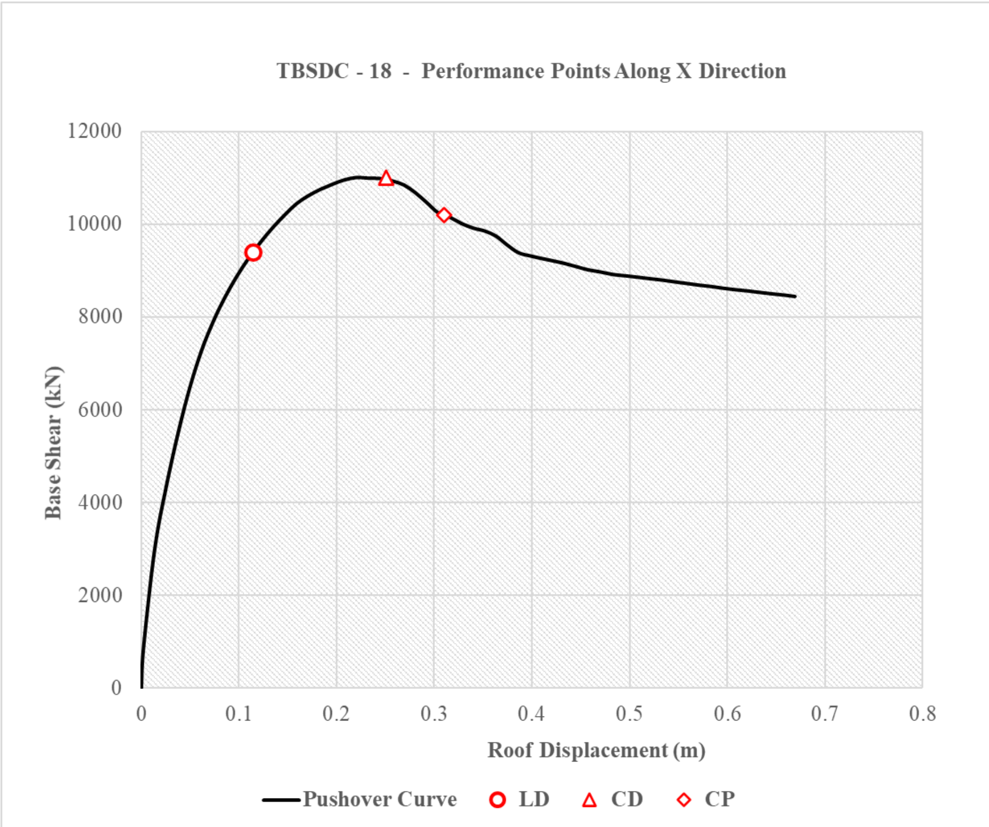

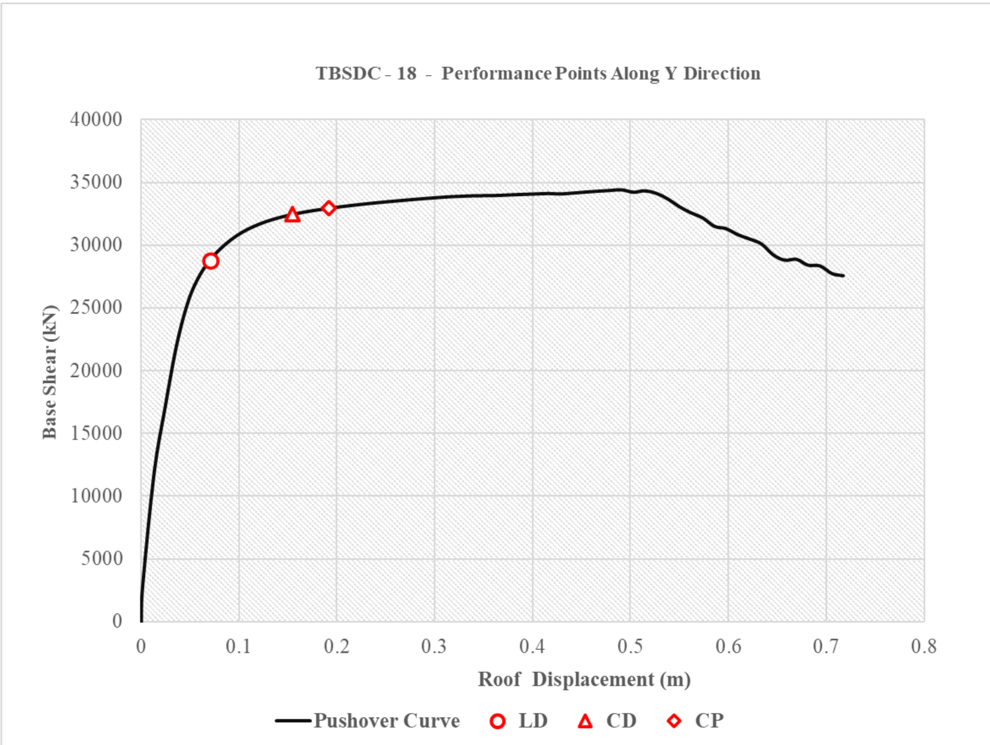

Figure 3.3. Performance Points (Damage States) according to TBSDC-18

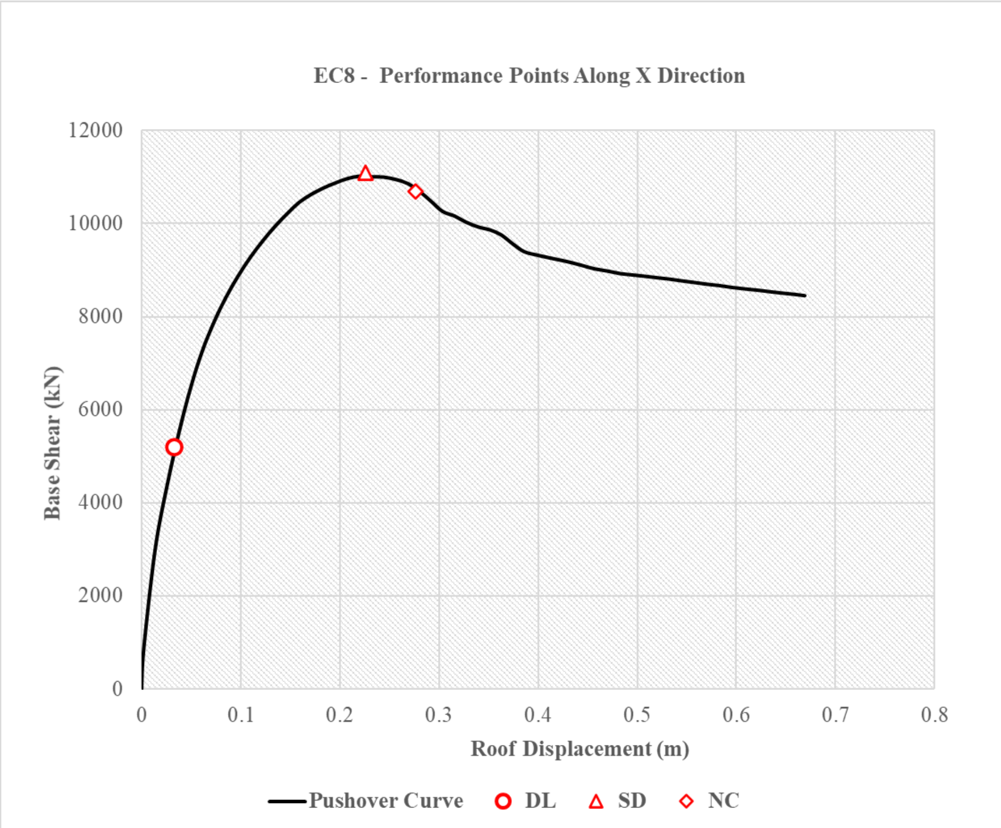

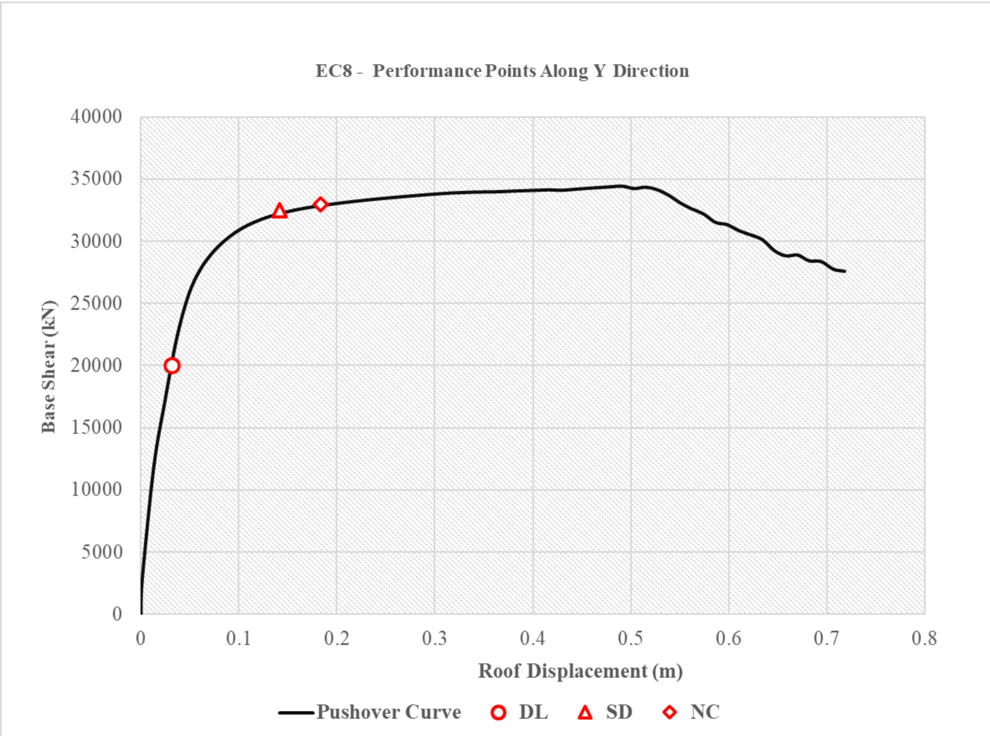

Figure 3.4 Performance Points (Damage States) according to EC8-3

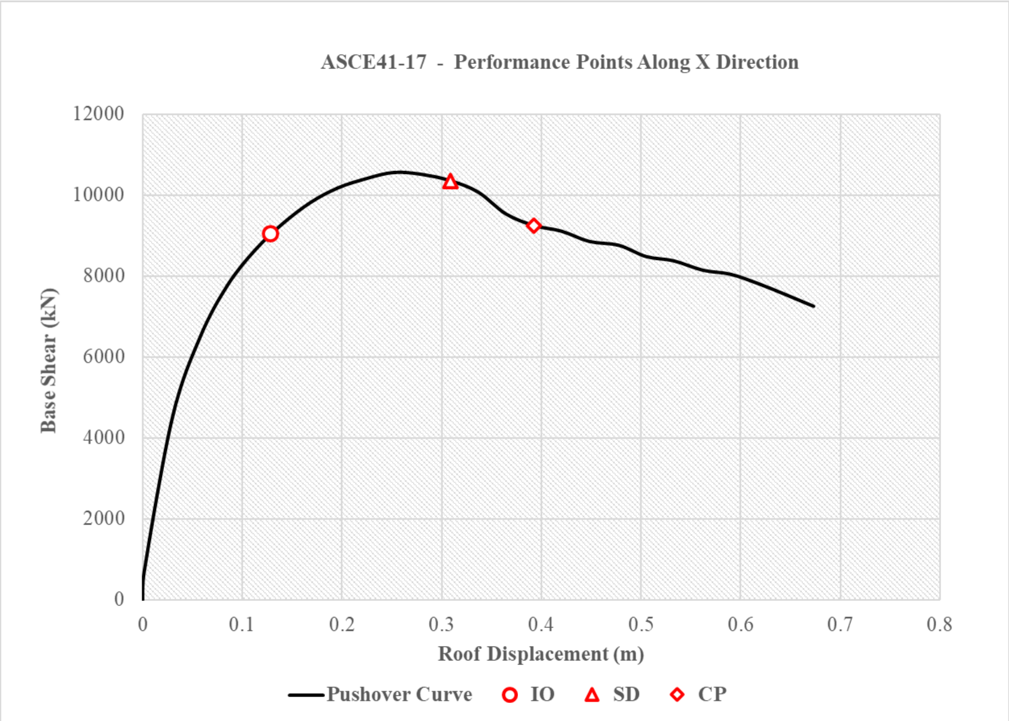

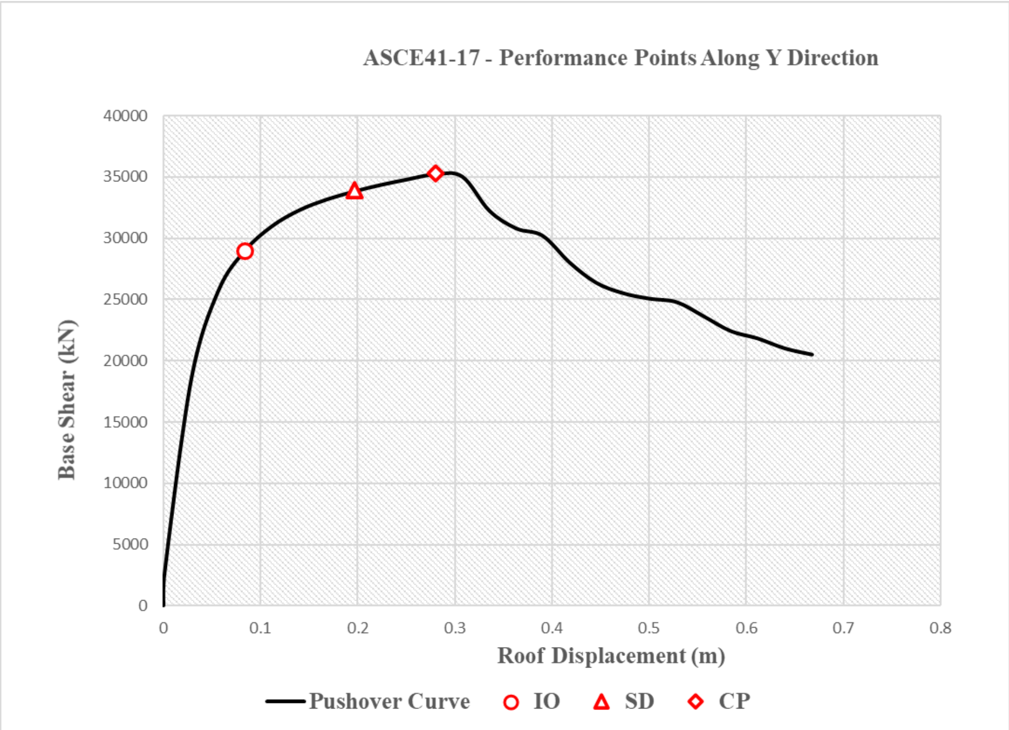

Figure 3.5 Performance Points (Damage States) according to ASCE/SEI 41-17

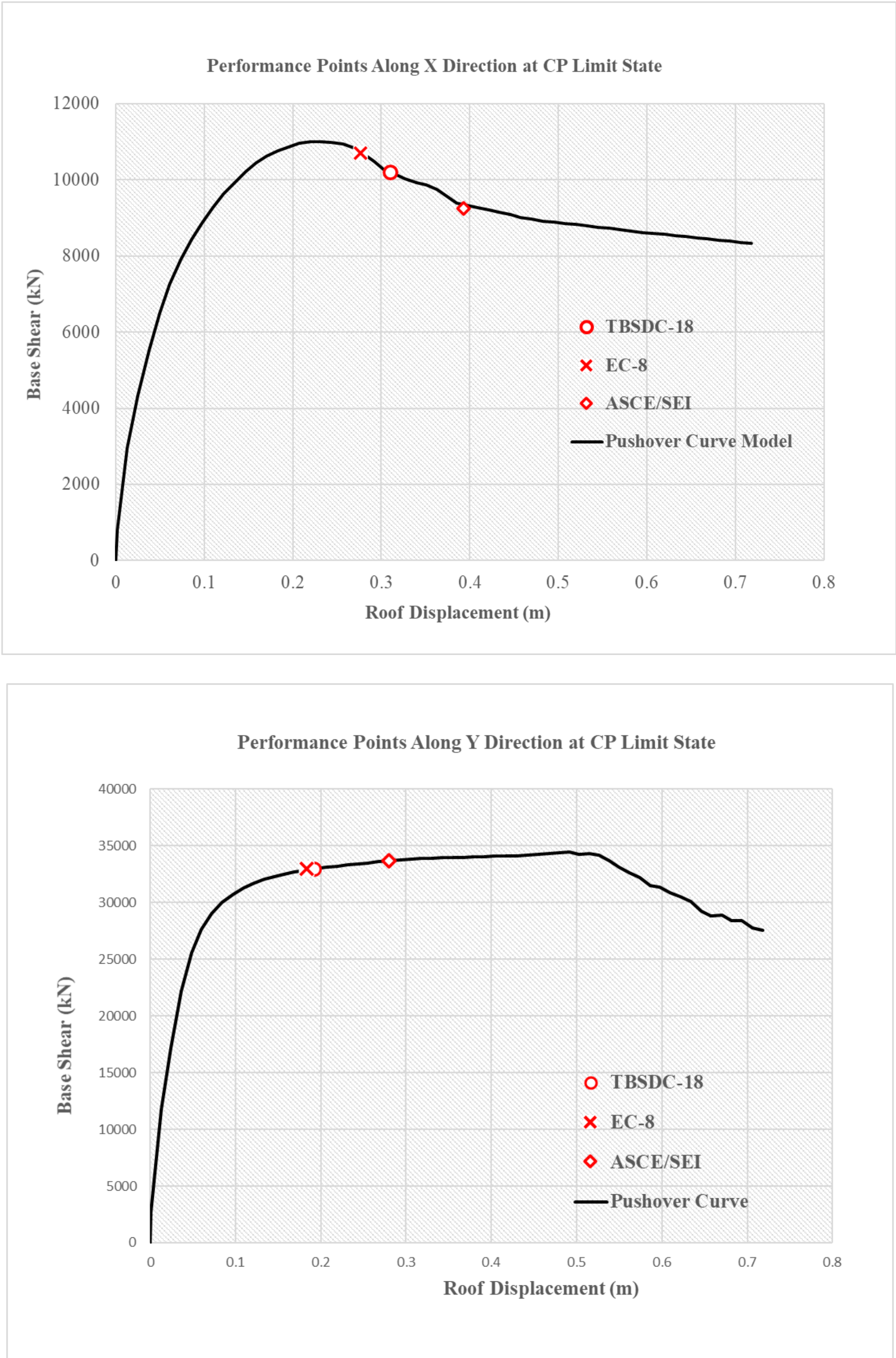

Figure 3.6 Performance Points (Damage States) at CP Limit State according to three codes

4 GROUND MOTION CHARACTERIZATION

4.1 Introduction

Some important points in probabilistic seismic hazard assessment (PSHA), and the record selection and scaling are briefed in this chapter. The details of these studies can be found in Curic (2021). The PSHA is performed for a site in the Atasehir district in Istanbul and its results are used to develop the target response spectra at different hazard levels. The target response spectra are based on Conditional Spectrum (CS) (Lin et al, 2013) conditioned on average spectral acceleration (AvgSA) (Kohrangi et al, 2017). The ground-motion records are selected and scaled by considering the target response spectra for performing NRHA.

As indicated, the selected site (Figure 4.1) is located in the Ataşehir district, which is one of the densely populated and seismic prone districts in Istanbul. There are also densely populated tunnel form buildings in this district. The shear wave velocity (V_{s30}) is selected as $V_{s30} = 375\ m/s$ according to the V_{S30} map (Figure 4.2) provided by IBB-KRADE (2020).

Figure 4.1 Location of Site. [Google Earth v7.3.3.7786 (April 30, 2021). Atasehir, Istanbul. (40.982959N, 29.128342E), Eye alt 633m. Maxar Technologies 2021, Basarsoft 2021, Google 2021. (June 01, 2021)]

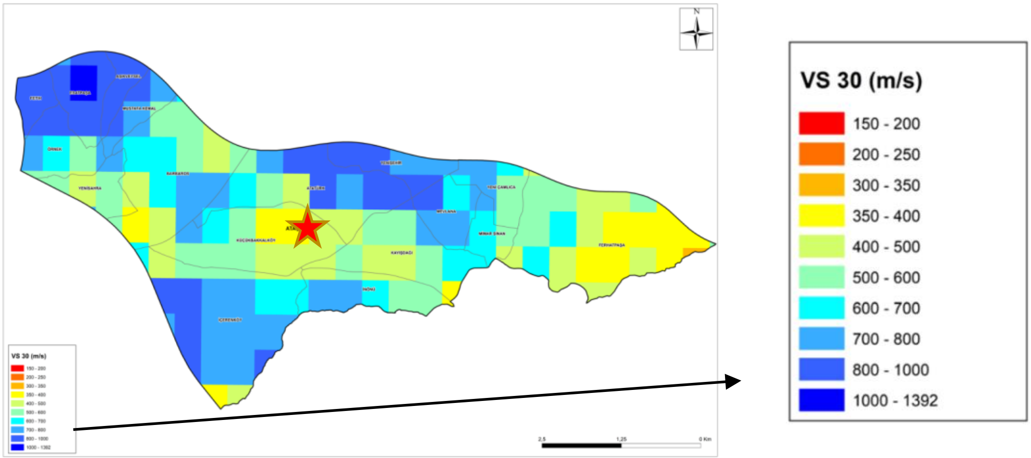

Figure 4.2 The shear wave velocity map of Ataşehir (IBB-KRADE, 2020). The red star refers to the location of the site.

4.2 Uniform Hazard Spectra and Conditional Spectra for Ground Motion Selection and Scaling

The site-specific PSHA is performed at fourteen different hazard levels. (Curic, 2011). Of these hazard levels, eight of them are taken into account for developing the fragility functions in this study. The return periods as well as the corresponding uniform hazard spectra (UHS) are shown in Figure 4.3.

After performing PSHA, the conditional spectra conditioned on average spectral acceleration $CS(AvgSA)$ are computed using the modal periods of the first four modes (except for the torsional mode) of the model building as well as two additional periods to capture period elongation due to building's post elastic response and possible higher mode effects. The sum of modal mass contributions of the four modes exceeds 90% of the total effective modal mass. The two additional periods used to capture the nonlinear period elongation as well as the higher mode effects correspond to 1.5 and 0.2 times, respectively, the fundamental mode periods in two orthogonal building directions (principal axes of the model building).

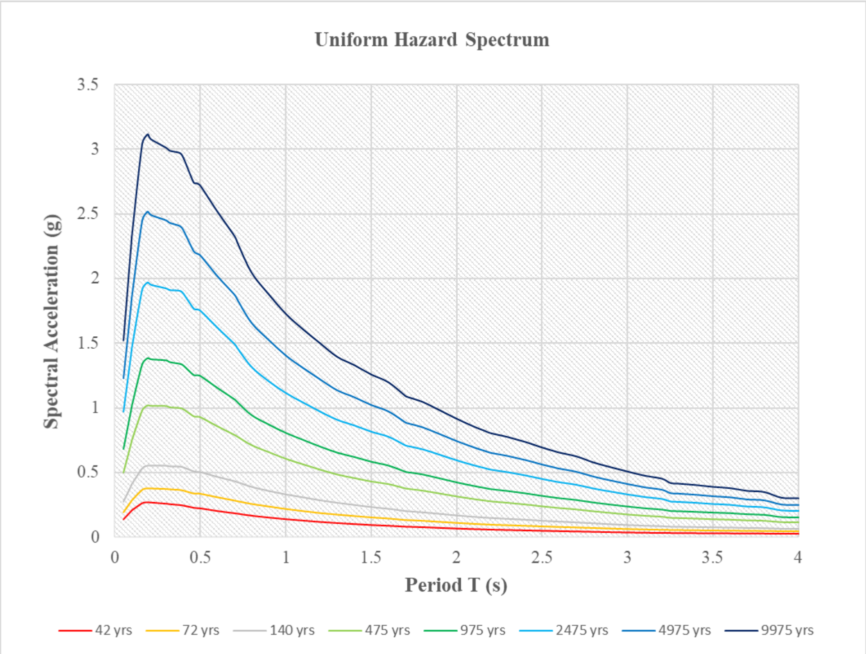

Figure 4.3 Uniform hazard spectra at different return periods that are based on the PSHA study by Curic (2021). The ground-motion predictive model used in the PSHA is Akkar et al (2014). The reader is referred to Curic (2021) study for details.

The average spectral acceleration (AvgSA) is selected as the intensity measure (IM) as it is described as efficient, self-sufficient, and practical (Bianchi et al, 2009 and Kohrangi et al, 2017). The AvgSA can be defined in several ways. Bianchi et al. (2009) and Kohrangi et al. (2017) are defined this IM as the geometric mean of the spectral accelerations of a set of periods (Eq. 4.1). It is constrained between $0.2T_1 \leq T_i \leq 1.5T_1$ where T_1 is the dominant period of the structure. The period range as defined above accounts for the higher mode effects and the period elongation due to post-elastic building response. (Kohrangi et al, 2017).

$$AvgSA = \left[\prod_{i=1}^{n} SAT_i\right]^{1/n} \qquad 4.1$$

In his thesis, Curic (2021) makes a modification to Eq 4.1 by redefining AvgSA as presented in Eq 4.2. He considers a weighted average spectral acceleration (AvgSA1) and the weights are chosen as the modal effective mass ratios of the considered modal periods. The weights corresponding to the periods representing period elongation and higher mode effects are set equal to that of the fundamental mode period weights. The weights add up to unity (1).

$$AvgSA1 = AvgSA(\vec{T}_1, \vec{W}_1) \quad 4.2$$

The conditional spectrum conditioned on AvgSA1 is performed by considering six different periods. These are: T_{1x}, $T_{1y}, T_{2x}, T_{2y}, 1.5T_{1x}, 1.5T_{1y}$ where x and y denote the principal axis of the 3D model building. Figure 4.4 is an example of conditional spectrum conditioned on AvgSA for 2475 return periods (MCE). The CS (AvgSA) for all return periods is shown in Appendix D (provided by Curic, 2021). All scaling factors and ground motions are also listed in Appendix D.

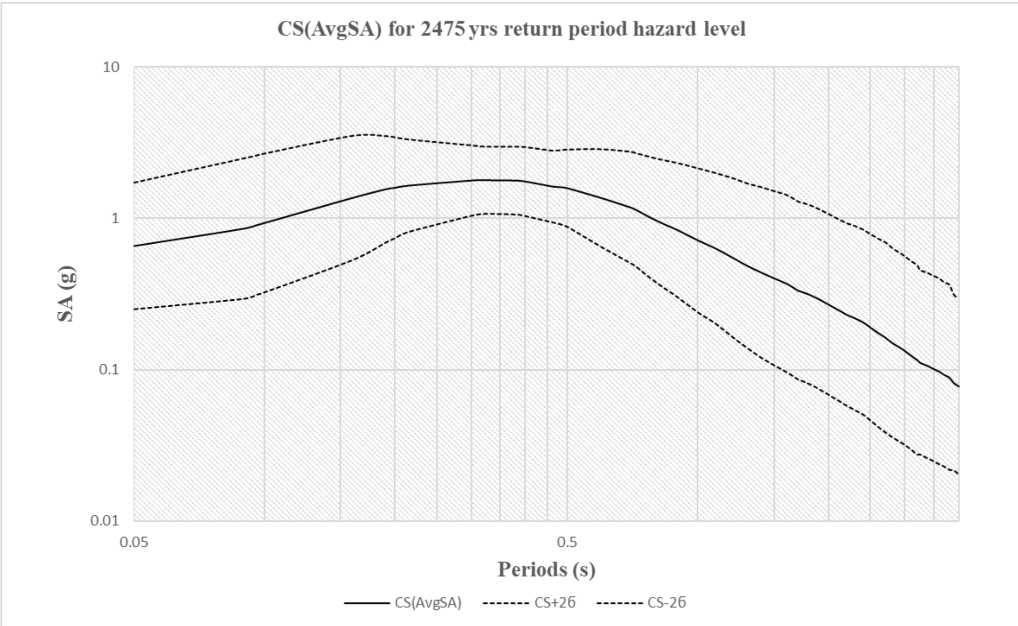

Figure 4.4 Conditional spectrum conditioned on AvgSA for 2475 return periods

4.3 The Input Ground Motions Dataset for NRHA

The input ground motions are selected and scaled at eight different hazard levels represented by different return periods. The legends of Figure 4.3 designate the considered return periods in this study. The ground-motion records compiled from the PEER website (https://ngawest2.berkeley.edu) are scaled to the target conditional spectra conditioned on AvgSA as explained in the previous sections. A total of 20 horizontal ground-motion pairs at each hazard level are scaled by considering cloud scaling. Shome and Cornell (1999) indicate that the use of minimum of 20 records is sufficient to define the mean and standard deviation of the target EDP. The scaling is performed such that the average of the scaled horizontal ground-motion pairs follows the mean conditional spectrum given a target hazard level. The selection of the ground motions relies on the most contributing earthquake scenarios at the target hazard level that are determined from disaggregation analysis. The details of cloud scaling as well as the record selection can be found in Curic (2021). The selected ground-motion sets are given in Appendix D.

5 NONLINEAR RESPONSE HISTORY ANALYSIS AND STRUCTURAL RESPONSE

5.1 Introduction

The 6-story tunnel form model building is subjected to scaled ground motions that are representatives of different hazard levels as summarized in the previous chapter. The engineering demand parameters (EDPs) determined from the NRHA are, for example, shear forces at each floor, interstory drift ratios (IDRs), and plastic deformations in SWs, and they are evaluated in this chapter. The structural performance of the model building is evaluated in terms of strain limits, chord rotations, and plastic rotations based on the damage limit states defined by the design codes of interest in this study. The NRHA is based on multiple stripe analysis (MSA; Reference) and a total of 640 response history analyses are executed for determining the EDP distributions for performance evaluation of the model building.

5.2 Structural Response Evaluation

Engineers consider several EDPs for assessing the structural performance such as shear forces at each level, plastic rotations, or IDRs. The identification of "sufficient" and "efficient" IMs that are consistent and compatible with EDPs is one of the most critical points in building performance assessment. Several studies (Bianchini et all, 2009, Kohrangi et all, 2016) stated that an "efficient" and "sufficient" IM correlates well with EDPs of interest since a good correlation between these two variables lead to low dispersion in EDPs that means lesser number of ground motion records for NRHA. The evaluation of IDR, shear forces and plastic rotations, and strain limits in terms of efficiency and sufficiency is the focus of this section.

The IDR results based on MSA (to account for different hazard levels) are calculated in both principal directions for Model 1 and Model 2. (Note as a reminder that the shear behavior in model 2 is considered as nonlinear whereas the first model is assumed that the shear is linearly elastic). The IDR results presented in Figure 5.1 to Figure 5.4 indicate that the damage is generally concentrated at the ground story in each horizontal direction and the damage modality is dominated by the first mode. However, in the second model, the damage shifts to upper stories in the y-direction (short direction in plan view) as given in Figure 5.4 due to the nonlinear shear behavior Note that the plastic deformations can be defined better by considering the inelastic shear behaviour defined in model 2. The maximum IDR occurs at the ground story except for the short direction in Model 2 due to out-trigger effects and nonlinear shear behaviour. Needless to say, the damage increases as the hazard levels increase.

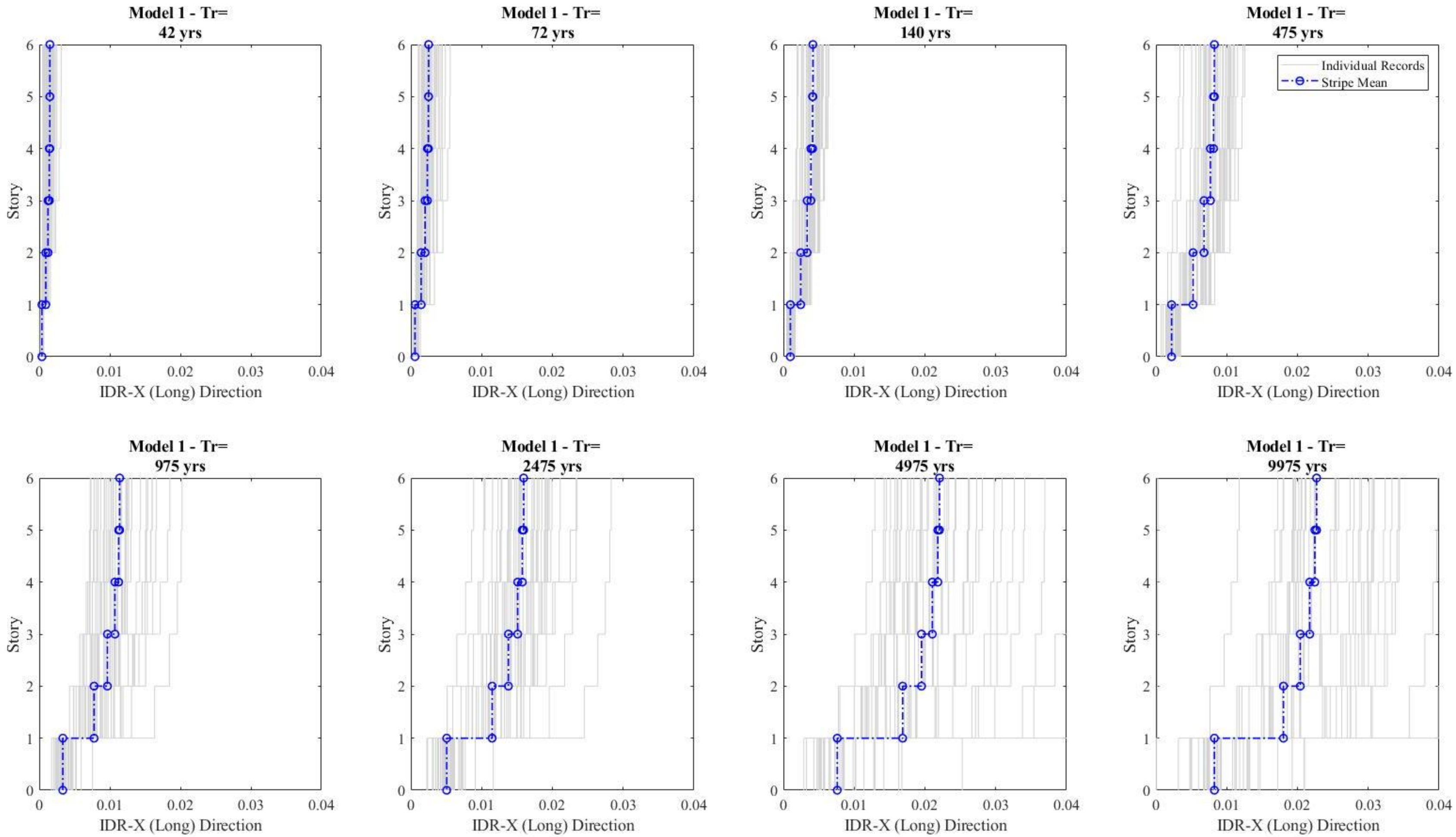

Figure 5.1 The IDR distribution along with the model building height in the x-direction for Model 1

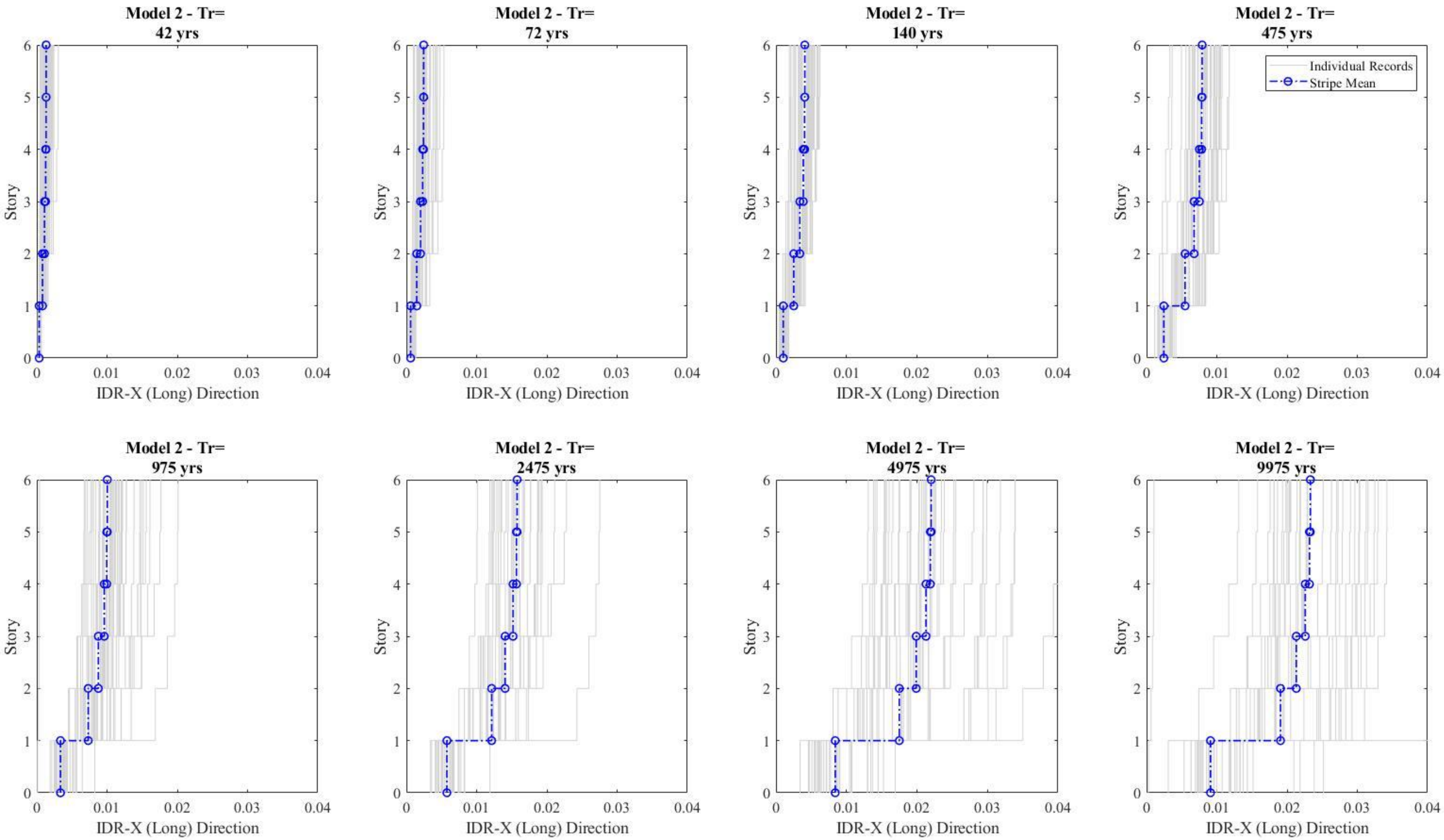

Figure 5.2 The IDR distribution along with the model building height in the x-direction for Model 2

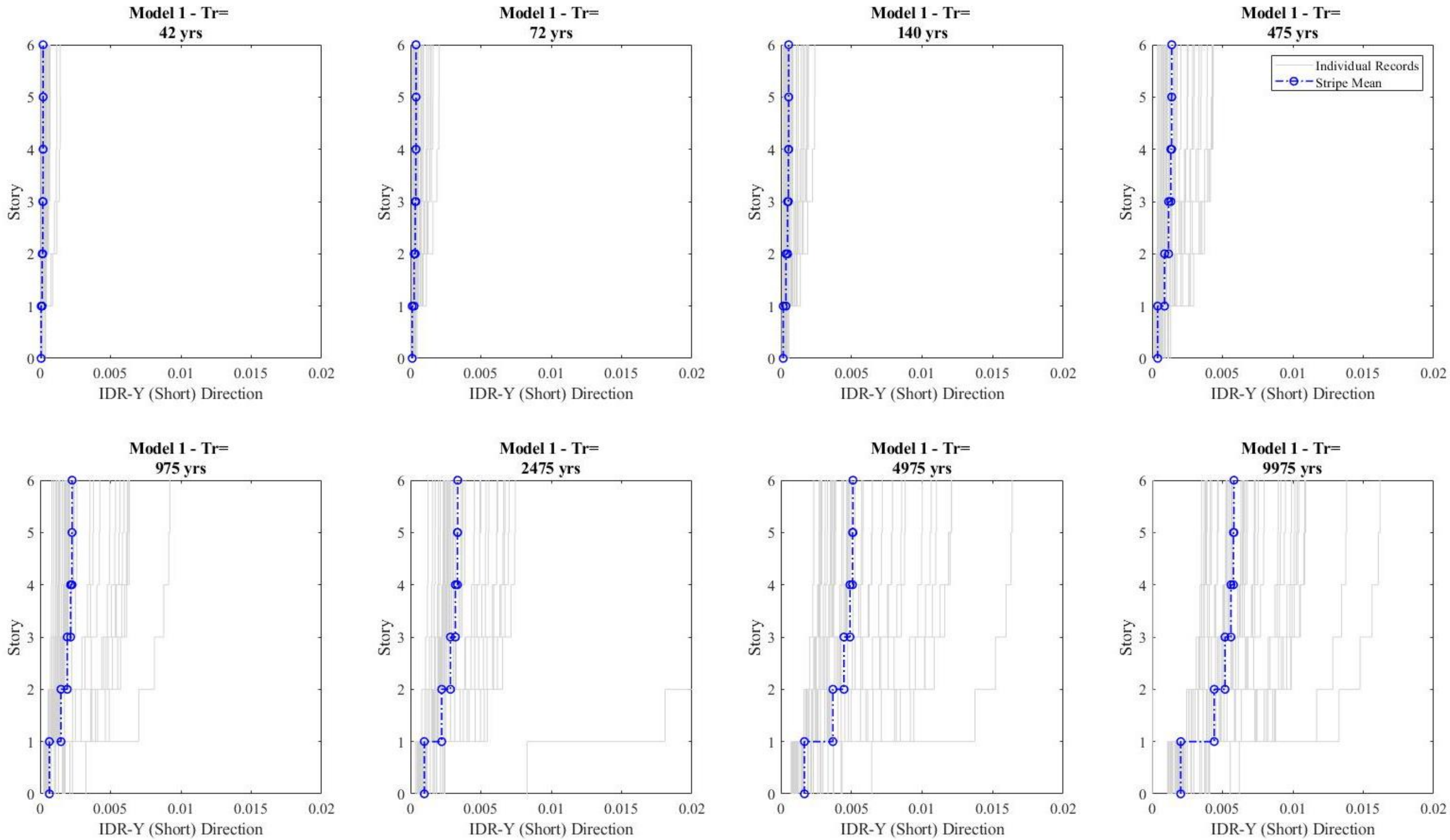

Figure 5.3 The IDR distribution along the model building height in y direction for Model 1

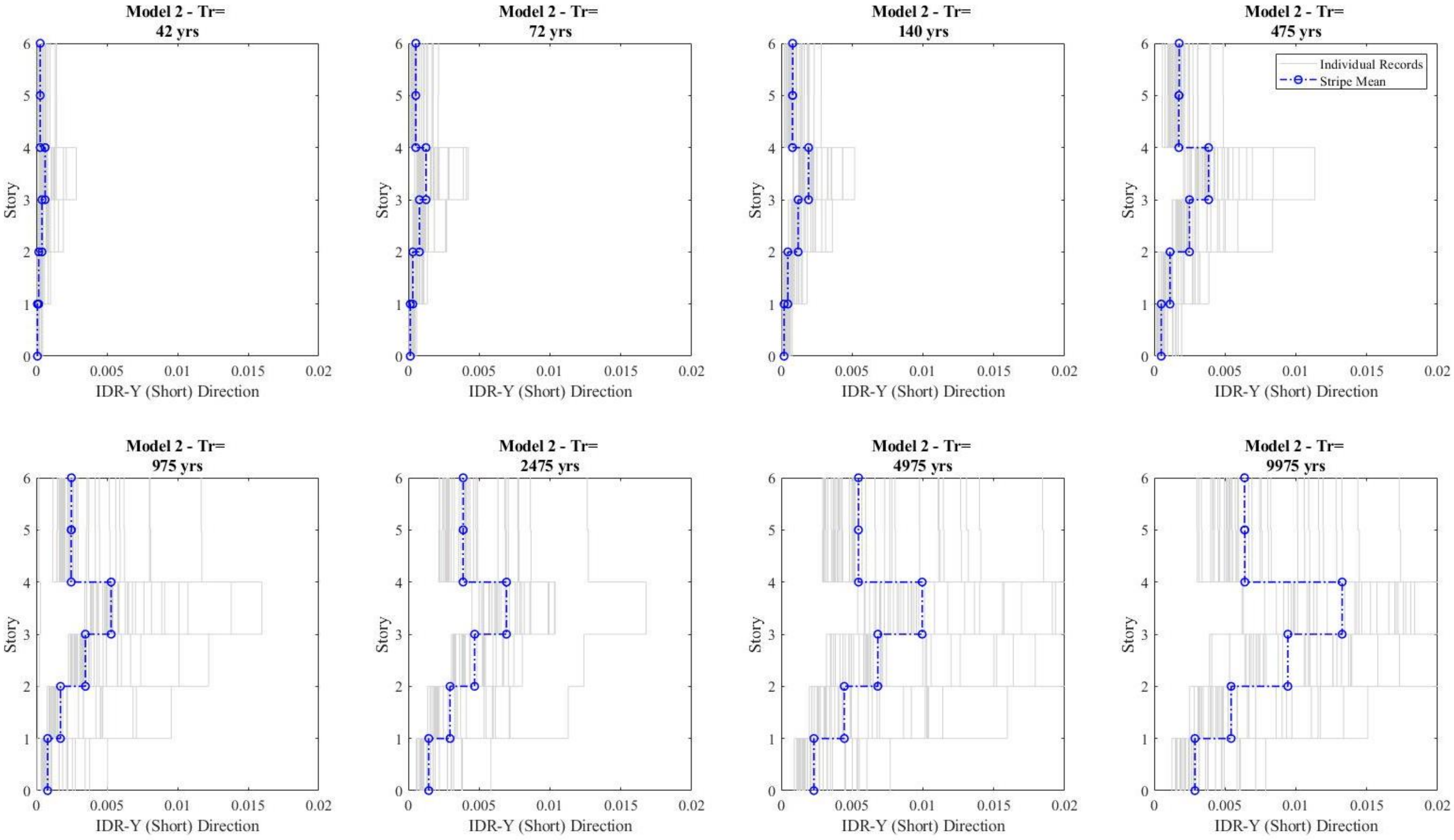

Figure 5.4 The IDR distribution along with the model building height in y-direction for Model 2

Figure 5.5 displays the NRHA results for maximum interstory drift ratios (MIDRs) at the predefined target hazard levels. Table 5.1 lists the mean (average) MIDR at each hazard level for Model 1 and 2. The maximum MIDR tends to occur in x-direction due to smaller shear areas (total area of SWs in each principal direction) in this direction.

Table 5.1 Maximum average inter-story drift ratio

Hazard Level (yrs)	**Average MIDR**			
	Model 1		Model 2	
	X Dir	Y Dir	X Dir	Y Dir
42	0.15%	0.02%	0.13%	0.06%
72	0.25%	0.04%	0.25%	0.13%
140	0.42%	0.06%	0.41%	0.19%
475	0.83%	0.14%	0.79%	0.38%
975	1.14%	0.23%	1.00%	0.53%
2475	1.59%	0.34%	1.58%	0.69%
4975	2.21%	0.51%	2.00%	0.99%
9975	2.27%	0.58%	2.33%	1.33%

The following observations are made for MIDR from the results of NRHA:

- The long direction tends to have larger MIDRs and MIDR keeps increasing with the increase in hazard level. This may suggest that the model building can resist larger hazard levels due to a positive correlation between hazard level and MIDR.
- The IDR results (see Figure 5.4) have proven that the damage can be observed at higher stories if the shear behavior is modeled as inelastic. (Note as a reminder that the shear behavior in model 2 is considered as nonlinear whereas the first model is assumed that the shear is linearly elastic).
- The MIDR does not exceed 2% and 1%, respectively, for maximum considerable earthquake (MCE; represented by 2475-year return period hazard level) and design basis earthquake (DBE; represented by 475-year return period hazard level), respectively.
- The larger shear areas (y-direction in the model building) inherently result in smaller MIDR, reducing the probability of heavy damage.

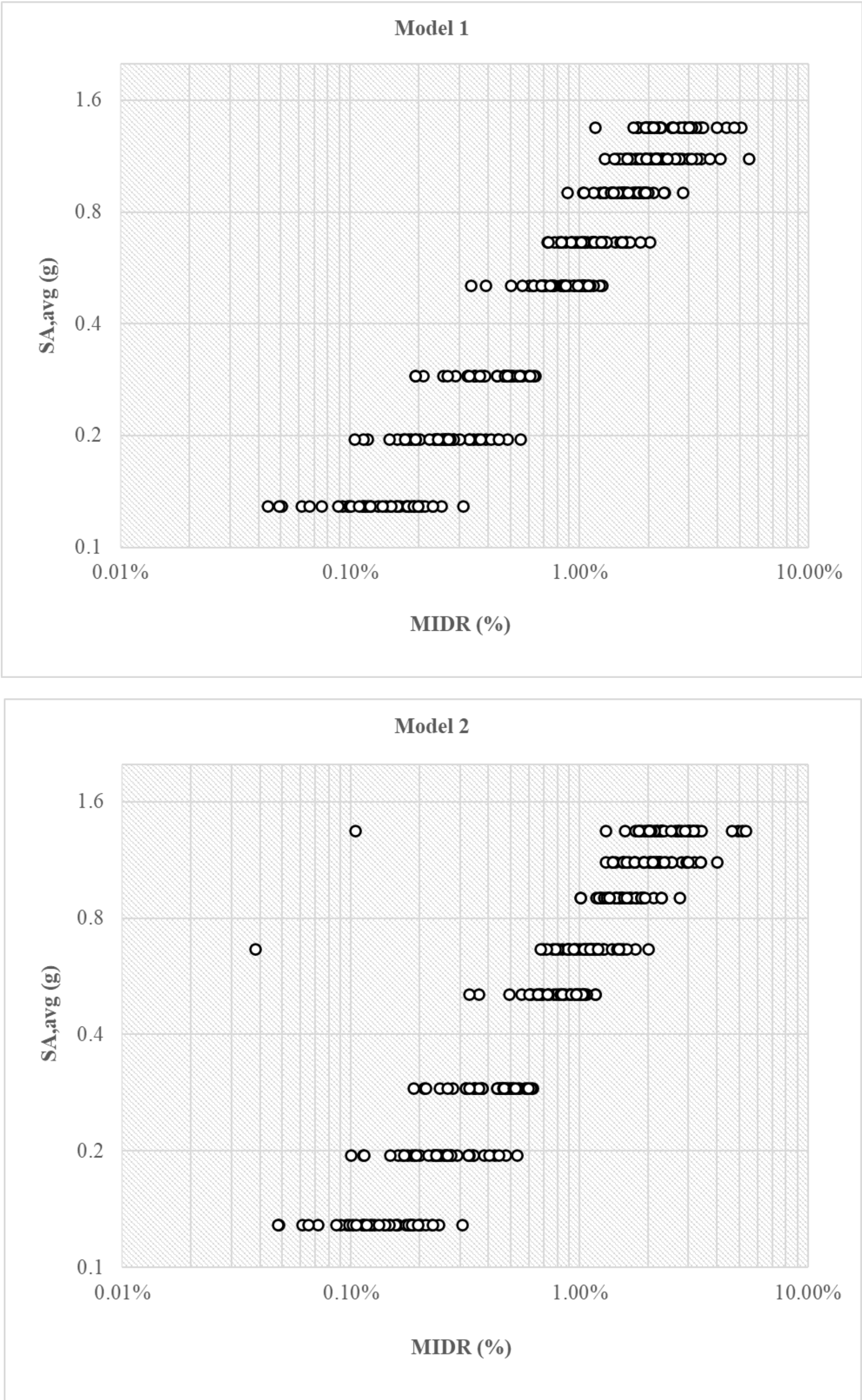

Figure 5.5 The MIDR results of Model 1 (top raw) and Model 2 (bottom row) based on MSA

5.3 Shear Check (Demand / Capacity ratio)

The building model in this study does not have a frame system and all lateral forces are resisted by the shear walls. The building can be considered as a core-wall system whose lateral load carrying members behave together. As described in Chapter 2, the shear behavior is modeled as linearly elastic (first model) and as a monotonic backbone curve (therefore nonlinear shear behavior is taken into consideration) in Model 2.

The brittle behavior resulting from shear deformation is an undesirable damage type by codes. Therefore, seismic design codes, such as those discussed in this thesis, do not permit brittle failure and set shear limits to prevent brittle failure. In this study, the shear limits are evaluated by considering the code provisions. For the range of hazard levels presented here, the NRHA results do not indicate any brittle failure.

The shear forces normalized by total structure weight are displayed in Figure 5.6 to Figure 5.9. As depicted by these figures, the most critical section in terms of shear forces is the ground story. As an example, the shear strain and shear force variations of one of the shear walls labeled as SW8 (see Figure 5.11 for its location in the plan view) are shown in Figure 5.10 and Figure 5.10, respectively. The wall does not exceed the allowable shear strain and force limits set by the codes studied in this thesis at DBE (475-year return period) and MCE (2475-year return period) hazard levels.

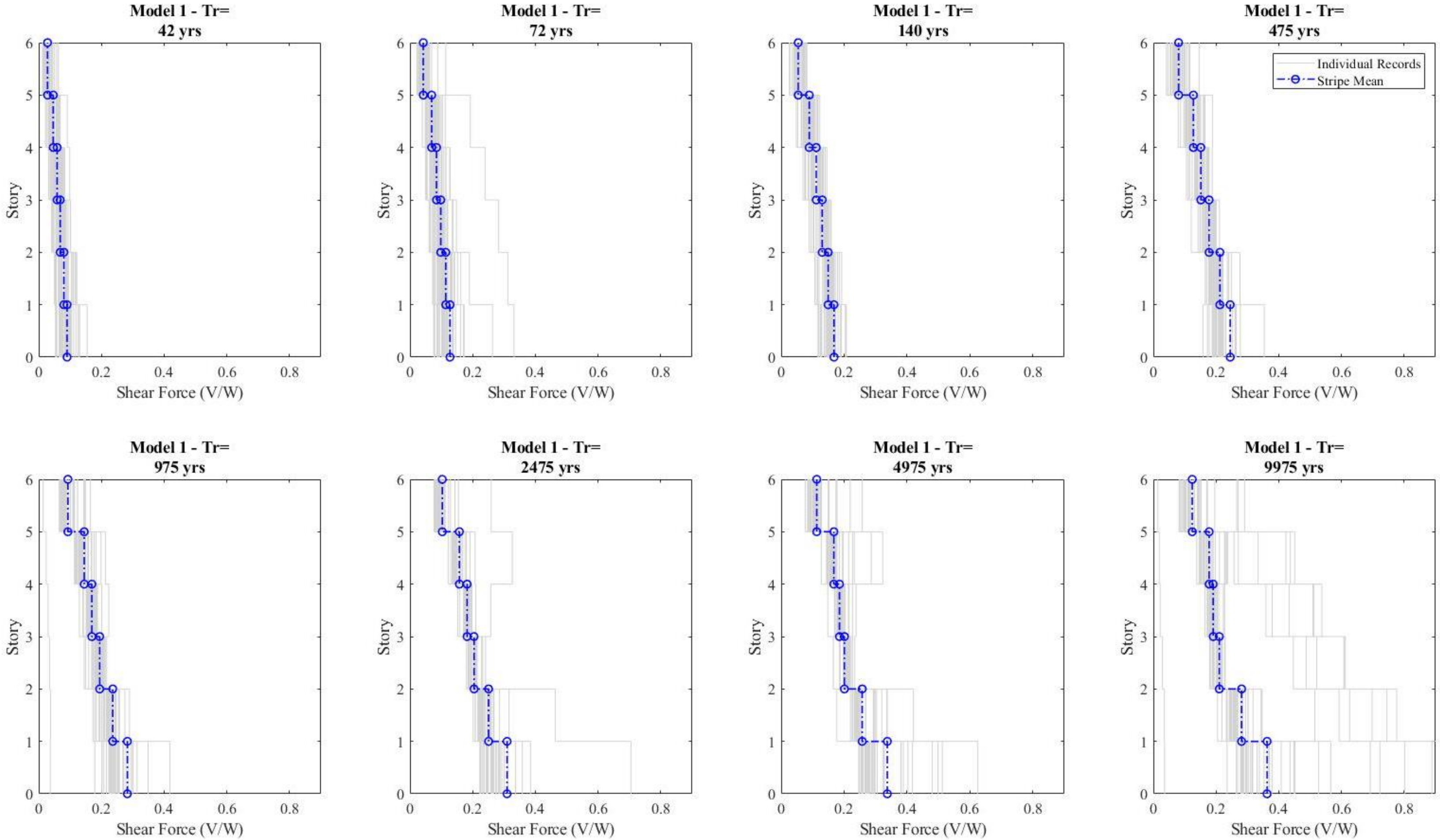

Figure 5.6 Normalized shear force distribution along with the height of the model building - Model 1, along x (long) direction

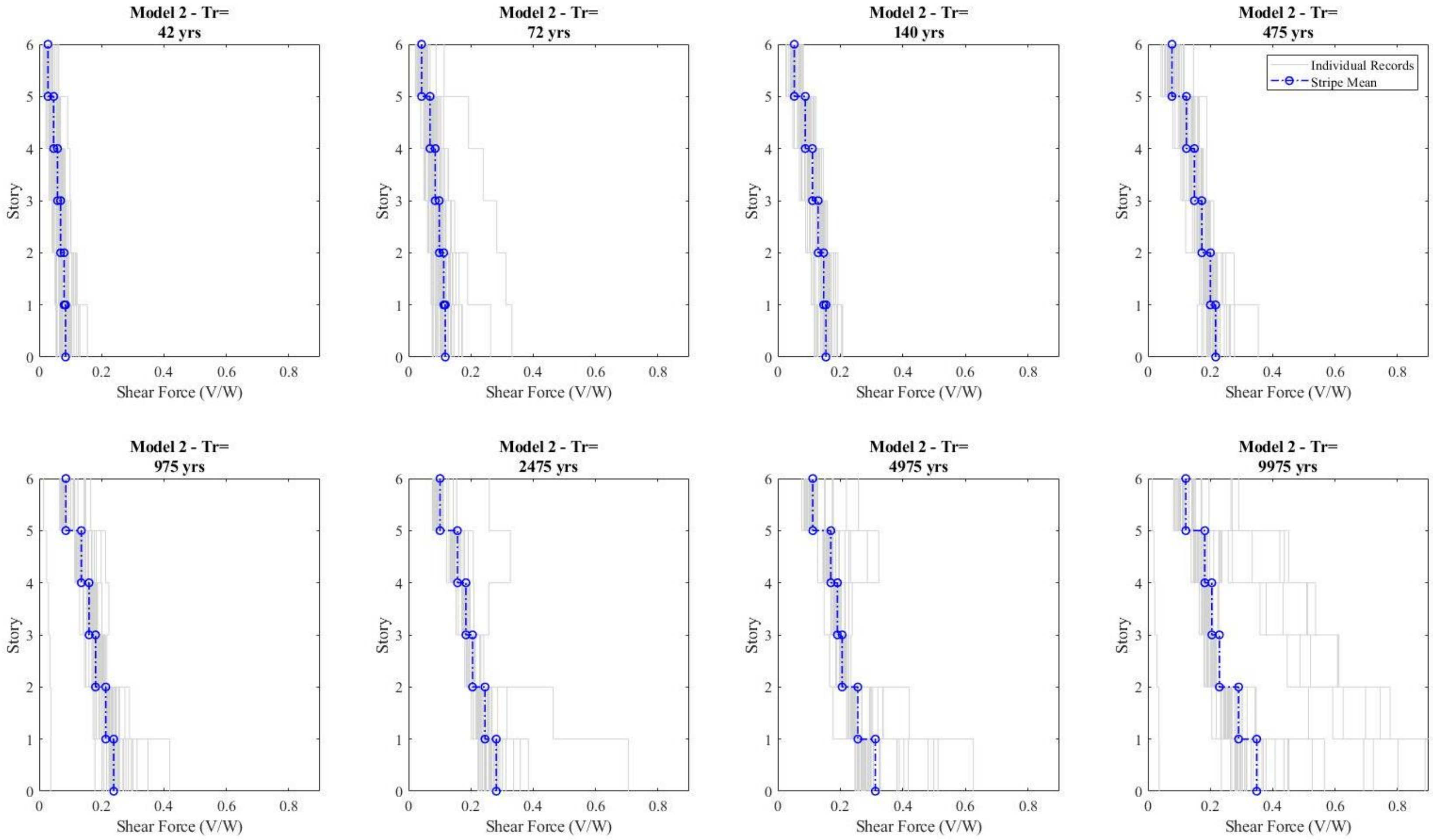

Figure 5.7 Normalized shear force distribution along with the height of the model building - Model 2, along x (long) direction

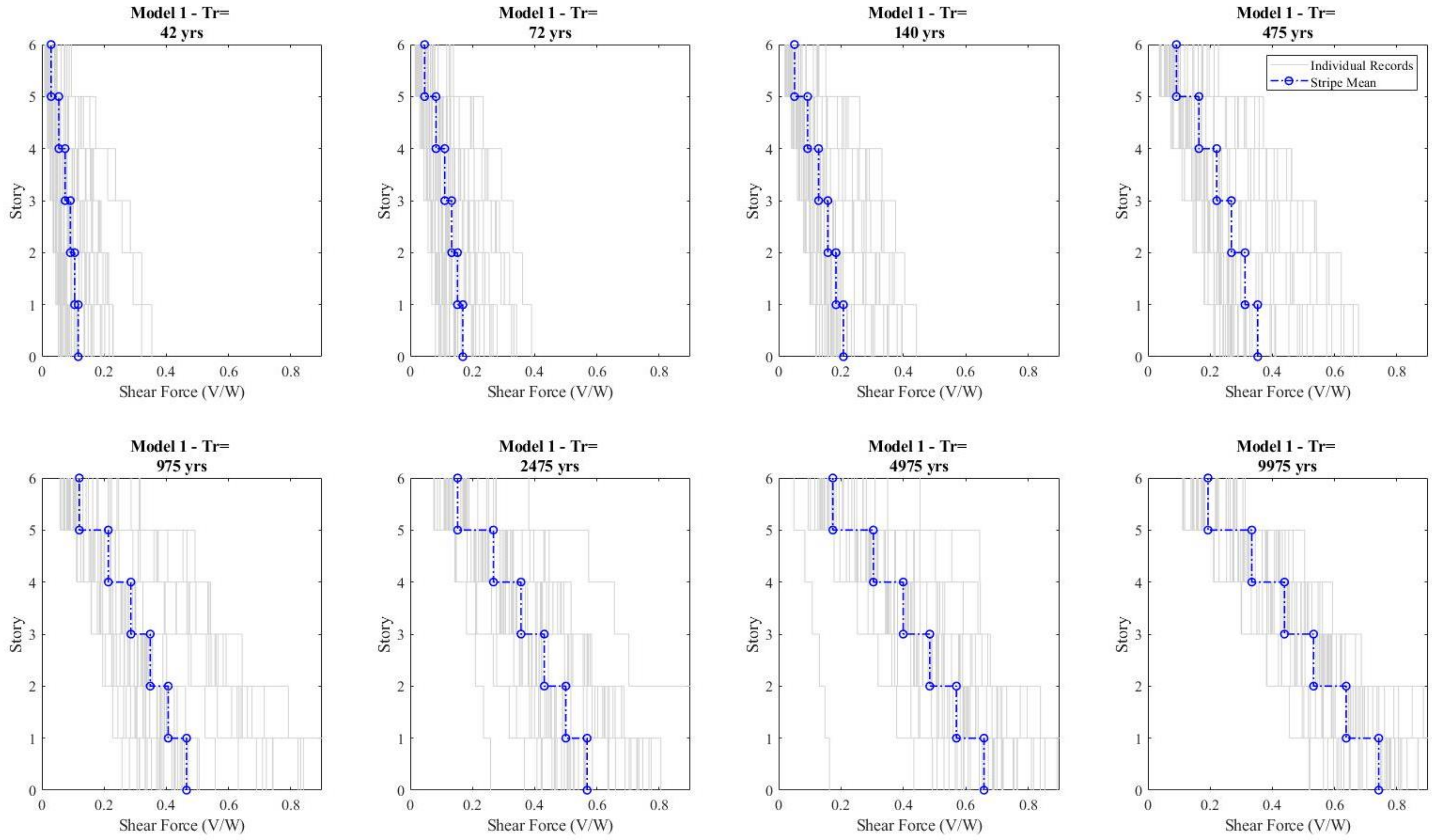

Figure 5.8 Normalized shear force distribution along with the height of the model building - Model 1, along y (short) direction

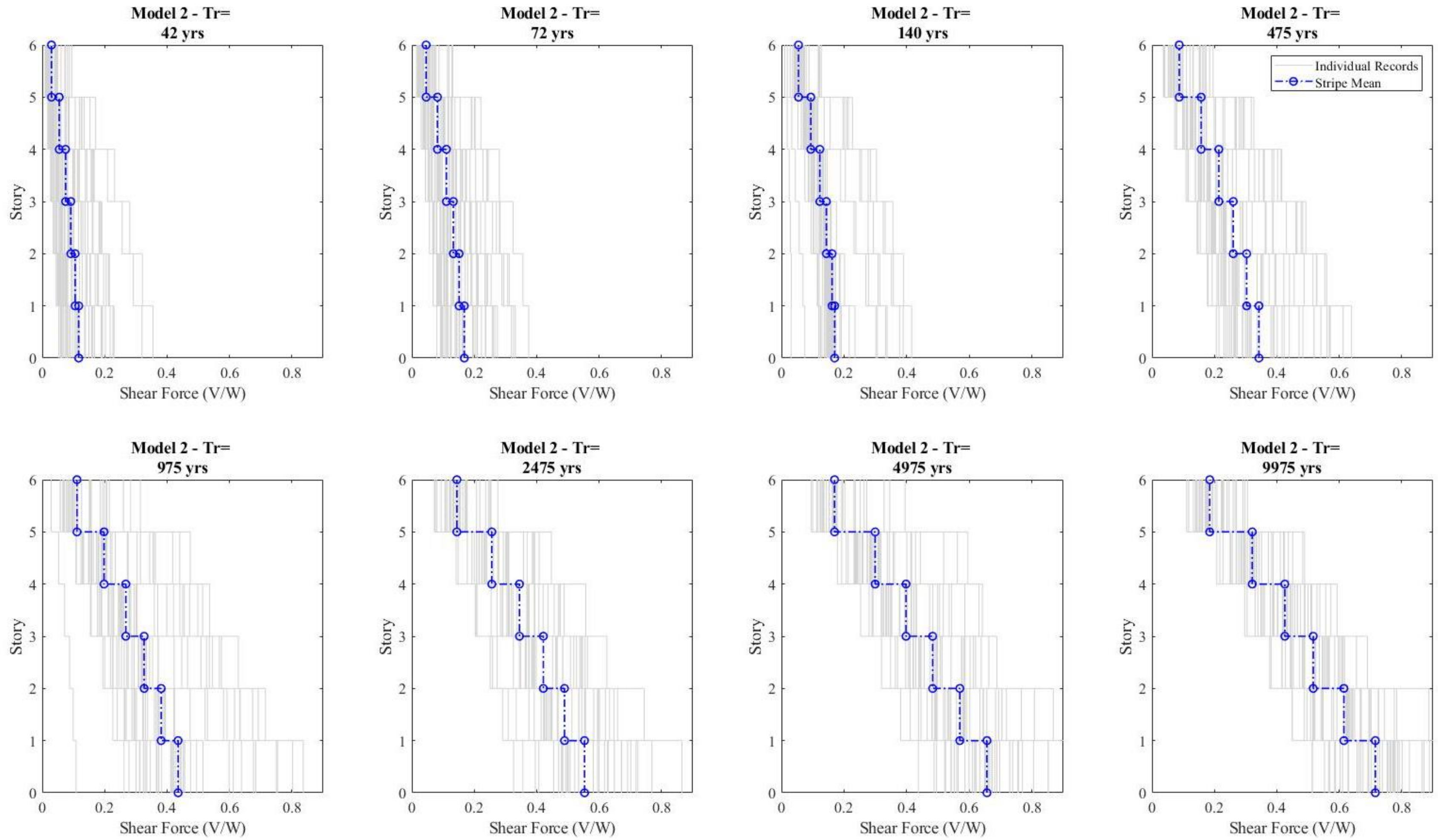

Figure 5.9 Normalized shear force distribution along the height of the model building - Model 2, along y (short) direction

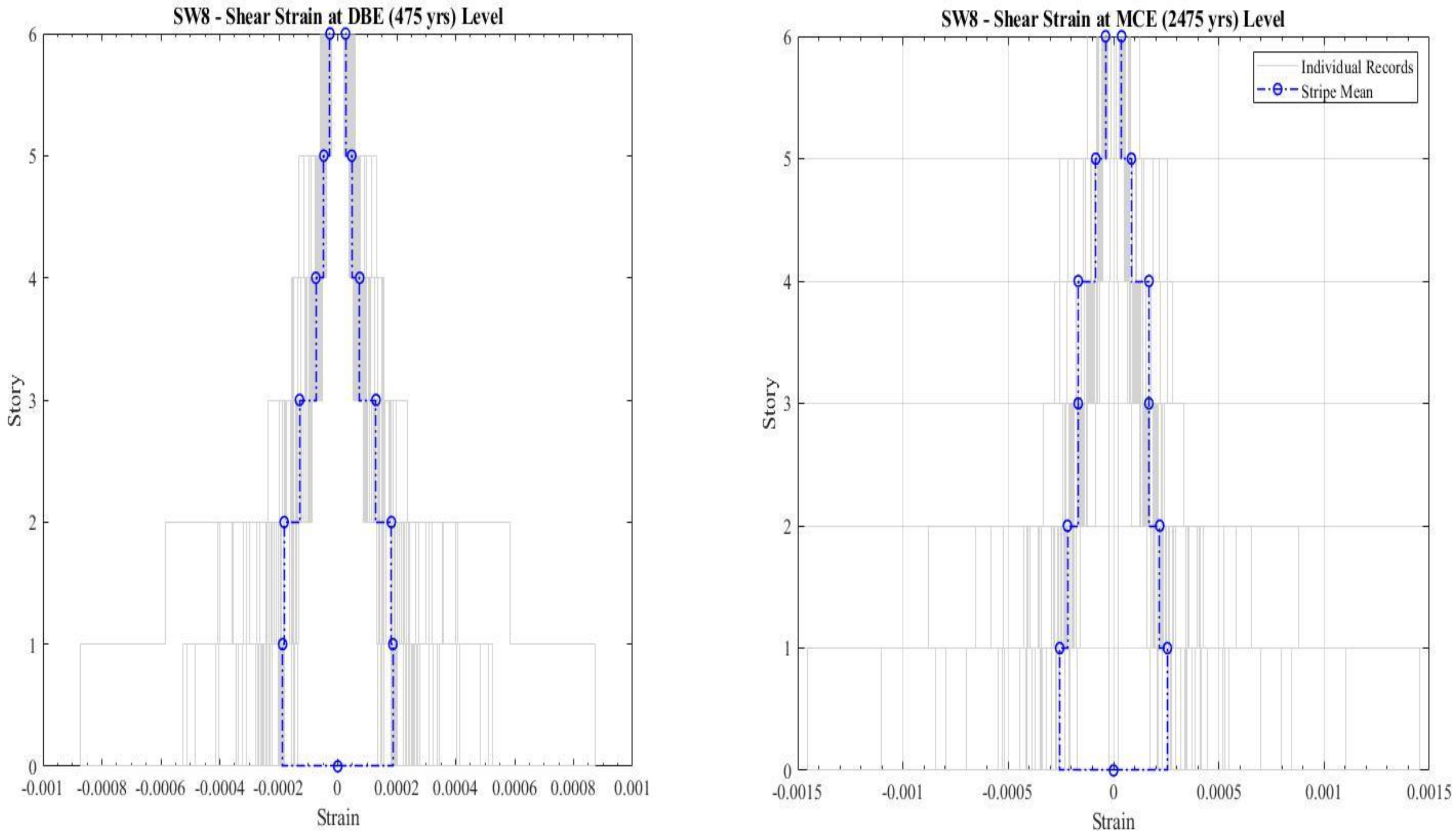

Figure 5.10 Shear strain distribution along the height of SW8 for 475-year (left panel) and 2475-year (right panel) hazard levels

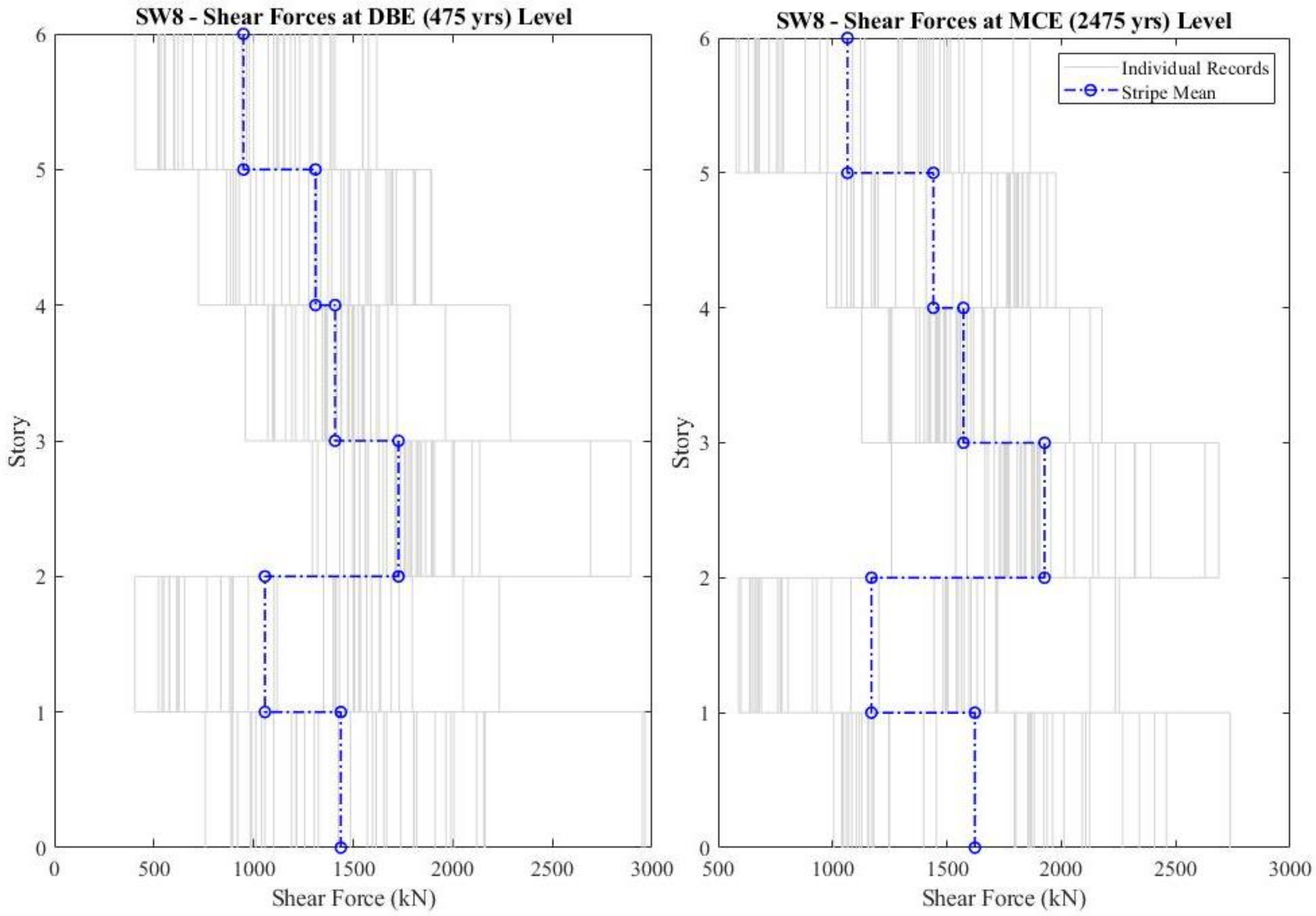

Figure 5.11 Shear force distribution along the height of SW8 for 475-year (left panel) and 2475-year (right panel) hazard levels

5.4 Detailed Assessment According to the Considered Design Codes in the Thesis

Performance assessment is done in terms of strain limits, plastic rotation, and chord rotation limits. These limits formulation and limits are described in Section 3.2 based on the provisions of codes and presented in Appendix C. When a structural element exceeds its performance level, the performance criteria are accepted as that performance level. For instance, Figure 5.13 shows the plan view of the model building showing the locations of SWs as well as the locations (labeled in circles) where strain data from NRHA are read. Figure 5.12 displays the strain data from NRHA. The red line denotes the damage state limit while black line denotes the tension and compression strain profiles along the heights.

The tunnel form building includes 8 different pairs of SWs (see the plan view in Figure 5.13). Their performance levels are calculated and presented in Appendix C. As described in Section 3.1, the Turkish earthquake code provides performance criteria only for cross-sections of structural members. The vertical WS elements are evaluated by means of strain limits. EC8 does not propose any global performance limit. hence the damage state limits are evaluated by means of chord rotation at the member level. ASCE/SEI 41-17 also evaluates performance assessment at the member level. Failure type is considered in performance assessment. If walls are dominated by flexure, plastic rotations limits are considered while shear dominates to walls, shear strain limits are taken into account to assess structural performance.

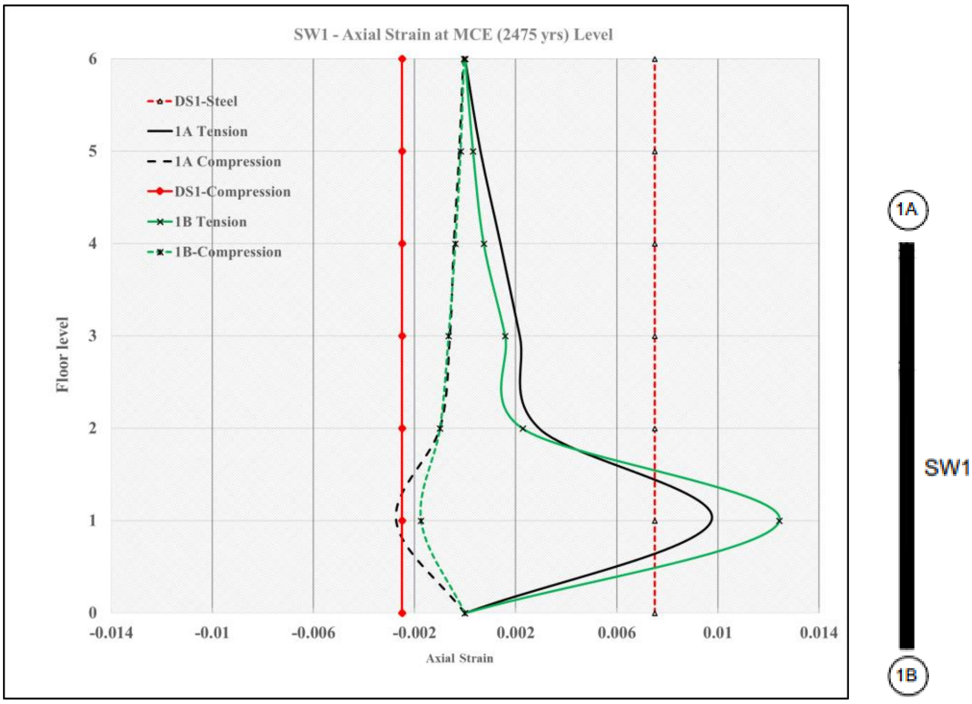

Figure 5.12 Tension and compression strain profiles along the heights of SW1 for 2475-year return period and corresponding damage state limits per provisions in TBEC-18.

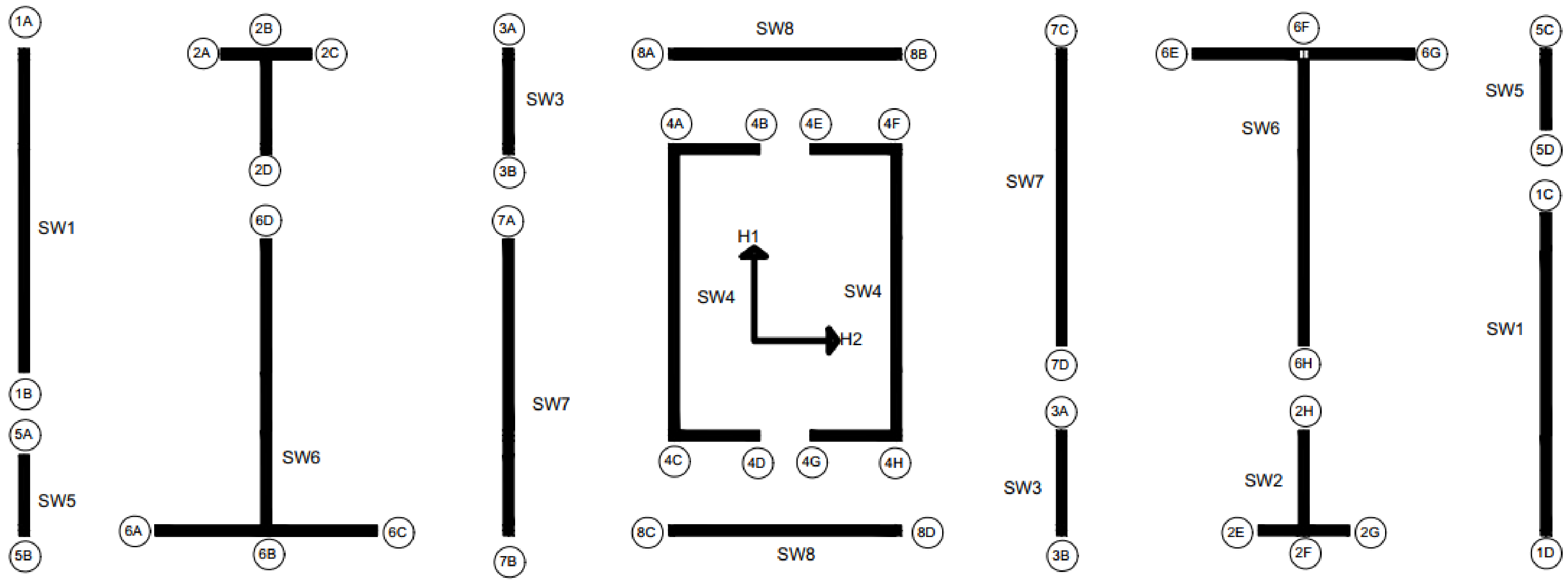

Figure 5.13 The plan view of the model building showing the locations of SWs as well as the loactions (labeled in circles) where strain data from NRHA are read.

In essence, the ground story is generally the most critical level for the tunnel form building (see Figure 5.12) studied in the thesis and upper stories can rarely be under high demands of ground motions due to higher modes effects and nonlinear shear behavior. (Figure 5.11). Shear forces directly affect the type of damage on walls. Some walls do not experience any damage because of the re-distribution of rigidity after the first cracking. Note that coupling beams in the model do not respond together with beams in a monotonic manner. Therefore, they do not contribute to the overall dynamic response of the model. This could be a modelling deficiency due to the choice of member sizes of coupling beams (the model assumes 25 cm by 60 cm coupling beams). Alternatively, if this is average size of coupling beam in Turkish construction practice then coupling beams in general do not contribute to the seismic behaviour of tunnel form building in Turkey.

6 FRAGILITY MODELS

6.1 Introduction

Seismic performance assessment of structure includes various types of steps. One of the most important steps is fragility analysis. There are several definitions to derive fragility functions such as expert judgment, experimental data, and collecting data from post-earthquake damage. (Baker,2015). Apart from these definitions, the Analytical approach is the most common method to derive fragility analysis. To derive the fragility curve, dynamic analysis is conducted to assess structural performance. Analytical computation to derive fragility proposed by Baker (2015) is to be adopted in this study.

The codes give different demand parameters to assess performance assessment such as strain limits, chord rotations, and plastic rotation. These parameters are taken into account as local performance levels while MIDR is considered as global performance levels.

6.2 Development of Fragility Curves

Fragility functions can be defined as the statistical distribution of damage as a function of a given demand parameter (see Figure 6.1). It can be formulated as a lognormal cumulative distribution function represented by median and standard deviation. (FEMA P-58-1, 2018). This formulation can be defined as:

$$F(D) = \emptyset\left(\frac{ln\left({}^{D}/_{\mu}\right)}{\beta}\right) \qquad 6.1$$

where $F(D)$ is probability conditioned on demand parameter, $\emptyset$ is standard normal cumulative function and μ and β are median and standard deviation respectively. This formulation is the main concept of the derivation of fragility curves.

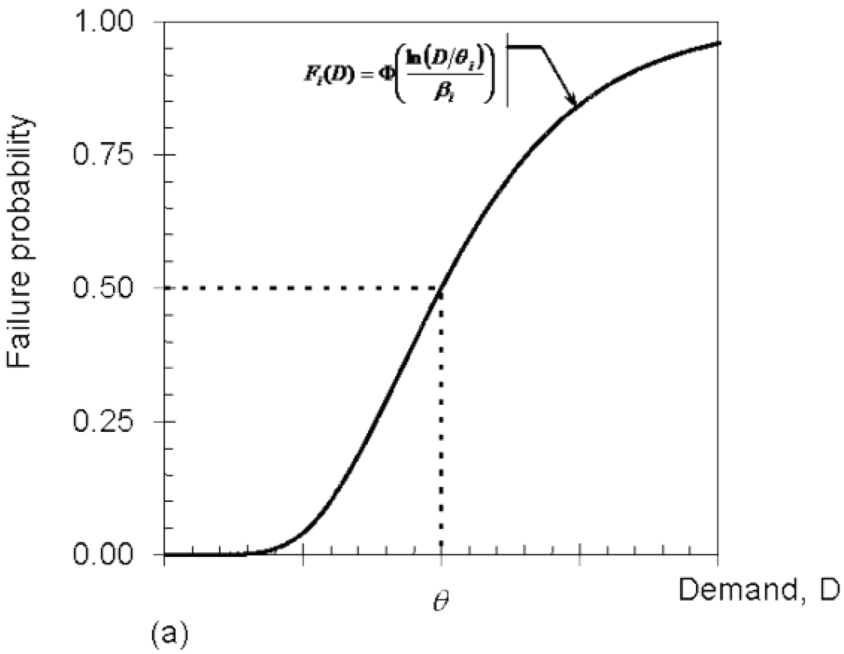

Figure 6.1 The representation of fragility curves (taken from FEMA P-58-1, (2018))

As the discussed previous section, the analytical procedure proposed by Baker (2015) is adopted. The nonlinear analysis can be conducted in several ways such as Incremental Dynamic Analysis (IDA) and Multiple Stripe Analysis (MSA). IDA proposed by Vamvatsikos and Cornell (2002) is the first analysis type where a suite of ground motions is scaled up or down incrementally until global collapse occurs. Another approach is to MSA where a set of ground motions conditioned on specific IM levels is performed. The results of the study (Baker, 2015) show that deriving the fragility curve based on MSA is more efficient than the one based on IDA.

6.3 Multiple Stripes Analysis

The dynamic analysis based on MSA was conducted to assess the structural performance of tunnel form building. The three different damage state levels based on the requirement of codes are selected to define the damage region. These types are categorized into three groups and followed the procedure proposed by Baker (2015) to develop the fragility curve of tunnel form building representing low stories tunnel form building in Turkey. A technique of deriving fragility curve is summarized as follow:

In this method, the maximum likelihood fitting technique is used to fit this type of data. First, to compute failure probability given demand parameter can be calculated in Eqn. 6.2.

The study (Baker, 2015) states that the fitting fragility curve to observe data from NRHA by using maximum likelihood estimation is a good alternative statistical approach.

$$P(DS > ds\ I\ IM = im) = \Phi\left(\frac{\ln\left({im}/{\theta}\right)}{\beta}\right) \tag{6.2}$$

The probability of observing the damage z_j exceeding damage state level out of n_j ground motions for a given in IM=im is presented as binominal distribution. (Eqn. 6.3). The main purpose is to compute the prediction of p_j leading to collapse to structure.

$$P\left(z_j\ collpase\ in\ n_j\ ground\ motions\right) = \binom{n_j}{z_j} p_j^{z_j}\left(1 - p_j\right)^{n_j - z_j} \tag{6.3}$$

Next, the product of binomial probabilities (Eqn. 6.3) gives the final probability of intensity levels when obtained data from MSA. To compute the overall probability, the product of likelihood estimations can be taken for each IM level. overall probability can be computed as shown in Eqn. 6.4.

$$Likelihood = \prod_{j=1}^{m} \binom{n_j}{z_j} p_j^{z_j}\left(1 - p_j\right)^{n_j - z_j} \tag{6.4}$$

Then, Eq 6.2 is substituted to p_j, the pragility parameters is obtained as:

$$Likelihood = \prod_{j=1}^{m} \binom{n_j}{z_j} \Phi\left(\frac{ln\left(x_j/\theta\right)}{\beta}\right)^{z_j}\left(1 - \Phi\frac{ln\left(x_j/\theta\right)}{\beta}\right)^{n_j - z_j} \tag{6.5}$$

To maximize the logarithm of the likelihood function is computed as Eqn. 6.6. A fragility curve will be derived by using this approach.

$$\left\{\hat{\theta}, \hat{\beta}\right\} = \arg max_{\theta,\beta} \sum_{j=1}^{m} \left\{ ln\binom{n_j}{z_j} + z_j\ ln\Phi\left(\frac{ln\left(\frac{x_j}{\theta}\right)}{\beta}\right) + \left(n_j - z_j\right) ln\left(1 - \Phi\left(\frac{ln\left(\frac{x_j}{\theta}\right)}{\beta}\right)\right)\right\} \tag{6.6}$$

6.4 Fragility Results

The probability of exceedance given intensity levels is computed based on MSA results. The fragility curves corresponding to strain limits, chord rotation, and plastic rotation are listed in Table 6.1 and displayed in Figure 6.2, Figure 6.3, and Figure 6.4 respectively.

The observations obtained from fragility curves illustrated in Figure 6.2 to Figure 6.4 are as follows:

- Demand parameter plays a more important role to derive fragility functions. It directly affects the probability of exceeding damage states in all cases.

- The increase of shear wall area leads to a decreased probability of failure. The long direction having a smaller shear all area dominates the probability of failure. The same shear wall ratio in two horizontal directions should be investigated how to affect the probability of failure.

- Tunnel form building does not reach collapse region in DBE (475 -year return period.) level. There is also no significant damage at the DBE intensity level in all cases.

- The strain limit is more comprehensive than chord rotation and plastic rotation in walls when compared to fragility curves. It should be re-defined new damage state levels for tunnel form building.

- The local performance level is more comprehensive and efficient compared to the global performance level however, it leads to time-consuming by evaluating the structural performance level of tunnel form building.

- The secondary elements damages lead to decreasing of the probability of IO because the rigidity of beam elements is weaker compared to vertical elements.

Table 6.1 The fragility parameters of tunnel form building based on local performance

Codes/DS	IO		LS		CP	
	μ	β	μ	β	μ	β
TBSDC-18	0.488	0.035	0.868	0.21	1.013	0.238
EC8-3	0.336	0.25	1.415	0.221	1.77	0.284
ASCE/SEI 41-17	0.518	0.2	1.163	0.25	1.372	0.252

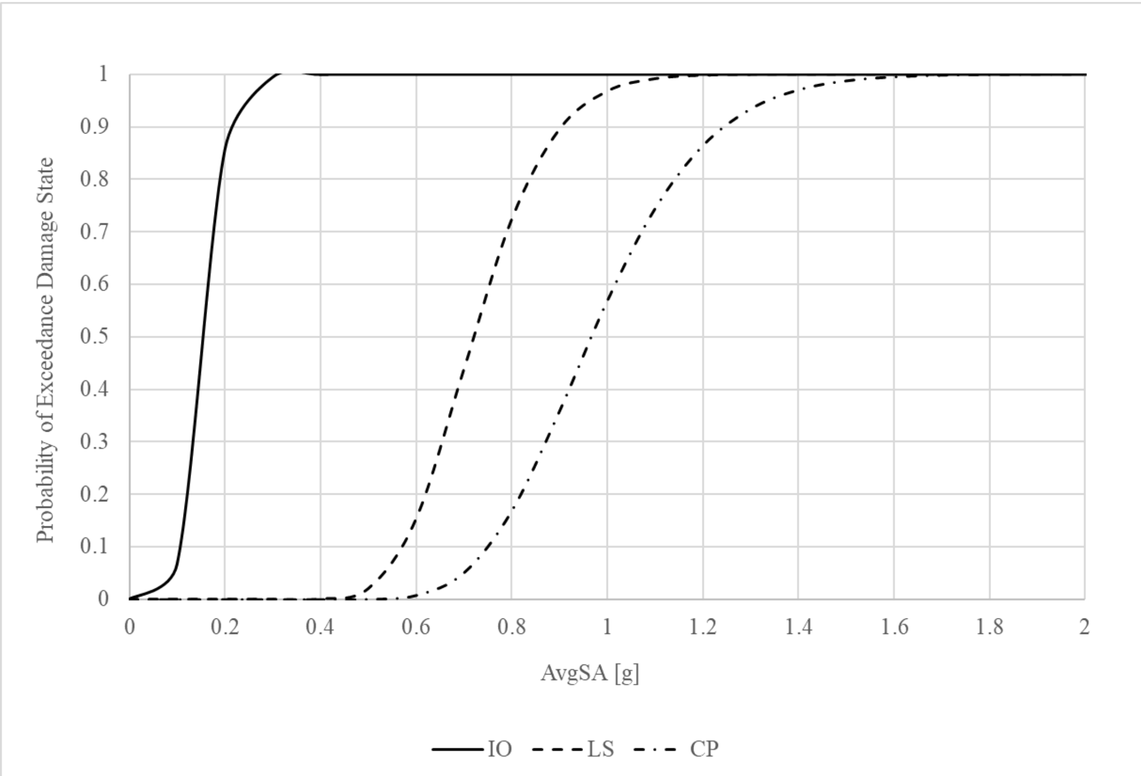

Figure 6.2 The fragility curve for TBSDC-18 based on strain limits

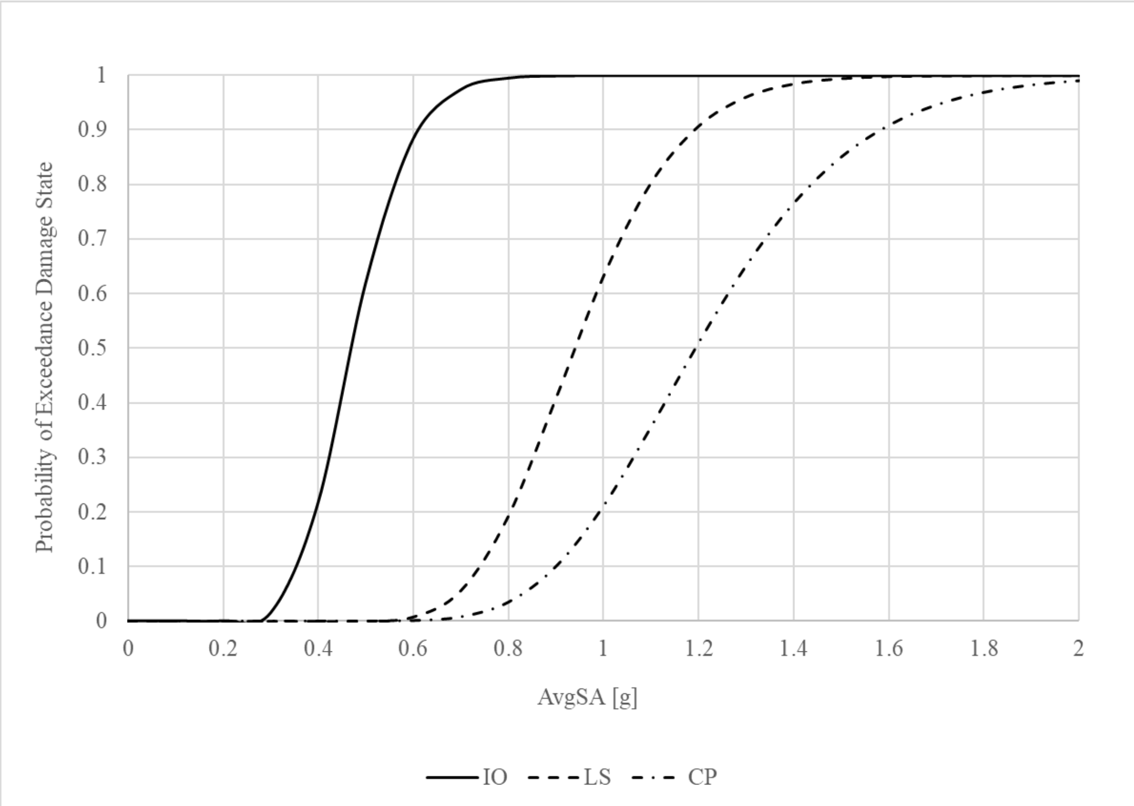

Figure 6.3 The fragility curve for EC8-3 based on chord rotation

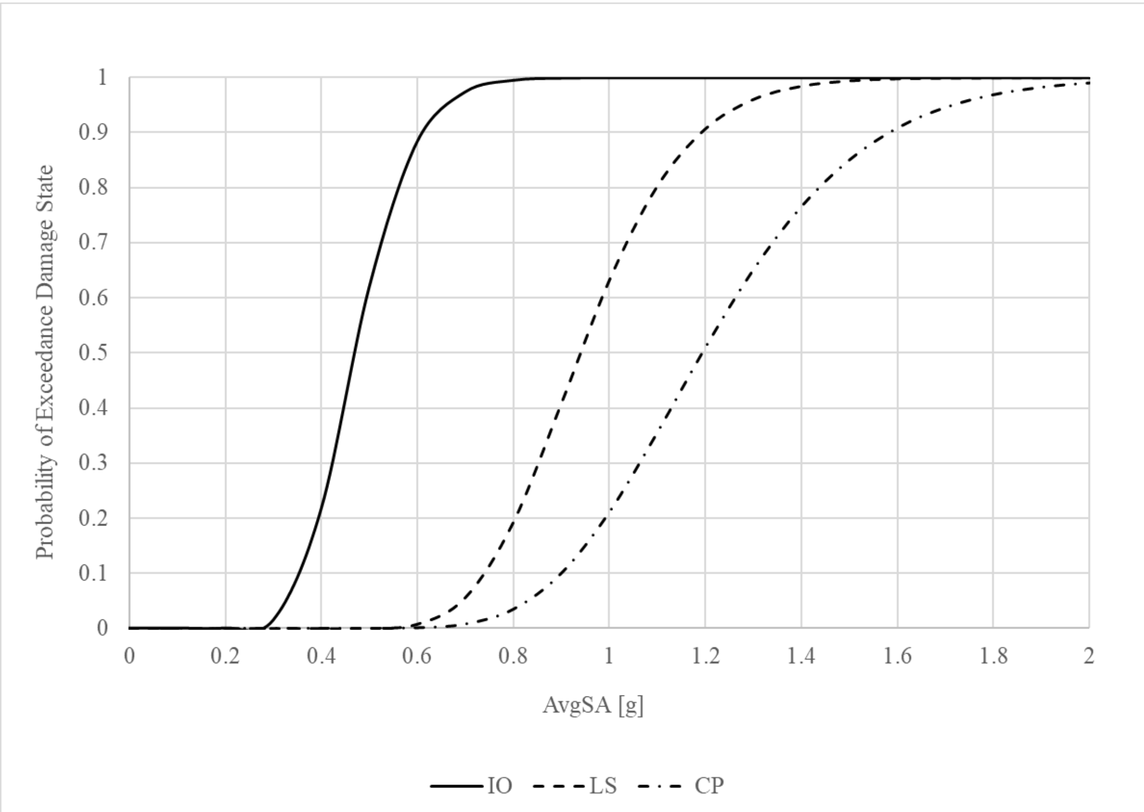

Figure 6.4 The fragility curve for ASCE/SEI 41-17 based on plastic rotations

6.4.1 Global MIDR Limits

It is more effective and realistic to develop fragility curves based on local performance limits. It is also easier to derive a fragility curve for one building. When it comes to large building stock, time-consuming will be a grave problem. Hence, the global acceptance limit should be investigated. The global acceptance criteria should also be appropriate with intensity measures in terms of sufficiency, efficiency, and practicality. The MIDR limits are computed for collapse limits based on the response limit of codes. When the first collapse that occurred in the wall is observed, the MIDR limit exceeds its level. The final fragility curve is listed in Table 6.2 and displayed in Figure 6.7, Figure 6.6, and Figure 6.7. As a result, the fragility curve based on local performance limits is not similar to the one based on global performance limits. This conclusion leads to the need for new demand parameter limitations considering only tunnel form buildings.

Table 6.2 The fragility parameters of tunnel form building based on global performance

Codes/DS	IO		LS		CP	
	μ	β	μ	β	μ	β
TBSDC-18	0.42	0.185	0.78	0.18	0.95	0.212
EC8-3	0.15	0.27	0.72	0.178	0.967	0.197
ASCE/SEI 41-17	0.47	0.205	0.94	0.185	1.194	0.22

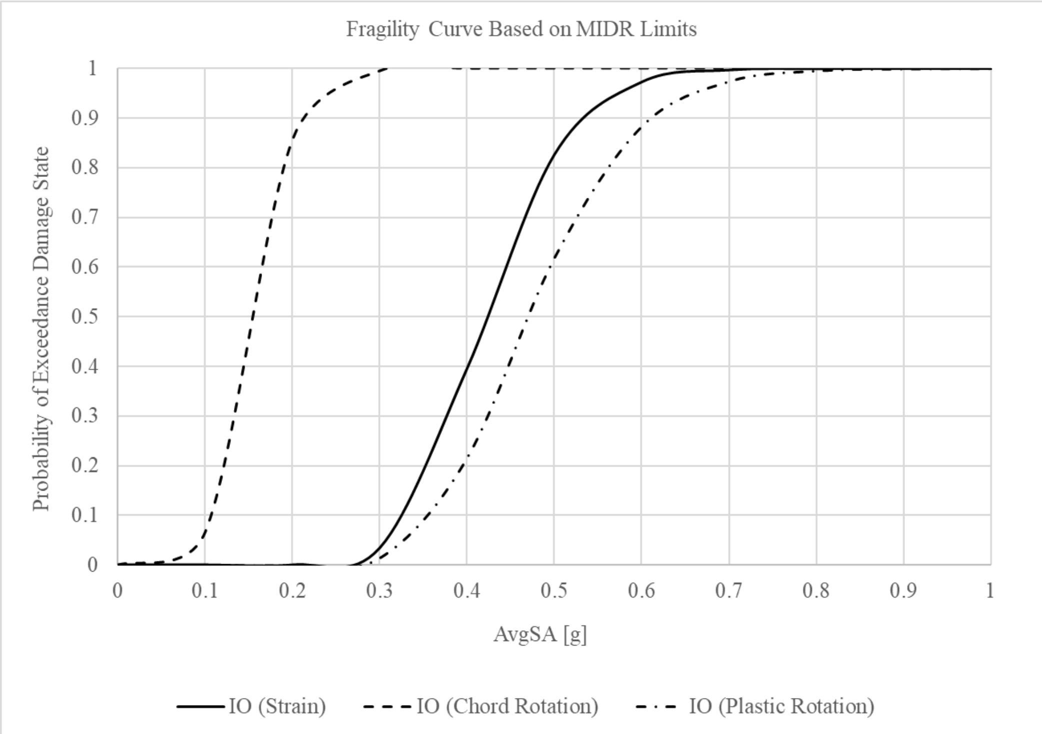

Figure 6.5 Fragility curve based on global performance limits at IO damage state

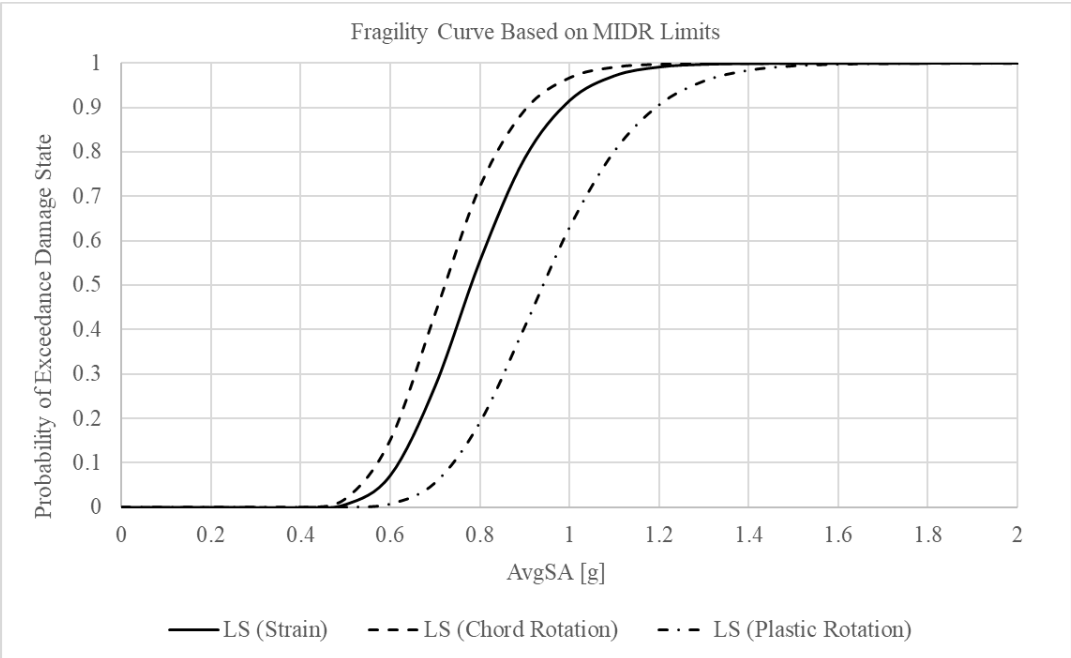

Figure 6.6 Fragility curve based on global performance limit at LS damage state

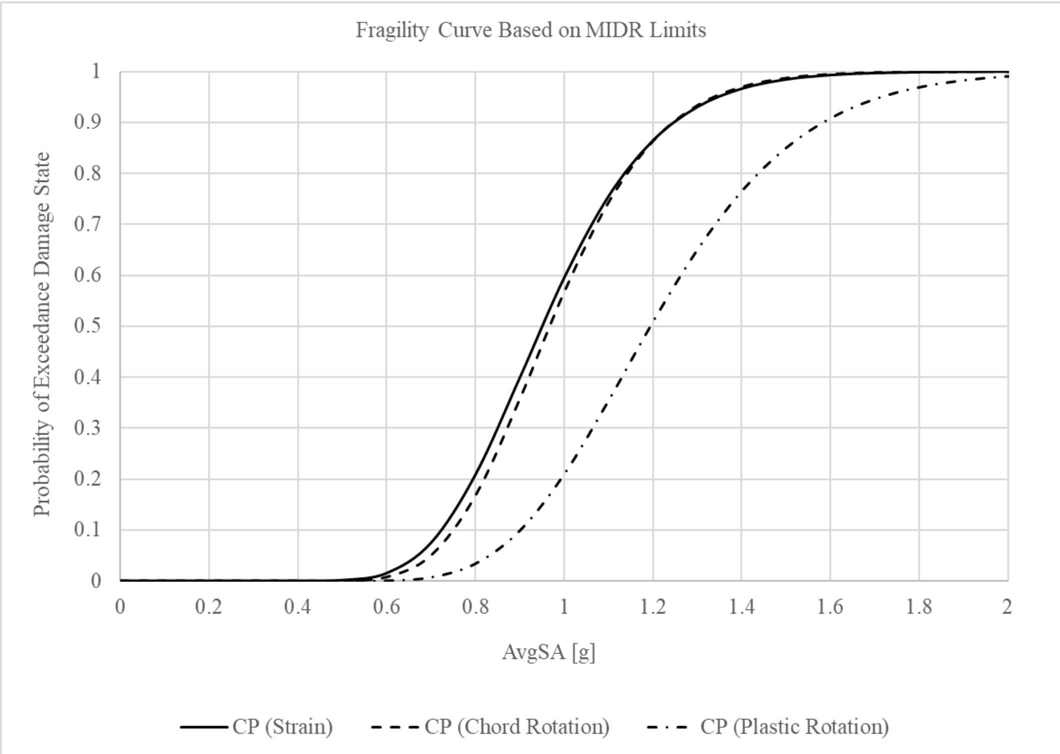

Figure 6.7 Fragility curve based on global performance limit at CP damage state

7 SUMMARY AND CONCLUSION

7.1 Summary

The main goal of this dissertation is to derive fragility curves of a 6-story tunnel form building representing the residential building stocks in Turkey. The residential building is categorized in terms of its number of stories, shear wall area, and reinforcement ratio statistically. Consequently, the tunnel form building is categorized under four classes with different number stories in order to represent the stock of buildings in Turkey. The first group building including 6-story is investigated in this study.

Firstly, the first group called as mid-rise is designed in accordance with the information obtained from statistical research. The short direction is more shear wall area than the long direction. Then, the guidelines and codes are investigated to establish a mathematical model in structural software. The fiber model is used for wall elements whereas, the lumped plasticity model is preferred to model beam elements. Shear behavior is considered both elastic and inelastic.

The intensity measure (IM) is investigated in terms of efficiency, sufficiency, and practicality. The average spectral acceleration is selected as IM. The selection of ground motion procedure is followed by the study of Curic (2021). Eight out of fourteen different intensity levels in his thesis are considered. The location of Ataşehir is selected for seismic hazard assessment. After PSHA analysis, twenty different records are selected for each intensity level. The reader can find all other details in the Curic study (2021).

The two different mathematical models are designed to follow the requirements based on guidelines and codes. Another reason to design two different models is to represent shear inelastic behavior. After conducting PSHA analysis, the response limits are defined based on the code requirements. The pushover, push-pull and modal analysis is conducted to determine the behavior of building and cyclic degradation curve to derive SDOF model and to compute top lateral drift exceeding damage limit states. The nonlinear static analysis is conducted by subjecting the loads compatible with the first modes of the structure.

The NRHA is conducted using 640 ground motions under eight different intensity levels. The axial strain in walls, chord rotation, and plastic rotation is computed to assess structural performance levels. The shear demand capacity does not exceed the limits of shear walls.

Finally, the fragility curve is derived by using an MLE method proposed by Baker (2015) based on MSA results. The strain limits, chord rotation, and plastic rotation are considered as local performance levels while maximum intensity drift is considered as global performance limits.

7.2 Conclusions

The observation obtained from this study is as follows:

- This building is limited to the 6-story building (first group). The other groups representing the stock of tunnel form buildings in Turkey should be investigated and compared in terms of intensity measures and demand parameters.
- The intensity measure is selected as Average spectral acceleration. Different intensity measures such as PGV, $Sa(T_1)$ should be investigated whether it is compatible with tunnel form buildings. The correlation between AvgSa and PGV/PGA should be investigated in future studies.
- Engineering demand parameter plays a more important role to derive fragility functions. The global and local performance levels are not similar compared to fragility curves. A new demand parameter for both global and local levels should be developed.
- The tunnel form building performs well under the DBE (475 -year return period) and MCE (2475 -year return period) levels. It can be more economic than other types of buildings.
- The shear effect has a significant effect on structural behaviour. the brittle behaviour is not observed under the MCE level, however, shear force effects lead to damage shifting upper stories especially in a short direction.
- The linked beams are more vulnerable than walls and they exceed collapse performance levels before walls exceed lower performance levels.

REFERENCES

Akkar S., Sandıkkaya MA. and Bommer JJ. (2014). Empirical ground-motion models for point- and extended-source crustal earthquake scenarios in Europe and the Middle East. Bulletin of Earthquake Engineering, 12, 359–387. https://doi.org/10.1007/s10518-013-9461-4

ASCE/SEI 41-17, (2017). Seismic Evaluation and Retrofit of Existing Buildings. American Society of Civil Engineers, USA

ACI 318-11. (2011). Building Code Requirements for Structural Concrete and Commentary, American Concrete Institute Committee 318

Applied Technology Council. (2010). Guidelines on modeling and acceptance criteria for seismic design and analysis of tall buildings. ATC-72-1, Redwood City, California

Baker JW (2015). Efficient analytical fragility function fitting using dynamic structural analysis. Earthquake Spectra, 31, 1, 579-599.

Balkaya C., and Kalkan E. (2003). Seismic design parameters for shear-wall dominant building structures. Guanajuato: The 14th National Congress on Earthquake Engineering

Balkaya C., and Kalkan E. (2004). Seismic vulnerability, behavior and design of tunnel form building structures. Engineering Structures, 26, 14, 2081–2099

Beheshti-Aval SB, Mohsenian V and Sadegh KH. (2018). Seismic Performance-Based Assessment of Tunnel Form Building Subjected to Near and Far Fault Ground Motions. Asian Journal of Civil Engineering. 19. DOI: 10.1007/s42107-018-0009-4.

Bianchini M., Diotallevi P., and Baker JW. (2009). Prediction of inelastic structural response using an average of spectral accelerations. 10th international conference on structural safety and reliability (ICOSSAR09). 13-17.

Computer and Structures, Inc. (2018). Perform-3D V7: Nonlinear analysis and performance assessment for 3D structures, Berkeley, CA.

Curic H., (2021). Scalar and vector probabilistic seismic risk assessment procedures and their implementation for a simplified mid-rise RC tunnel form building, Boğazici University, MSc Thesis.

Eads L., Miranda E., and Lignos D. (2015). Average spectral acceleration as an intensity measure for collapse risk assessment. Earthquake Engineering & Structural Dynamics, 44,2057-2073.

European Committee for Standardization (EC8-3), (2005). Eurocode 8: Design of structures for earthquake resistance - Part 3: Strengthening and repair of buildings. European Standard, EC-8-3, BS EN 1998–3, Comité Européen de Normalisation, Brussels, Belgium.

FEMA-P-58-1, Seismic Performance Assessment of Buildings, Federal Emergency Management Agency, Washington, DC., 2018.

Filippou FC., Popov EG., and Bertero VV., (1983). Effects of bond deterioration on hysteretic behavior of reinforced concrete joints. UCB/EERC Report 83/19, University of California, Berkeley, California.

Görgülü O., and Taşkın B. (2015). Numerical simulation of RC infill walls under cyclic loading and calibration with widely used hysteretic models and experiments. Bulletin of Earthquake Engineering, 13, 2591–2610. DOI 10.1007/s10518-015-9739-9.

Hancilar U. and Cakti E. (2015) Fragility functions for code complying RC frames via best correlated IM-EDP pairs. Bulletin of Earthquake Engineering, 13, DOI:10.1007/s10518-0159775-5

Ibarra LF, Medina RA, Krawinkler H (2005). Hysteretic models that incorporate strength and stiffness deterioration. Earthquake Engineering and Structural Dynamics 34, 12, 1489–1511

IBB-KRDAE (2020) İstanbul İli Olası Deprem Kayıp Tahminlerinin Güncellenmesi Projesi, İstanbul Büyükşehir Belediyesi, Deprem Risk Yönetimi ve Kentsel İyileştirme Daire Başkanlığı, Deprem ve Zemin İnceleme Müdürlüğü.

Kent DC, Park R (1971) Flexural members with confined concrete. Journal of the Structural Division, 97, 7, 1969–1990

Kohrangi M., Bazzurro P., Vamvatsikos D. (2016). Vector and Scalar IMs in Structural Response Estimation: Part I – Hazard Analysis. Earthquake Spectra. 32.

Kohrangi M, Bazzurro P, Vamvatsikos D. (2016). Vector and Scalar IMs in Structural Response Estimation, Part II: Building Demand Assessment. Earthquake Spectra;32, 3, 1525-1543.

Kohrangi M., Bazzurro P., Vamvatsikos D., and Spillatura A. (2017). Conditional spectrum-based ground motion record selection using average spectral acceleration. Earthquake Engineering & Structural Dynamics. 46. DOI:10.1002/eqe.2876.

Kolozvari K., Orakcal K., and Wallace JW. (2015). Shear-Flexure interaction modeling of reinforced concrete structural walls and columns under reversed cyclic loading. Pacific Earthquake Engineering Research Center, University of California, Berkeley.

Kolozvari, K., Piatos G., and Beyer K., (2017). Practical nonlinear modeling of U-shaped reinforced concrete walls under bi-directional loading. 16th World Conference on Earthquake, Santiago Chile, Paper No: 2503

Kolozvari K., Orakcal K., Wallace JW. (2018). New opensees models for simulating nonlinear flexural and coupled shear-flexural behavior of RC walls and columns. Computers & Structures, 196, 246-262. ISSN 0045-7949,

Kolozvari, K., Kalbasi, K., Orakcal, K. Massone LM., and Wallace J. (2019). Shear–flexure-interaction models for planar and flanged reinforced concrete walls. Bulletin of Earthquake Engineering, 17, 6391–6417.

LATBSDC, (2020). An Alternative Procedure for Seismic Analysis and Design of Tall Buildings Located in the Los Angeles Region. Los Angeles, CA.

Lin T., Haselton C., and Baker J., (2013). Conditional spectrum-based ground motion selection. Part I: Hazard consistency for risk-based assessments. Earthquake Engineering & Structural Dynamics. 42. 10.1002/eqe.2301.

Lu X, Lu X, Guan H, Ye L. Comparison and Selection of Ground Motion Intensity Measures for Seismic Design of Super High-Rise Buildings. Advances in Structural Engineering. 2013;16(7):1249-1262. doi:10.1260/1369-4332.16.7.1249

Mander JB, Priestley MJN, Park R (1988) Theoretical stress-strain model for confined concrete. Journal of the Structural Division, 114, 8, 1804–1826.

Massone LM, Orakcal K, Wallace JW. (2006). Modeling flexural/shear interaction in RC walls, ACI-SP-236, deformation capacity, and shear strength of reinforced concrete members under cyclic loadings. Farmington Hills (MI): American Concrete Institute, 127–50

Menegotto M., and Pinto P., (1973). Method of analysis for cyclically loaded RC plane frames including changes in geometry and nonelastic behavior of elements under combined normal force and bending. Proceedings of Symposium on Resistance and Ultimate Deformability of Structures Acted on by Well-Defined Repeated Loads, IABSE Reports, 13, 2557-2573

Mohsenian V., Nikkhoo A., Rostamkalaee S., Moghadam SA., and Hejazi F.. (2020). The seismic performance of tunnel-form buildings with a non-uniform in-plan mass distribution. Structures. 29. 993-1004. 10.1016/j.istruc.2020.11.063.

Orakcal K. and Wallace, JW. (2004). Modeling of slender reinforced concrete walls, 13th World Conference on Earthquake Engineering, 18, 1, 141-143.

Orakcal K., and Wallace JW., (2006). Flexural modeling of reinforced concrete walls-Experimental verification. Structural Journal, ACI, 103, 2, 196-206

Orakcal K., Massone LM., and Wallace JW. (2009). Shear strength of lightly reinforced wall piers and spandrels. Structural Journal, ACI, 106, 4, 455-465.

OpenSees, Open System for Earthquake Engineering Simulation, Pacific Earthquake Engineering Research Center, University of California, Berkeley, California, online at http://opensees.berkeley.edu/.

Perform3D User Guide, (2006). Nonlinear analysis of performance assessment for 3D structures. Computers and Structures, Inc.

Deierlein G. Reinhorn A., and Willford M. (2010). Nonlinear structural analysis for seismic design- a guide for practicing Engineers. NEHRP Seismic Design Technical Brief No. 4, NIST GCR 10-917-5, National Institute of Standards and Technology, Gaithersburg, MD, USA.

Shome, N. and Cornell, CA., Probabilistic seismic demand analysis of nonlinear structures, Report No. RMS-35, RMS Program, Stanford University, Stanford, CA, 1999.

Turkish Building Seismic Design Code, TBSDC-18., (2018). Specification for structures to be built in disaster areas. Ministry of Public Works and Settlement Government of the Republic of Turkey.

Wallace, JW., (2007). Modeling issues for tall reinforced concrete core wall buildings. The Structural Design of Tall and Special Buildings, 16, 5, 615-632.

Yuksel SB., and Kalkan E. (2006). Behavior of tunnel form buildings under quasi-static cyclic lateral loading. Structural Engineering and Mechanics, 27, 1.

APPENDIX

– Appendix A– Nonlinear Modeling Input Parameters

The detailed parameters about structural components described in Section 2 are presented in Appendix A. These parameters include detailed material information such as concrete and reinforcement, moment-curvature (M-K) analysis, and shear F-D curve. All parameters are used to input structural software for NRHA. Nominal material strength is given in Table A.1

Table A.1: The nominal material strength parameters

Material	Strength	Value (MPa)
Concrete (C30)	Compressive Strength	30
Reinforcing Steel (S420)	Yield Strength	420
	Ultimate Strength	550

The unconfined and confined concrete parameters are determined by adopting the Mander model. (Mander et al, 1988). The idealization curve parameters are presented in Figure A.1. Table A.2 and Table A.3 depict the parameters of input structural software. DX point is selected a very large number to avoid convergence problem at large displacement in NRHA.

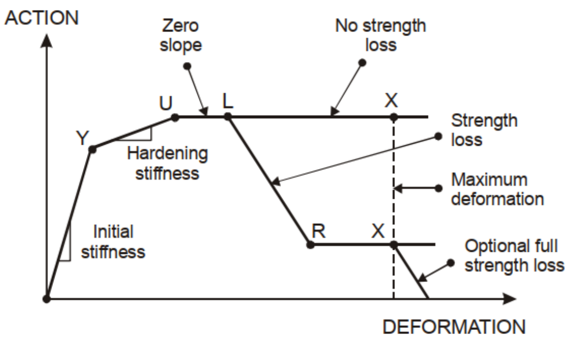

Figure A.1 Idealization model for Perform 3D (Perfom3D User Guide, 2006)

Table A.2 Constitutive model parameters

Tunnel Form Building		
Point	**Value**	
E_c	28000	MPa
f_{co}	30	MPa
e_{co}	0.002	
e_{cu}	0.005	
e_c	0.0048	
f_{cc}	33.33	MPa
e_{cc}	0.003	
e_{cr}	0.0134	
e_{cu}	0.03	

Table A.3. The points of the idealization curve

Point	Unconfined		Point	Confined	
FY,DY	0.6 f_{co}/E_c	0.6 f_{co}	**FY,DY**	0.6 f_{cc}/Ec	0.6 f_{cc}
FU,DU	0.9 e_{cc}	f_{co}	**FU,DU**	0.75 e_{cc}	f_{cc}
FL,DL	1.1 e_{cc}	f_{co}	**FL,DL**	1.2 e_{cc}	f_{cc}
DR,DR	e_{cu}	0.05 f_{co}	**DR,DR**	0.9 e_{cr}	0.63 f_{cc}

The reinforcement steel shown in Table A.1 is adopted a model proposed by Menegotto and Pinto, (1973). Two different steel constitutive models were produced since the code ASCE/SEI 41-17 constraints stain limits for reinforcement steel. These limits are 0.02 and 0.05 for compression and tension strains, respectively. The steel constative model shown in Figure A.2 was derived for EC8 and TBSDC-18 design codes, whereas a model shown in Figure A.3 was derived for the ASCE/SEI 41-17 design code.

Table A.4. Reinforcement steel parameters

Steel Grade	f_{sy}	e_{sy}	e_{sh}	e_{su}	f_{su}
S420	420	0.0021	0.008	0.1	550

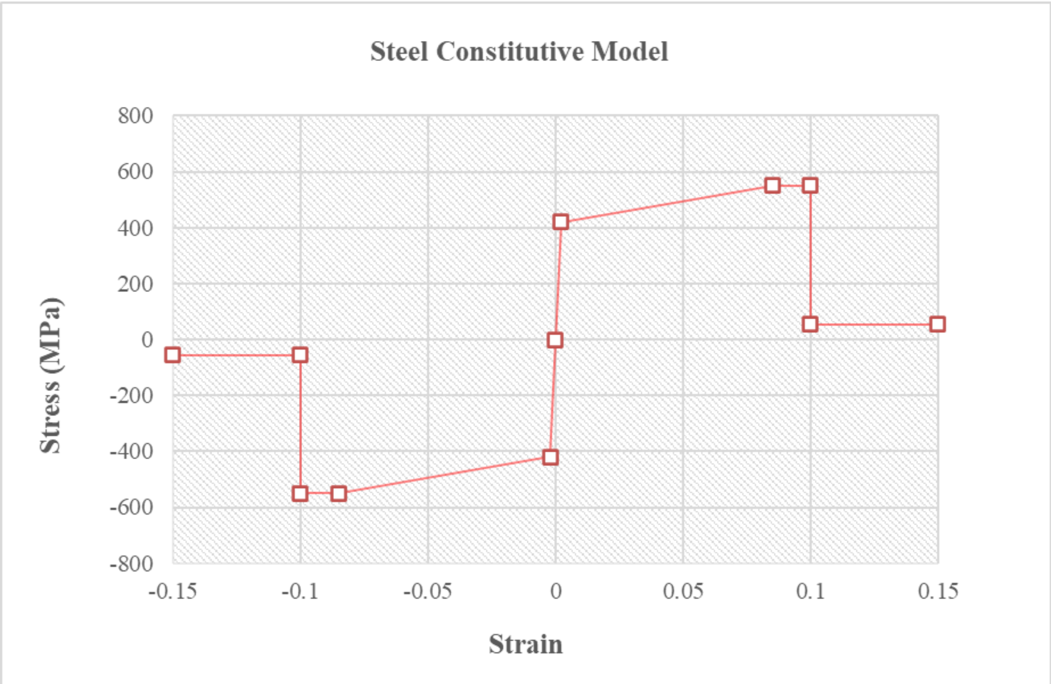

Figure A.2. Steel Constitutive Model for EC8 and TBSDC-18

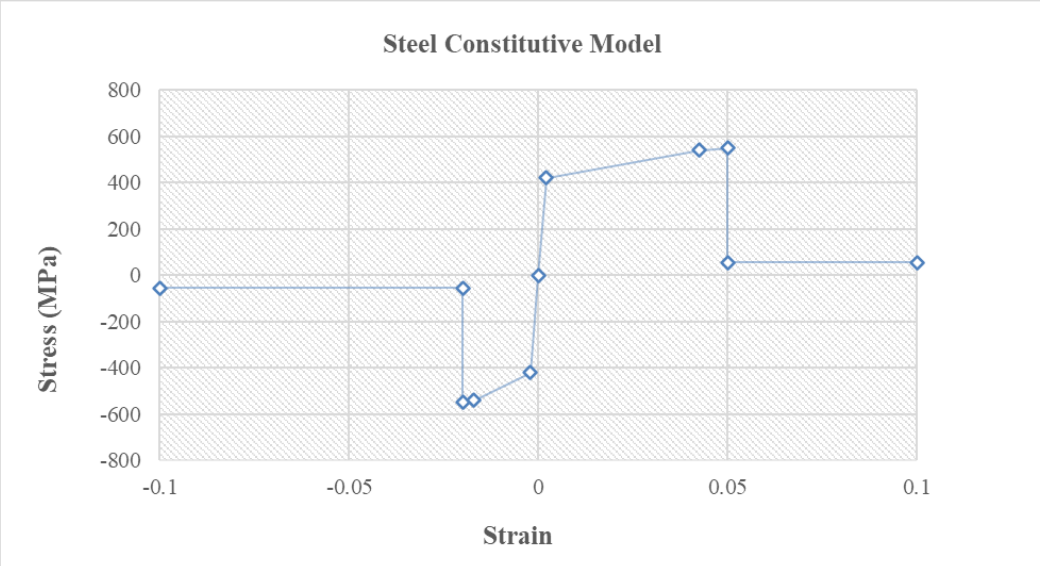

Figure A.3. Steel Constitutive Model for ASCE/SEI 41-17

The main concept of the shear stress-strain F-D backbone curve is described in section 2.2.1.1. ATC72-1 (2010), Wallace (2007), and Orakcal (2009) recommendations are utilized to be generated a shear F-D backbone curve (Figure A.4.). The shear behavior in model 1 considering limitations of the codes EC8 and TBSDC-18 is set linearly elastic, whereas the shear behavior in model 2 considering ASCE/SEI 41-17 is set to be as backbone curve illustrated in Figure A.4.

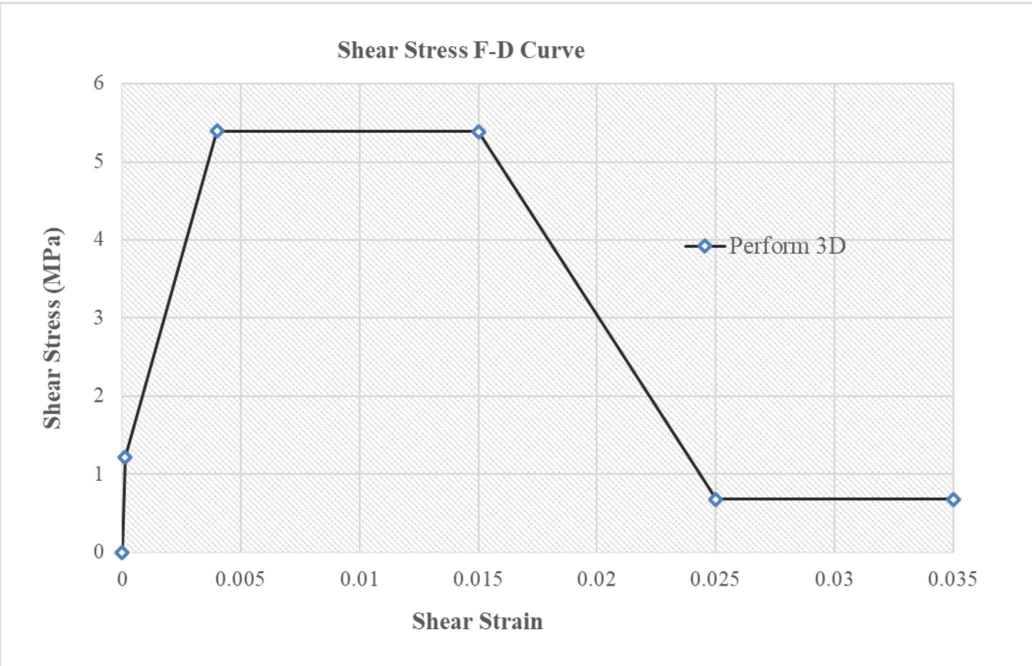

Figure A.4. Shear Stress-Strain Force-Deformation Curve

The M-K analysis is conducted by considering actual material properties and cross-section. The 6 -story tunnel form building has one beam section. The analysis results are shown in Figure A.5.

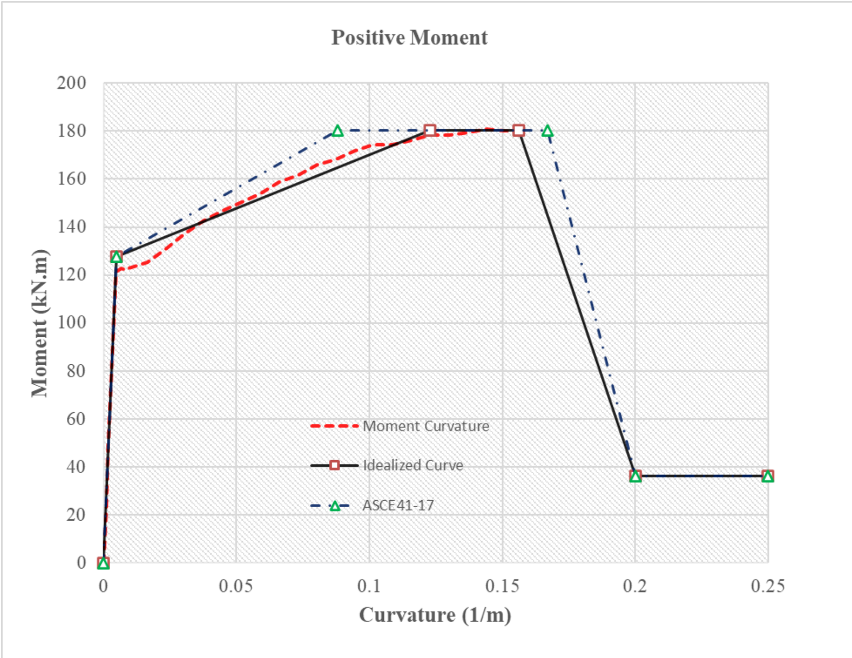

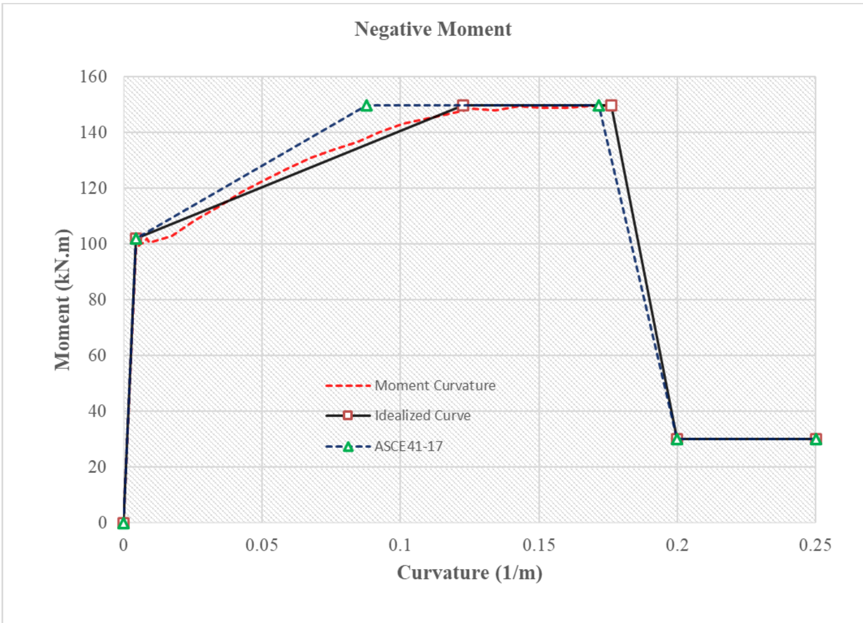

Figure A.5. Moment curvature analysis of beam at 6-floor

– Appendix B– Dynamic Analysis Results

Model Properties of Buildings:

Table B.1. Model properties of tunnel form building with 6 floor

Mode No.	Period (sec)	H1-Dir for Mode	H2-Dir for Mode	Cumulative H1-Dir	Cumulative H2-Dir
1	0.048	0.705	0	0.705	0
2	0.2137	0	0.71	0.705	0.71
3	0.096	0.20	0	0.905	0.71
4	0.05	0	0.21	0.905	0.92

Mode Shapes:

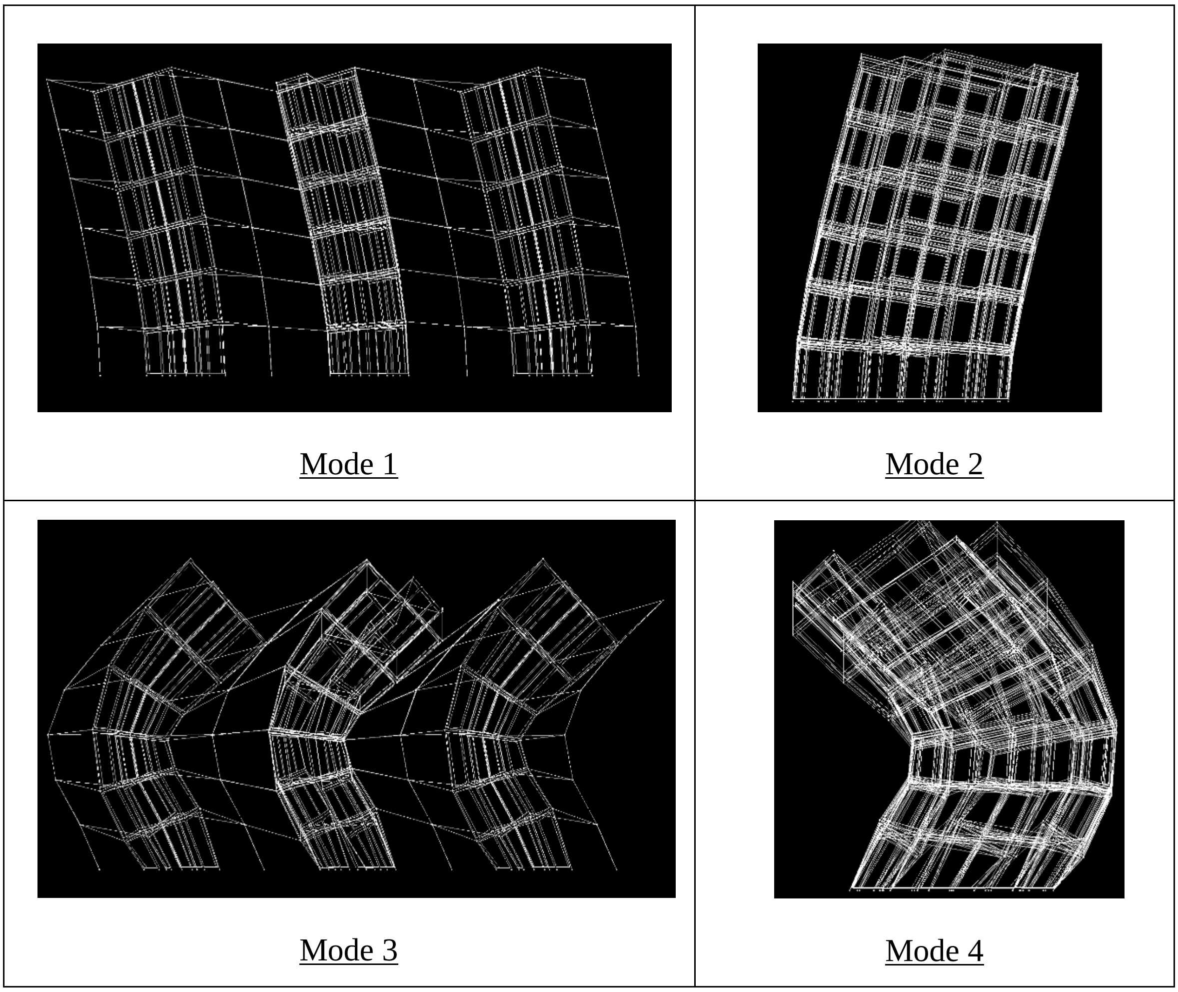

Figure B.1. Mode shapes of building with 6 floors.

Note that these mode shapes in Figure B.1 show only translational mode shapes considered in seismic hazard assessment.

Nonlinear Static Pushover Analysis:

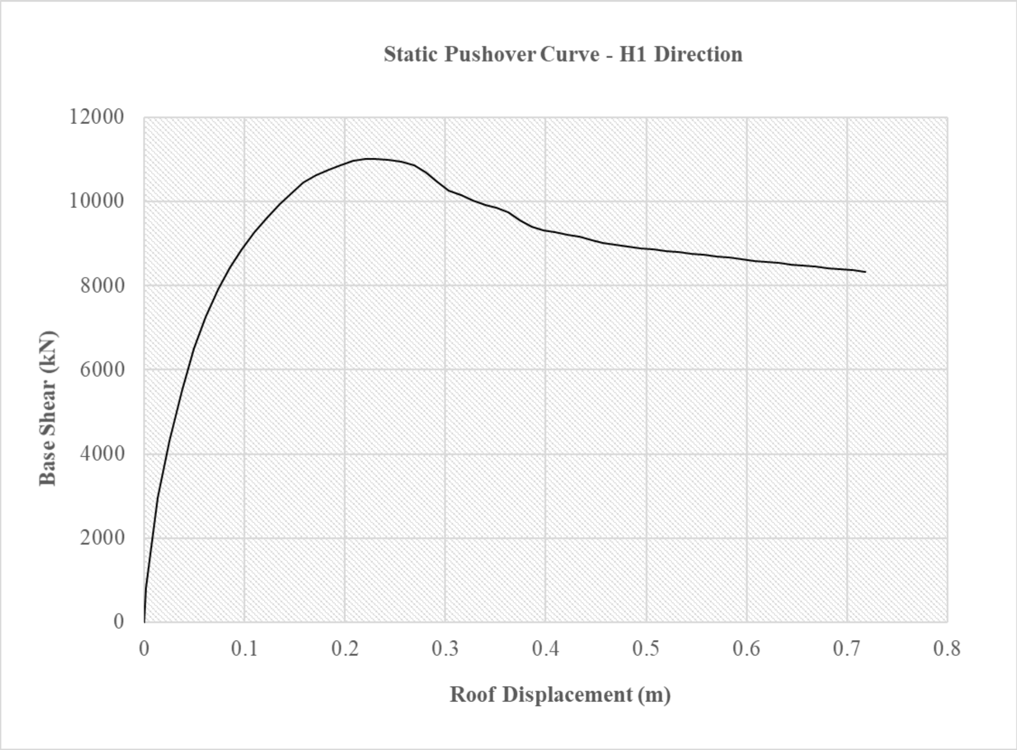

Figure B.2. Pushover Curve H1 (Long) Direction for 6-story

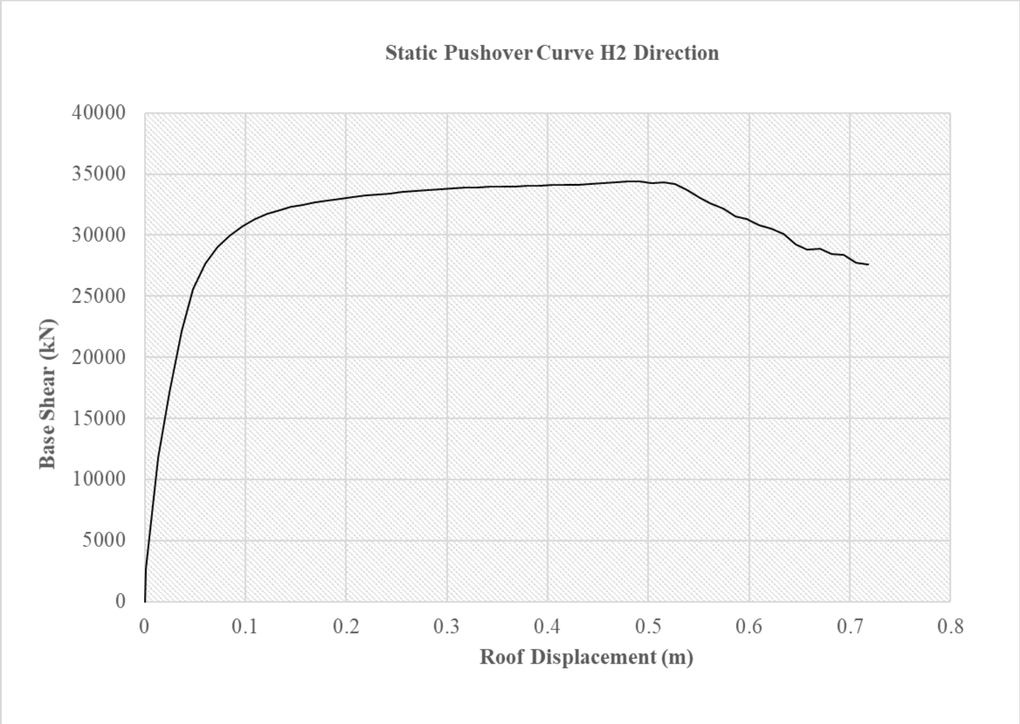

Figure B.3. Pushover Curve H2 (Short) Direction for 6-story

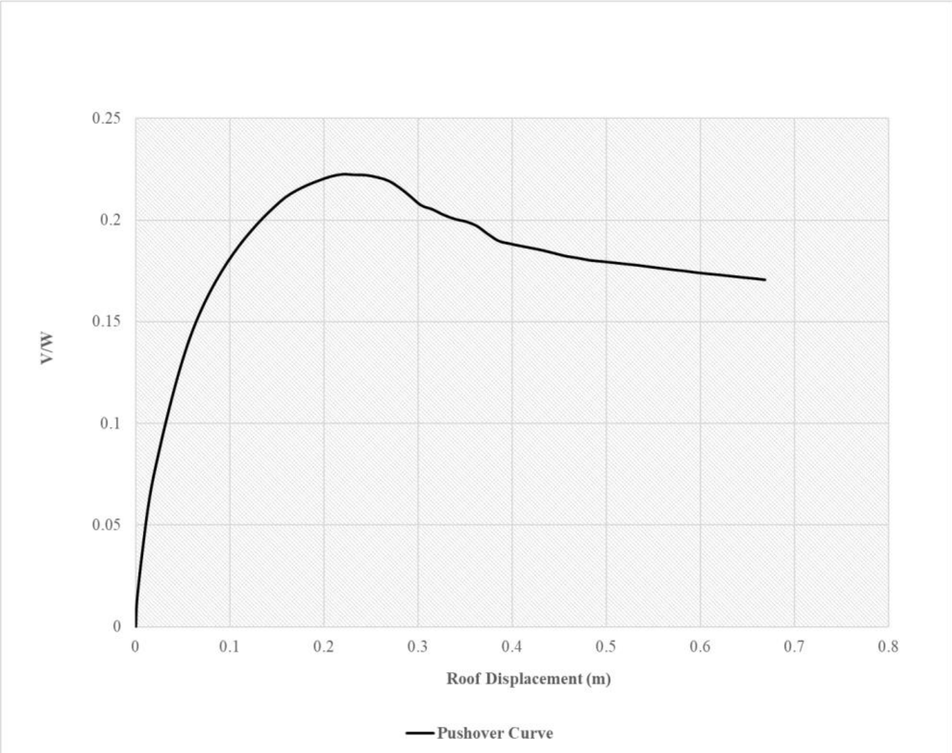

Figure B.4. Base shear (V), normalized by total building weight (W) versus Roof Displacement (H1 Direction)

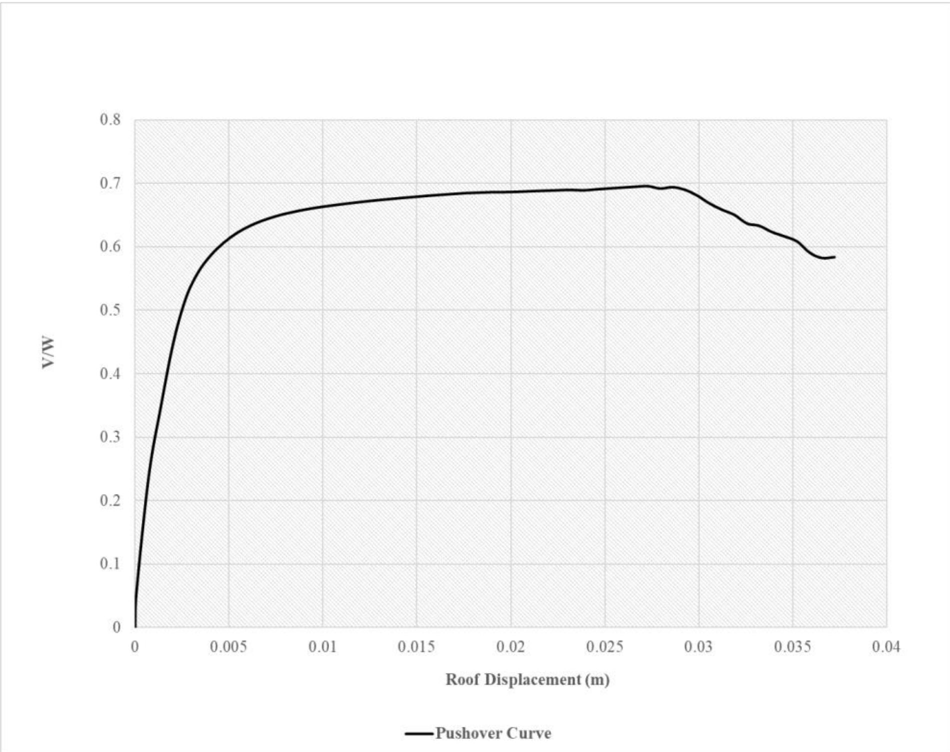

Figure B.5. Base shear (V), normalized by total building weight, (W) versus Roof Displacement (H2 Direction)

Nonlinear Static Push-Pull Analysis:

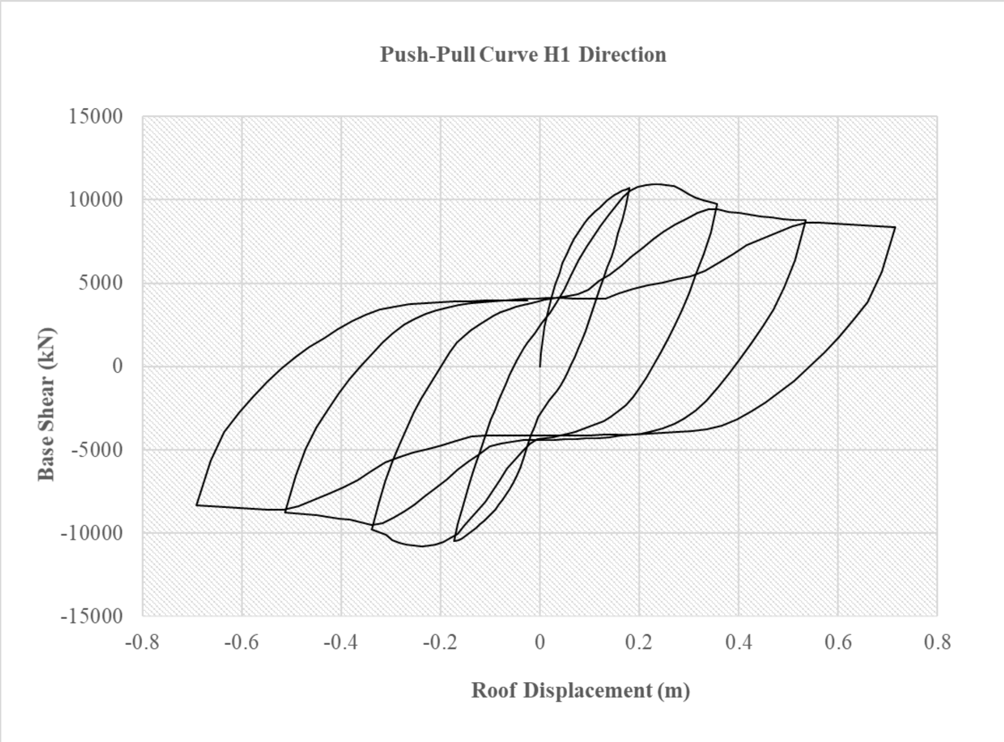

Figure B.6. Push-Pull Curve H1 Dir for 6-story

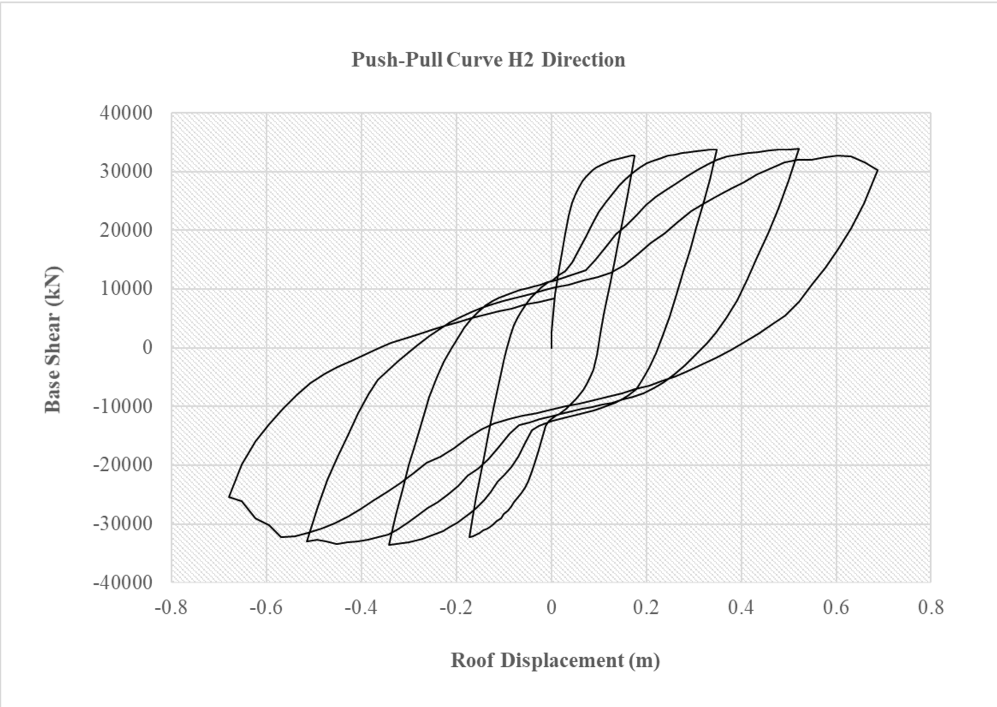

Figure B.7. Push-Pull Curve H2 Dir for 6-story

– Appendix C– Performance Assessment Response Limits

The Response Limits of TBSDC-18

The performance limits are described in Section 3.2.1. The structural limits are categorized into two groups based on their dimensions. The performance points are evaluated as two groups. Apart from dimensions, other parameters such as spacing, rebar diameter, and thickness are fixed. The performance points for the structural wall are shown in Table C.1.

Table C.1. Performance Points for Structural Wall for 6-floor building.

Wall Section Strain Limit States									
Wall ID / Limit State	**Reinforcement Limit States**			**Concrete Limit States**			**Final Limit States of Plastic Rotation**		
	LD	**CD**	**CP**	**LD**	**CD**	**CP**	**LD**	**CD**	**CP**
2X	0.0075	0.024	0.032	0.0025	0.00725	0.009668	0.0025	0.007251	0.0096682
2Y	0.0075	0.024	0.032	0.0025	0.00725	0.009668			
3	0.0075	0.024	0.032	0.0025	0.00725	0.009668			
4X	0.0075	0.024	0.032	0.0025	0.00725	0.009668			
5	0.0075	0.024	0.032	0.0025	0.00725	0.009668			
1	0.0075	0.024	0.032	0.0025	0.00754	0.010052	0.0025	0.007539	0.0100522
4Y	0.0075	0.024	0.032	0.0025	0.00754	0.010052			
6X	0.0075	0.024	0.032	0.0025	0.00754	0.010052			
6Y	0.0075	0.024	0.032	0.0025	0.00754	0.010052			
7	0.0075	0.024	0.032	0.0025	0.00754	0.010052			
8	0.0075	0.024	0.032	0.0025	0.00754	0.010052			

Beam elements performance points in this study are calculated as plastic rotation based on equations in TBSDC-18. Firstly, the strain limits are defined (Table C.2), then moment-curvature analyses are conducted, Finally, plastic rotations performance points are defined. (Table C.3)

Table C.2. Strain Limits for Beams for 6 story building.

Reinforcement Limit States		
LD	**CD**	**CP**
0.0075	0.024	0.032
Confined Concrete Limit States for Beam		
LD	**CD**	**CP**
0.0025	0.0135	0.018

Table C.3. Performance Points of Beams in 6 story buildings

Element Type	Section		Mp	Limit States of Plastic Rotation			Final Limit States of Plastic Rotation		
Name	**b (cm)**	**h (cm)**	$kN.m$	**LD**	**CD**	**CP**	**LD**	**CD**	**CP**
B25x60_P_5Q12_3Q14	25	60	180.3	0.00000	0.00931	0.01241	0	0.009236	0.012315
B25x60_N_3Q14_5Q12	25	60	149.9	0.00000	0.00924	0.01232			
Coupling Beam_P	25	60	180.3	0.00000	0.00849	0.01132	0	0.008423	0.011231
Coupling Beam_N	25	60	149.9	0.00000	0.00842	0.01123			

The Response Limits of EC8-3:

Structural walls are divided into two groups in terms of their dimensions. The performance points are derived from the expression described in Section 3.2.2 based on the province of EC8-3. The shear limits states are not determined since brittle behavior is considered as permitted.

Table C.4: Chord Rotation Limits for Walls in 6-floor building.

Wall Type	Chord Rotation Limits					
Name	**NC(ult)**	**SD**	**DL**	**NC(ult)**	**SD**	**DL**
2X	0.02879	0.02159	0.00219	0.02859	0.02145	0.00202
2Y	0.02910	0.02183	0.00202			
3	0.02878	0.02158	0.00202			
4X	0.02913	0.02185	0.00202			
5	0.02859	0.02145	0.00234			
1	0.01955	0.01466	0.00153	0.01955	0.01466	0.00153
4Y	0.02030	0.01522	0.00155			
6X	0.02286	0.01715	0.00165			
6Y	0.02031	0.01523	0.00163			
7	0.02034	0.01526	0.00155			
8	0.02270	0.01702	0.00163			

The Response Limits of ASCE/SEI 41-17:

The performance points tables given in ASCE/SEI 41-17 are taken into consideration in evaluating performance.

– Appendix D– Ground Motion Selection

The conditional Spectrum conditioned on average spectral acceleration:

The following figures (Figure D.1, Figure D.2, Figure D.3, and Figure D.4) show the conditional spectrum conditioned on average spectral acceleration for each IM level.

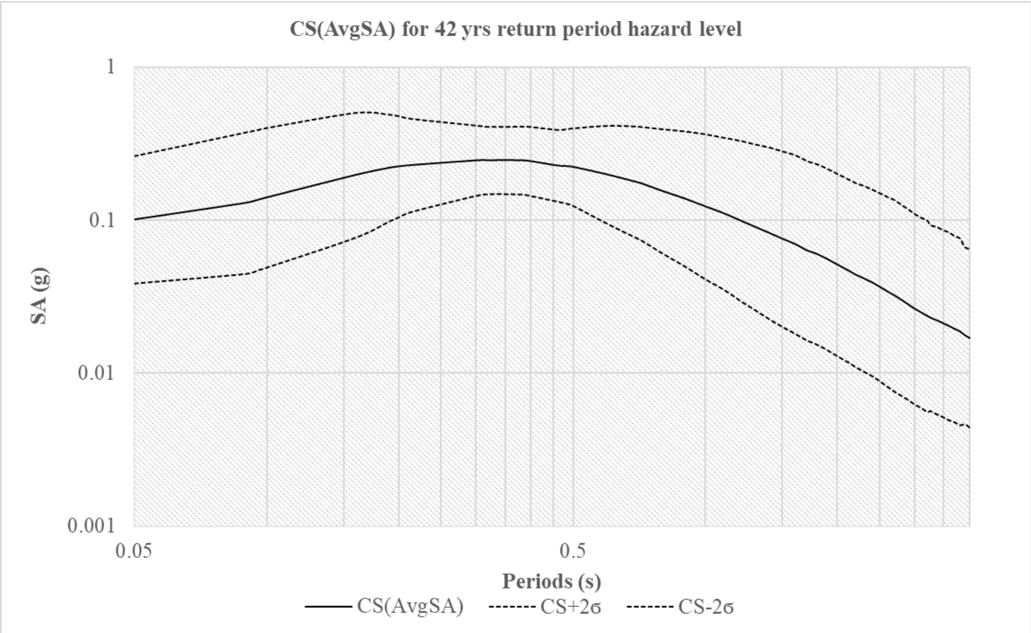

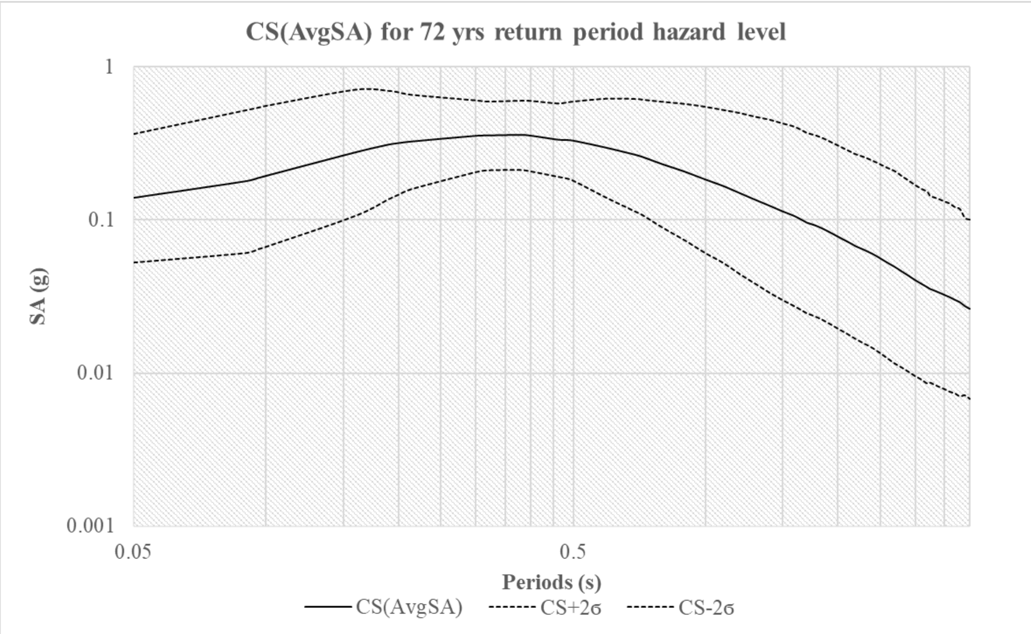

Figure D.1 Conditional Spectrum conditioned on AvgSA for 42 and 72 return periods hazard levels.

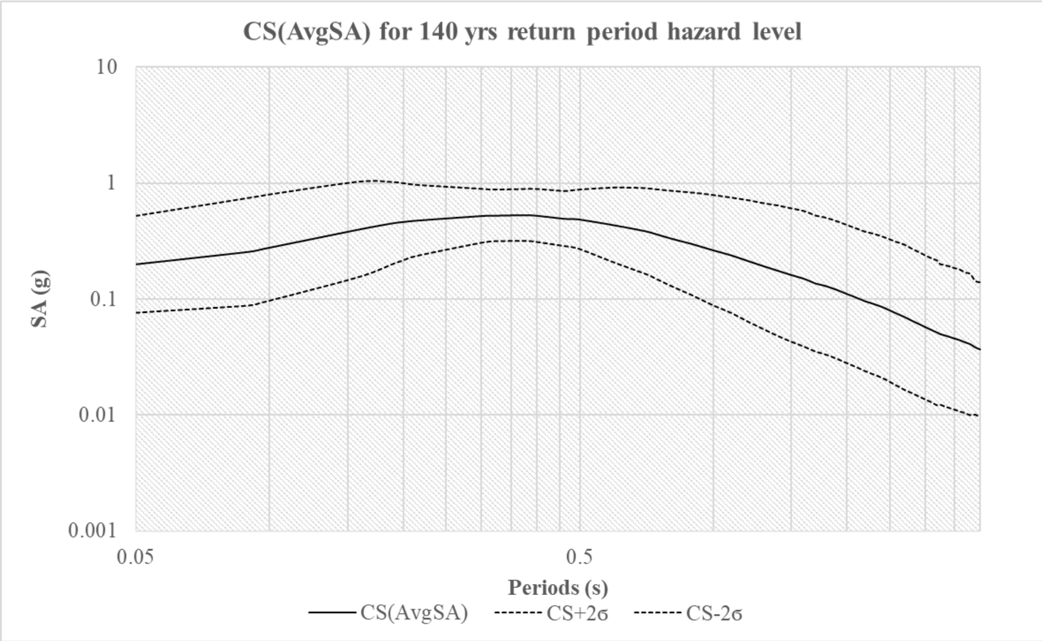

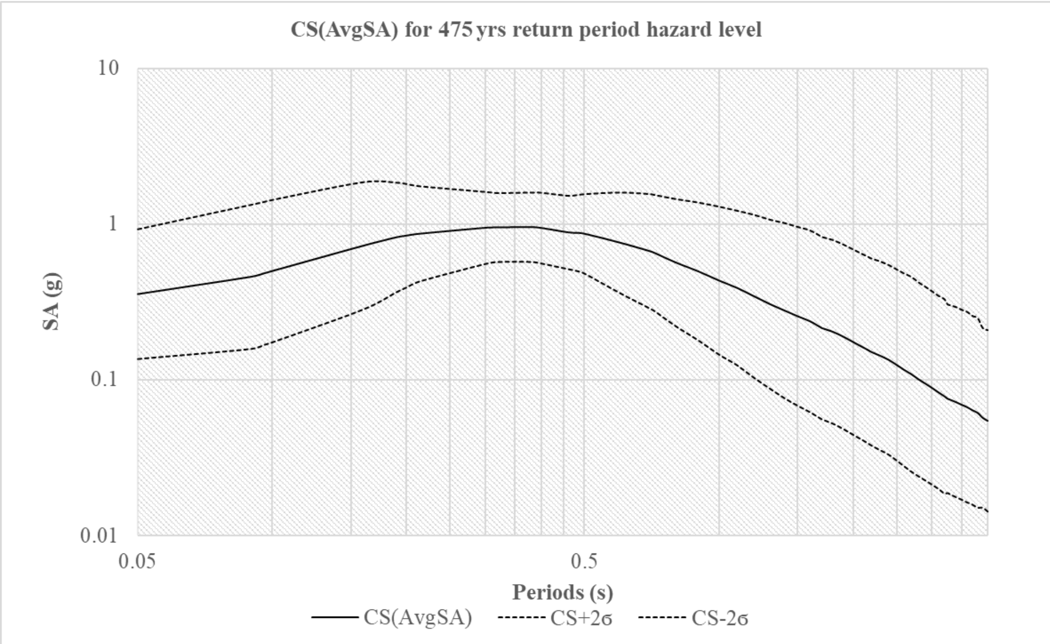

Figure D.2 Conditional Spectrum conditioned on AvgSA for 140 and 475 return periods hazard levels

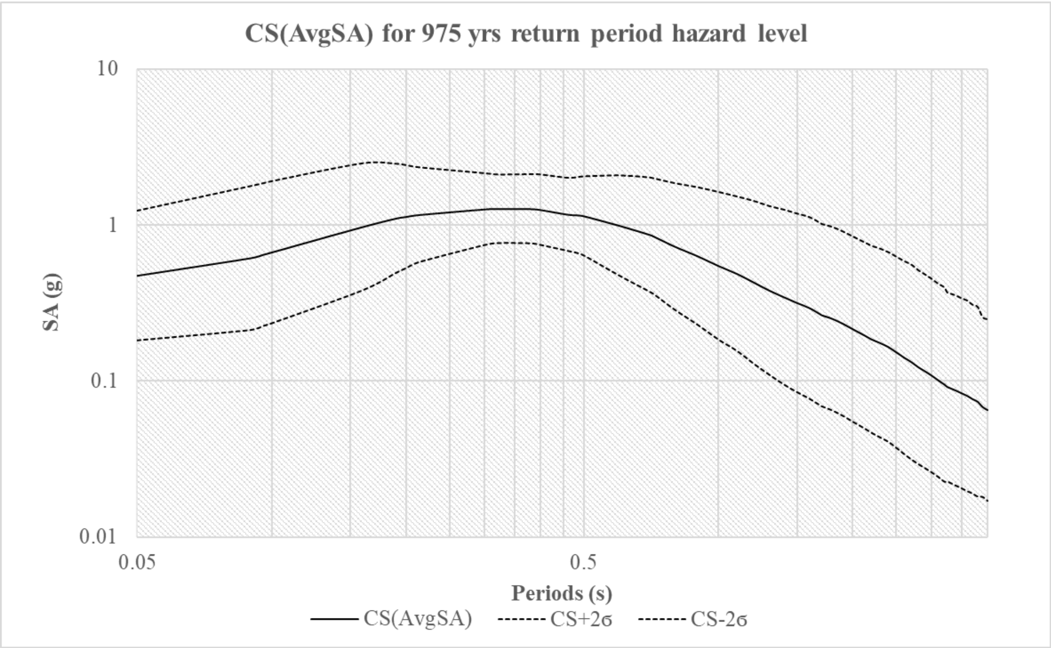

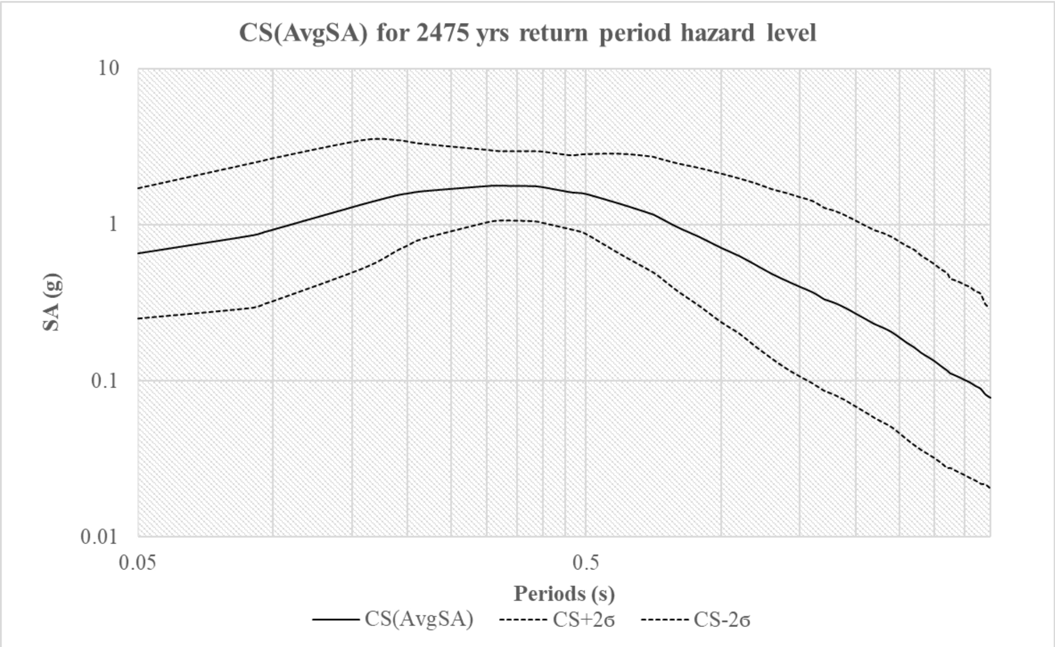

Figure D.3 Conditional Spectrum conditioned on AvgSA for 975 and 2475 return periods hazard levels

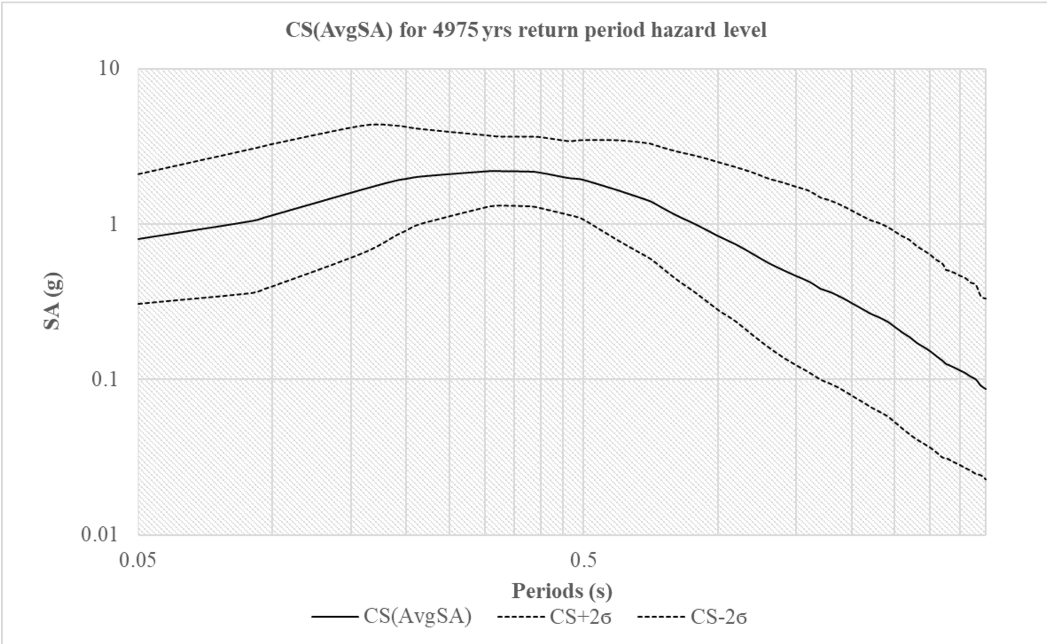

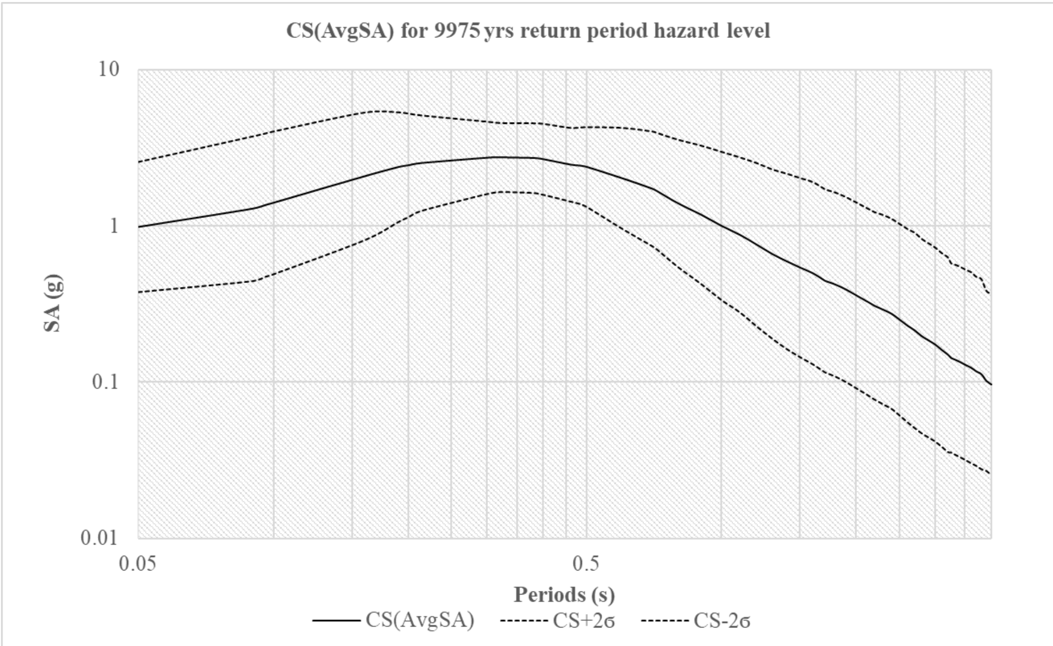

Figure D.4 Conditional Spectrum conditioned on AvgSA for 4975 and 9975 return periods hazard levels

The Selected Input Ground Motions:

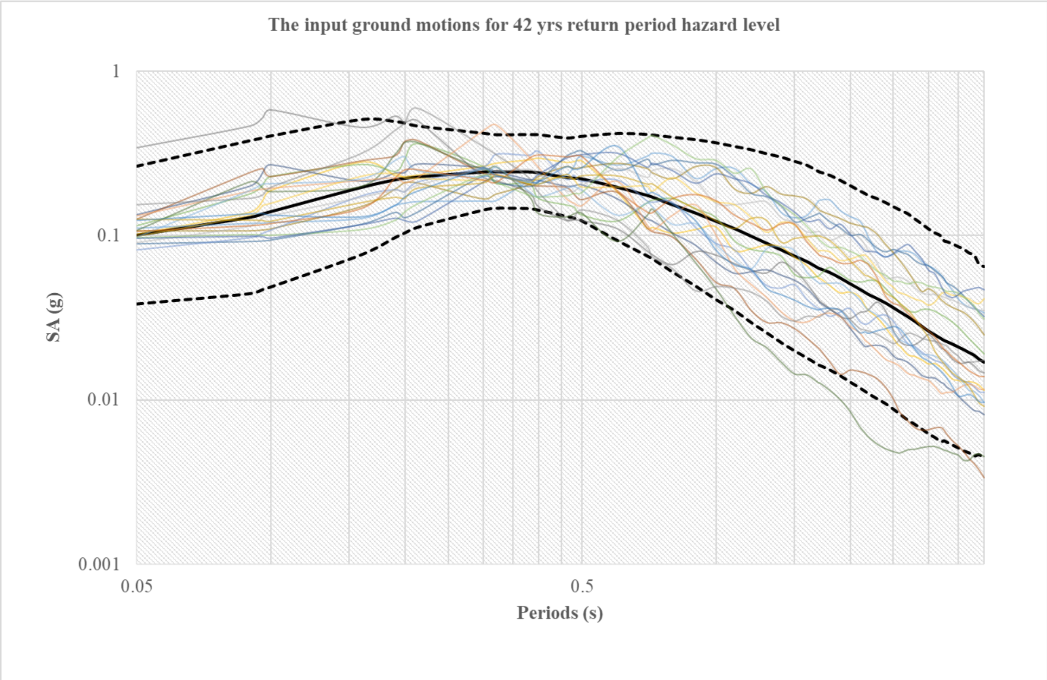

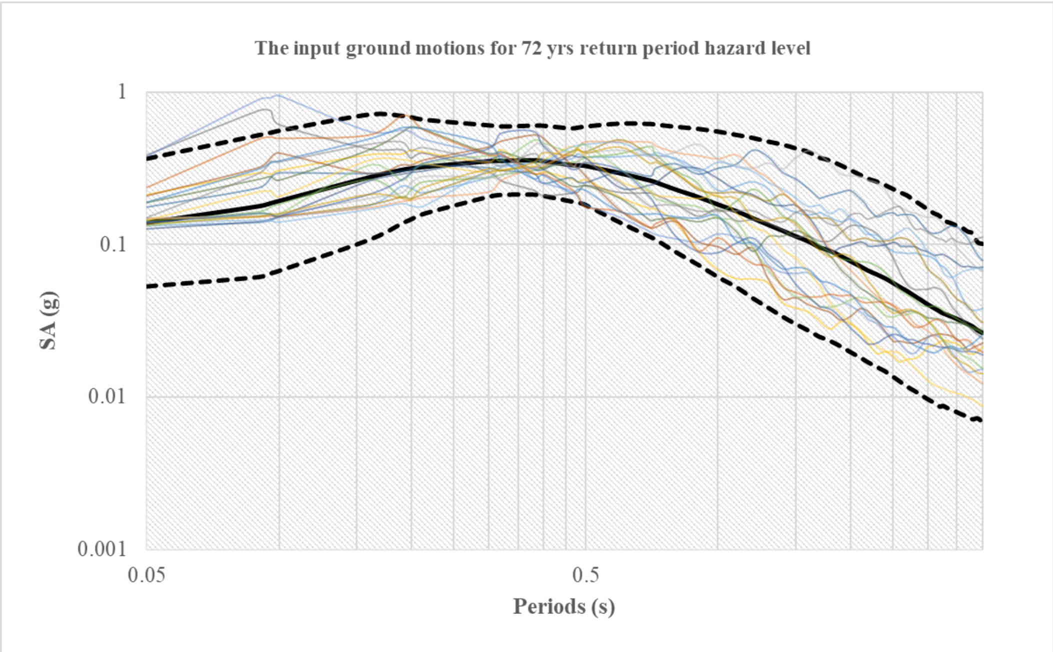

Figure D.5 The input ground motions for 42 and 72 years return periods hazard level

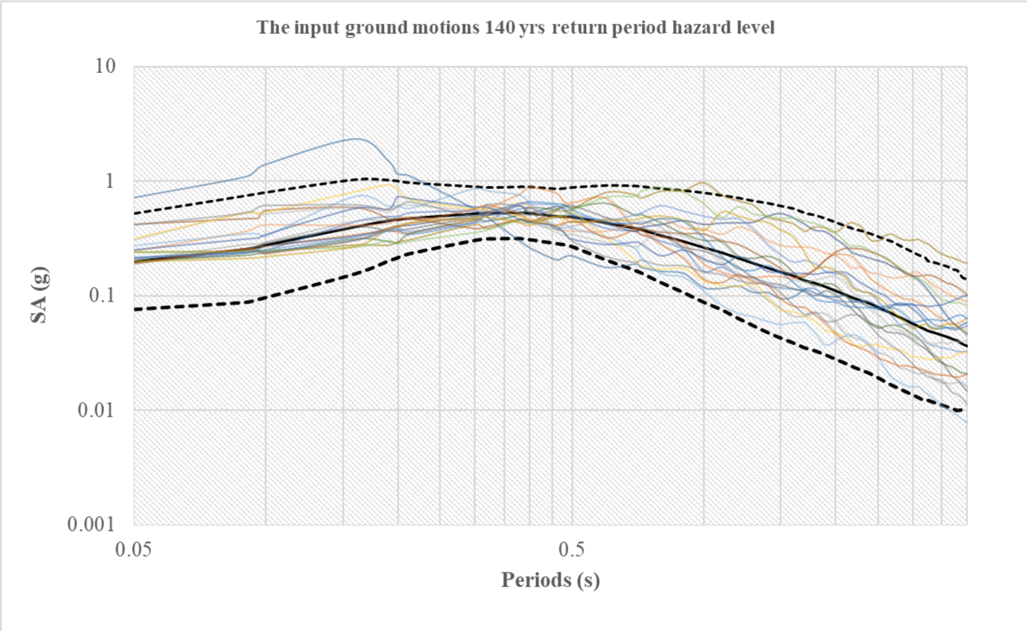

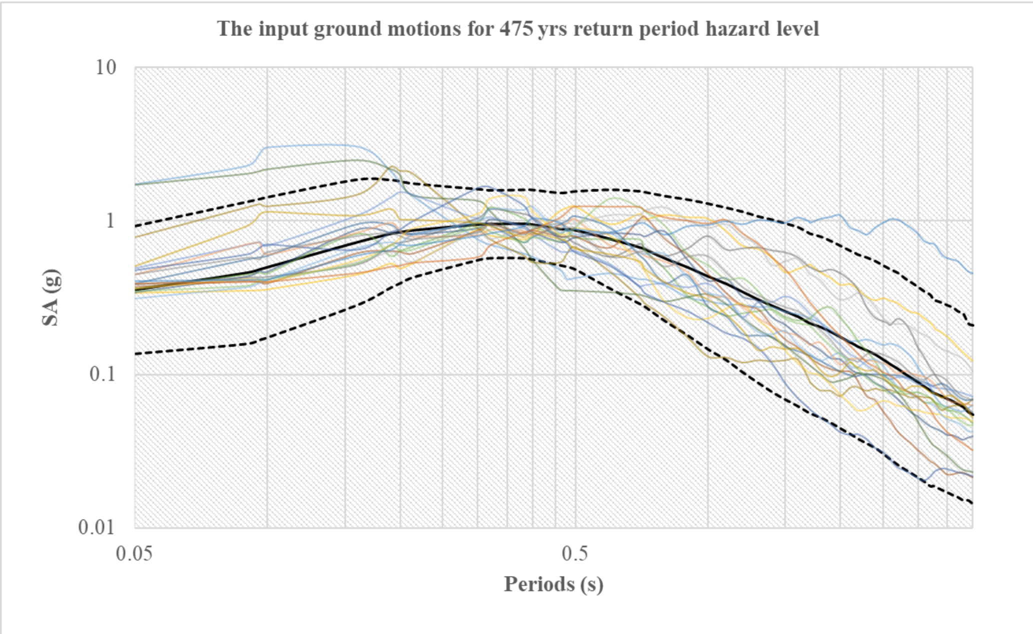

Figure D.6 The input ground motions for 140 and 475 years return periods hazard level

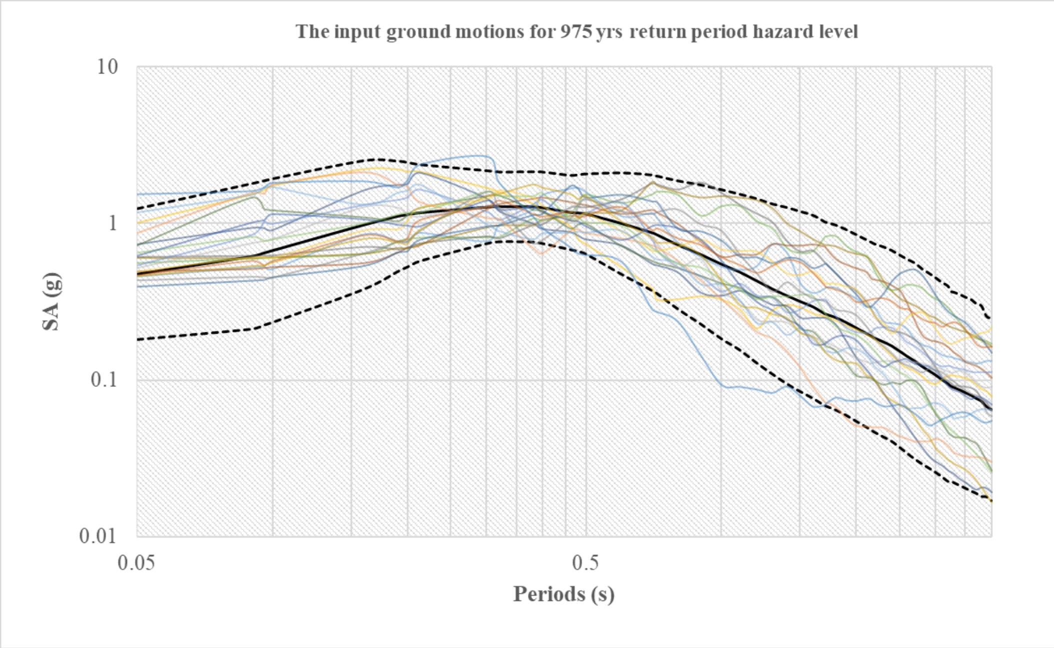

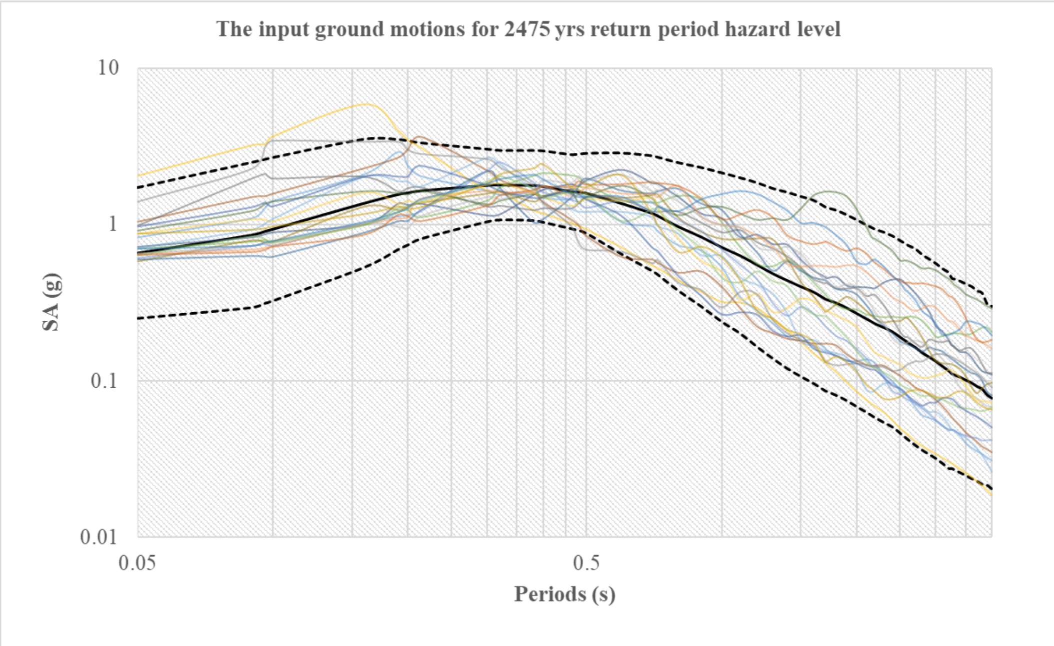

Figure D.7 The input ground motions for 975 and 2475 years return periods hazard level

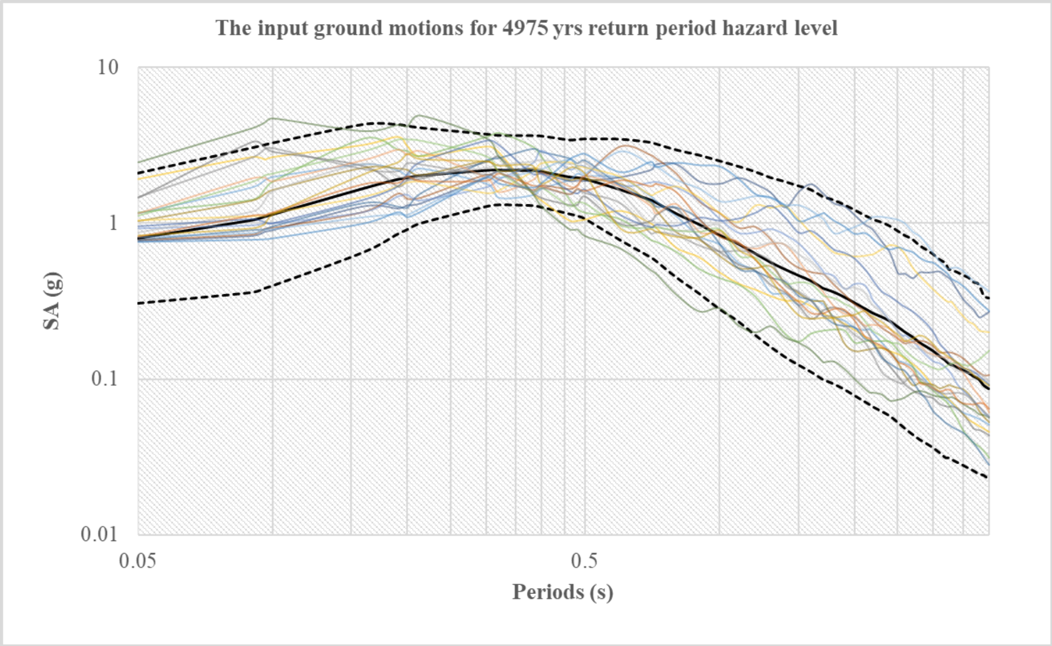

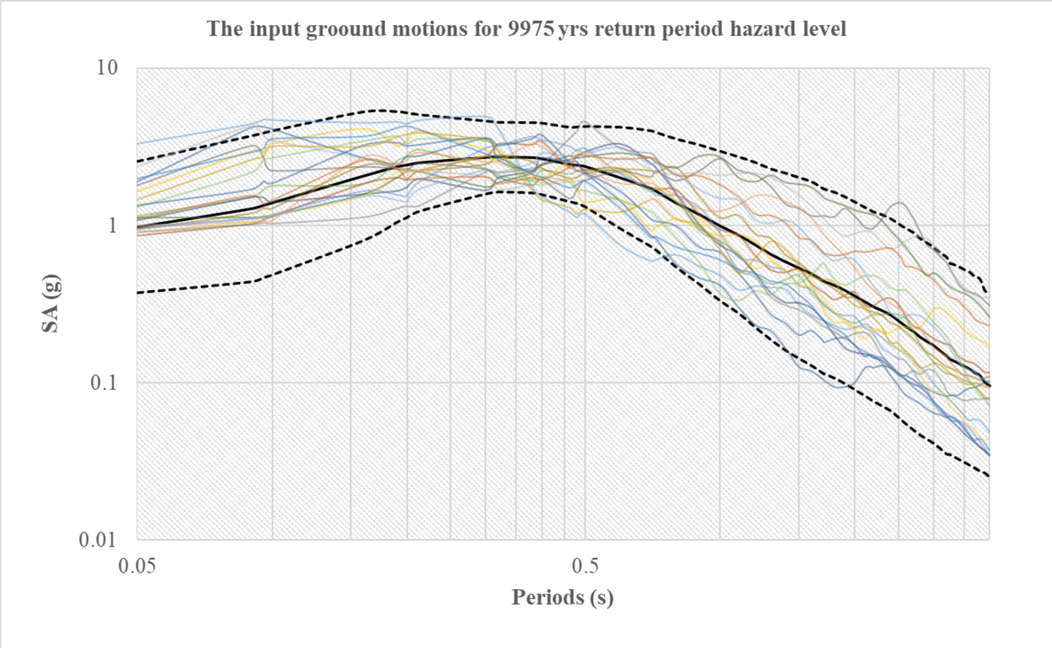

Figure D.8 The input ground motions for 4975 and 9975 years return periods hazard level

Table D.1 – The selected ground motion records and scaling factor (SF) for 42 return periods.

#	H1-Component	H2-Component	SF
1	RSN1205_CHICHI_CHY041-E.AT2	RSN1205_CHICHI_CHY041-N.AT2	0.41
2	RSN1376_CHICHI_KAU048-E.AT2	RSN1376_CHICHI_KAU048-N.AT2	1.59
3	RSN2907_CHICHI.04_TTN007E.AT2	RSN2907_CHICHI.04_TTN007N.AT2	5.23
4	RSN1770_HECTOR_BBL016.AT2	RSN1770_HECTOR_BBL106.AT2	0.97
5	RSN6959_DARFIELD_REHSN02E.AT2	RSN6959_DARFIELD_REHSS88E.AT2	0.30
6	RSN6242_TOTTORI.1_KGW004EW.AT2	RSN6242_TOTTORI.1_KGW004NS.AT2	1.41
7	RSN5970_SIERRA.MEX_BOR-90.AT2	RSN5970_SIERRA.MEX_BOR360.AT2	7.41
8	RSN1398_CHICHI_KAU087-N.AT2	RSN1398_CHICHI_KAU087-W.AT2	1.85
9	RSN4077_PARK2004_CHA090.AT2	RSN4077_PARK2004_CHA360.AT2	4.15
10	RSN3676_SMART1.45_45M06EW.AT2	RSN3676_SMART1.45_45M06NS.AT2	0.46
11	RSN2849_CHICHI.04_TCU038E.AT2	RSN2849_CHICHI.04_TCU038N.AT2	4.91
12	RSN1348_CHICHI_ILA064-N.AT2	RSN1348_CHICHI_ILA064-W.AT2	1.58
13	RSN5663_IWATE_MYG004EW.AT2	RSN5663_IWATE_MYG004NS.AT2	0.30
14	RSN1566_CHICHI_TTN010-E.AT2	RSN1566_CHICHI_TTN010-N.AT2	2.19
15	RSN8746_40204628_BKBDMHLE.AT2	RSN8746_40204628_BKBDMHLN.AT2	26.38
16	RSN266_VICT_CHI102.AT2	RSN266_VICT_CHI192.AT2	0.64
17	RSN1320_CHICHI_ILA016-N.AT2	RSN1320_CHICHI_ILA016-W.AT2	0.77
18	RSN5851_SIERRA.MEX_03154-90.AT2	RSN5851_SIERRA.MEX_03154360.AT2	2.56
19	RSN1266_CHICHI_HWA015-E.AT2	RSN1266_CHICHI_HWA015-N.AT2	0.74
20	RSN9280_14095628_CISMVHLE.AT2	RSN9280_14095628_CISMVHLN.AT2	52.98

Table D.2 The selected ground motion records and scaling factor (SF) for 72 return periods.

#	H1-Component	H2-Component	SF
1	RSN4078_PARK2004_COA090.AT2	RSN4078_PARK2004_COA360.AT2	2.63
2	RSN1628_STELIAS_059V2090.AT2	RSN1628_STELIAS_059V2180.AT2	0.73
3	RSN154_COYOTELK_SJB213.AT2	RSN154_COYOTELK_SJB303.AT2	2.21
4	RSN2857_CHICHI.04_TCU051E.AT2	RSN2857_CHICHI.04_TCU051N.AT2	7.65
5	RSN1455_CHICHI_TAP094-E.AT2	RSN1455_CHICHI_TAP094-N.AT2	1.18
6	RSN580_SMART1.45_45O06EW.AT2	RSN580_SMART1.45_45O06NS.AT2	0.66
7	RSN11100_40187964_NCCTAHNE.AT2	RSN11100_40187964_NCCTAHNN.AT2	87.57
8	RSN6980_DARFIELD_WAKCN80E.AT2	RSN6980_DARFIELD_WAKCS10E.AT2	1.03
9	RSN4077_PARK2004_CHA090.AT2	RSN4077_PARK2004_CHA360.AT2	6.28
10	RSN2859_CHICHI.04_TCU053E.AT2	RSN2859_CHICHI.04_TCU053N.AT2	9.77
11	RSN6138_TOTTORI.1_EHM001EW.AT2	RSN6138_TOTTORI.1_EHM001NS.AT2	3.29
12	RSN1563_CHICHI_TTN007-E.AT2	RSN1563_CHICHI_TTN007-N.AT2	3.92
13	RSN18085_14519780_CIFURHNE.AT2	RSN18085_14519780_CIFURHNN.AT2	74.64
14	RSN1562_CHICHI_TTN006-E.AT2	RSN1562_CHICHI_TTN006-N.AT2	3.44
15	RSN166_IMPVALL.H_H-CC4045.AT2	RSN166_IMPVALL.H_H-CC4135.AT2	1.60
16	RSN1299_CHICHI_HWA054-N.AT2	RSN1299_CHICHI_HWA054-W.AT2	4.01
17	RSN546_CHALFANT.B_B-SHE009.AT2	RSN546_CHALFANT.B_B-SHE099.AT2	9.67
18	RSN1274_CHICHI_HWA025-E.AT2	RSN1274_CHICHI_HWA025-N.AT2	2.08
19	RSN470_MORGAN_SJB213.AT2	RSN470_MORGAN_SJB303.AT2	3.49
20	RSN8746_40204628_BKBDMHLE.AT2	RSN8746_40204628_BKBDMHLN.AT2	39.92

Table D.3 The selected ground motion records and scaling factor (SF) for 140 return periods

#	H1-Component	H2-Component	SF
1	RSN1809_HECTOR_LCF090.AT2	RSN1809_HECTOR_LCF360.AT2	5.71
2	RSN913_BIGBEAR_TEM090.AT2	RSN913_BIGBEAR_TEM180.AT2	6.79
3	RSN584_SMART1.45_45O12EW.AT2	RSN584_SMART1.45_45O12NS.AT2	1.23
4	RSN6246_TOTTORI.1_KGW008EW.AT2	RSN6246_TOTTORI.1_KGW008NS.AT2	11.05
5	RSN11429_10275733_CIPDEHHE.AT2	RSN11429_10275733_CIPDEHHN.AT2	359.47
6	RSN1320_CHICHI_ILA016-N.AT2	RSN1320_CHICHI_ILA016-W.AT2	1.74
7	RSN15_KERN_TAF021.AT2	RSN15_KERN_TAF111.AT2	1.56
8	RSN6903_DARFIELD_FJDSN83E.AT2	RSN6903_DARFIELD_FJDSS07E.AT2	7.39
9	RSN2721_CHICHI.04_CHY057E.AT2	RSN2721_CHICHI.04_CHY057N.AT2	12.85
10	RSN4346_UBMARCHE.P_A-BEV000.AT2	RSN4346_UBMARCHE.P_A-BEV270.AT2	3.14
11	RSN1376_CHICHI_KAU048-E.AT2	RSN1376_CHICHI_KAU048-N.AT2	3.58
12	RSN1563_CHICHI_TTN007-E.AT2	RSN1563_CHICHI_TTN007-N.AT2	5.82
13	RSN1566_CHICHI_TTN010-E.AT2	RSN1566_CHICHI_TTN010-N.AT2	4.92
14	RSN18397_21401069_NPMPBHHE.AT2	RSN18397_21401069_NPMPBHHN.AT2	34.10
15	RSN1398_CHICHI_KAU087-N.AT2	RSN1398_CHICHI_KAU087-W.AT2	4.16
16	RSN1327_CHICHI_ILA035-E.AT2	RSN1327_CHICHI_ILA035-N.AT2	2.34
17	RSN1425_CHICHI_TAP032-E.AT2	RSN1425_CHICHI_TAP032-N.AT2	1.26
18	RSN1568_CHICHI_TTN013-E.AT2	RSN1568_CHICHI_TTN013-N.AT2	7.62
19	RSN8487_PARK2004_NPMPBHNE.AT2	RSN8487_PARK2004_NPMPBHNN.AT2	5.31
20	RSN2813_CHICHI.04_KAU020E.AT2	RSN2813_CHICHI.04_KAU020N.AT2	5.39

Table D.4 The selected ground motion records and scaling factor (SF) for 475 return periods

#	H1-Component	H2-Component	SF
1	RSN1764_HECTOR_TRF090.AT2	RSN1764_HECTOR_TRF360.AT2	12.70
2	RSN6246_TOTTORI.1_KGW008EW.AT2	RSN6246_TOTTORI.1_KGW008NS.AT2	19.34
3	RSN1566_CHICHI_TTN010-E.AT2	RSN1566_CHICHI_TTN010-N.AT2	8.62
4	RSN166_IMPVALL.H_H-CC4045.AT2	RSN166_IMPVALL.H_H-CC4135.AT2	4.16
5	RSN1865_YOUNTVL_1438A270.AT2	RSN1865_YOUNTVL_1438B180.AT2	59.70
6	RSN11088_40187964_BKBDMHLE.AT2	RSN11088_40187964_BKBDMHLN.AT2	827.13
7	RSN13_KERN_PAS180.AT2	RSN13_KERN_PAS270.AT2	5.41
8	RSN8622_40204628_N1780HNE.AT2	RSN8622_40204628_N1780HNN.AT2	12.05
9	RSN1335_CHICHI_ILA046-E.AT2	RSN1335_CHICHI_ILA046-N.AT2	5.45
10	RSN1266_CHICHI_HWA015-E.AT2	RSN1266_CHICHI_HWA015-N.AT2	2.93
11	RSN1398_CHICHI_KAU087-N.AT2	RSN1398_CHICHI_KAU087-W.AT2	7.28
12	RSN1326_CHICHI_ILA032-E.AT2	RSN1326_CHICHI_ILA032-N.AT2	4.36
13	RSN1154_KOCAELI_BSI090.AT2	RSN1154_KOCAELI_BSI180.AT2	4.78
14	RSN15_KERN_TAF021.AT2	RSN15_KERN_TAF111.AT2	2.73
15	RSN1320_CHICHI_ILA016-N.AT2	RSN1320_CHICHI_ILA016-W.AT2	3.04
16	RSN1316_CHICHI_ILA012-N.AT2	RSN1316_CHICHI_ILA012-W.AT2	3.21
17	RSN1848_YOUNTVL_DFS090.AT2	RSN1848_YOUNTVL_DFS360.AT2	29.63
18	RSN1564_CHICHI_TTN008-E.AT2	RSN1564_CHICHI_TTN008-N.AT2	7.32
19	RSN8487_PARK2004_NPMPBHNE.AT2	RSN8487_PARK2004_NPMPBHNN.AT2	9.30
20	RSN1568_CHICHI_TTN013-E.AT2	RSN1568_CHICHI_TTN013-N.AT2	13.33

Table D.5 The selected ground motion records and scaling factor (SF) for 975 return periods

#	H1-Component	H2-Component	SF
1	RSN6051_SIERRA.MEX_TOR-90.AT2	RSN6051_SIERRA.MEX_TOR360.AT2	41.85
2	RSN1320_CHICHI_ILA016-N.AT2	RSN1320_CHICHI_ILA016-W.AT2	3.98
3	RSN8746_40204628_BKBDMHLE.AT2	RSN8746_40204628_BKBDMHLN.AT2	135.96
4	RSN2038_GILROY2_0440090.AT2	RSN2038_GILROY2_0440360.AT2	115.37
5	RSN5864_SIERRA.MEX_FNK090.AT2	RSN5864_SIERRA.MEX_FNK360.AT2	9.77
6	RSN8679_40204628_NCCRHHNE.AT2	RSN8679_40204628_NCCRHHNN.AT2	42.64
7	RSN6036_SIERRA.MEX_RXH-90.AT2	RSN6036_SIERRA.MEX_RXH360.AT2	8.69
8	RSN4077_PARK2004_CHA090.AT2	RSN4077_PARK2004_CHA360.AT2	21.38
9	RSN1460_CHICHI_TAP103-E.AT2	RSN1460_CHICHI_TAP103-N.AT2	2.84
10	RSN18397_21401069_NPMPBHHE.AT2	RSN18397_21401069_NPMPBHHN.AT2	78.22
11	RSN1431_CHICHI_TAP043-E.AT2	RSN1431_CHICHI_TAP043-N.AT2	5.08
12	RSN1563_CHICHI_TTN007-E.AT2	RSN1563_CHICHI_TTN007-N.AT2	13.35
13	RSN1628_STELIAS_059V2090.AT2	RSN1628_STELIAS_059V2180.AT2	2.50
14	RSN8827_14383980_CIPDUHNE.AT2	RSN8827_14383980_CIPDUHNN.AT2	13.60
15	RSN3754_LANDERS_INJ090.AT2	RSN3754_LANDERS_INJ180.AT2	2.21
16	RSN645_WHITTIER.A_A-OR2010.AT2	RSN645_WHITTIER.A_A-OR2280.AT2	3.15
17	RSN1327_CHICHI_ILA035-E.AT2	RSN1327_CHICHI_ILA035-N.AT2	5.38
18	RSN1565_CHICHI_TTN009-E.AT2	RSN1565_CHICHI_TTN009-N.AT2	9.20
19	RSN6923_DARFIELD_KPOCN15E.AT2	RSN6923_DARFIELD_KPOCS75E.AT2	2.18
20	RSN1859_YOUNTVL_1445A090.AT2	RSN1859_YOUNTVL_1445B360.AT2	57.79

Table D.6 The selected ground motion records and scaling factor (SF) for 2475 return periods

#	H1-Component	H2-Component	SF
1	RSN1848_YOUNTVL_DFS090.AT2	RSN1848_YOUNTVL_DFS360.AT2	52.63
2	RSN8673_40204628_NCDOBHNE.AT2	RSN8673_40204628_NCDOBHNN.AT2	74.84
3	RSN18397_21401069_NPMPBHHE.AT2	RSN18397_21401069_NPMPBHHN.AT2	106.06
4	RSN3676_SMART1.45_45M06EW.AT2	RSN3676_SMART1.45_45M06NS.AT2	3.21
5	RSN9462_9086578_CIFONHLE.AT2	RSN9462_9086578_CIFONHLN.AT2	1000.20
6	RSN1264_CHICHI_HWA013-E.AT2	RSN1264_CHICHI_HWA013-N.AT2	3.66
7	RSN1320_CHICHI_ILA016-N.AT2	RSN1320_CHICHI_ILA016-W.AT2	5.40
8	RSN1794_HECTOR_JOS090.AT2	RSN1794_HECTOR_JOS360.AT2	3.84
9	RSN1564_CHICHI_TTN008-E.AT2	RSN1564_CHICHI_TTN008-N.AT2	13.00
10	RSN1361_CHICHI_KAU020-E.AT2	RSN1361_CHICHI_KAU020-N.AT2	5.16
11	RSN1300_CHICHI_HWA055-N.AT2	RSN1300_CHICHI_HWA055-W.AT2	4.96
12	RSN19894_40187964_NSPHNE.AT2	RSN19894_40187964_NSPHNN.AT2	86.69
13	RSN1566_CHICHI_TTN010-E.AT2	RSN1566_CHICHI_TTN010-N.AT2	15.32
14	RSN3757_LANDERS_NPF090.AT2	RSN3757_LANDERS_NPF180.AT2	4.71
15	RSN468_MORGAN_LBN090.AT2	RSN468_MORGAN_LBN180.AT2	10.32
16	RSN1326_CHICHI_ILA032-E.AT2	RSN1326_CHICHI_ILA032-N.AT2	7.75
17	RSN5864_SIERRA.MEX_FNK090.AT2	RSN5864_SIERRA.MEX_FNK360.AT2	13.25
18	RSN13_KERN_PAS180.AT2	RSN13_KERN_PAS270.AT2	9.61
19	RSN1588_CHICHI_TTN044-N.AT2	RSN1588_CHICHI_TTN044-W.AT2	8.34
20	RSN2859_CHICHI.04_TCU053E.AT2	RSN2859_CHICHI.04_TCU053N.AT2	45.14

Table D.7 The selected ground motion records and scaling factor (SF) for 4975 return periods

#	H1-Component	H2-Component	SF
1	RSN1460_CHICHI_TAP103-E.AT2	RSN1460_CHICHI_TAP103-N.AT2	4.76
2	RSN1300_CHICHI_HWA055-N.AT2	RSN1300_CHICHI_HWA055-W.AT2	6.14
3	RSN913_BIGBEAR_TEM090.AT2	RSN913_BIGBEAR_TEM180.AT2	26.13
4	RSN8679_40204628_NCCRHHNE.AT2	RSN8679_40204628_NCCRHHNN.AT2	71.53
5	RSN1266_CHICHI_HWA015-E.AT2	RSN1266_CHICHI_HWA015-N.AT2	6.43
6	RSN1566_CHICHI_TTN010-E.AT2	RSN1566_CHICHI_TTN010-N.AT2	18.95
7	RSN8887_14383980_13889090.AT2	RSN8887_14383980_13889360.AT2	20.18
8	RSN721_SUPER.B_B-ICC000.AT2	RSN721_SUPER.B_B-ICC090.AT2	3.33
9	RSN1320_CHICHI_ILA016-N.AT2	RSN1320_CHICHI_ILA016-W.AT2	6.68
10	RSN4094_PARK2004_HSP090.AT2	RSN4094_PARK2004_HSP360.AT2	40.18
11	RSN2791_CHICHI.04_HWA045N.AT2	RSN2791_CHICHI.04_HWA045W.AT2	122.57
12	RSN1327_CHICHI_ILA035-E.AT2	RSN1327_CHICHI_ILA035-N.AT2	9.02
13	RSN1564_CHICHI_TTN008-E.AT2	RSN1564_CHICHI_TTN008-N.AT2	16.09
14	RSN1574_CHICHI_TTN022-E.AT2	RSN1574_CHICHI_TTN022-N.AT2	9.20
15	RSN1326_CHICHI_ILA032-E.AT2	RSN1326_CHICHI_ILA032-N.AT2	9.59
16	RSN1289_CHICHI_HWA041-E.AT2	RSN1289_CHICHI_HWA041-N.AT2	7.50
17	RSN11094_40187964_NCDOBHNE.AT2	RSN11094_40187964_NCDOBHNN.AT2	830.38
18	RSN1454_CHICHI_TAP090-E.AT2	RSN1454_CHICHI_TAP090-N.AT2	5.42
19	RSN8663_40204628_N1844HNE.AT2	RSN8663_40204628_N1844HNN.AT2	99.01
20	RSN6903_DARFIELD_FJDSN83E.AT2	RSN6903_DARFIELD_FJDSS07E.AT2	39.92

Table D.8 The selected ground motion records and scaling factor (SF) for 9975return periods

#	H1-Component	H2-Component	SF
1	RSN18397_21401069_NPMPBHHE.AT2	RSN18397_21401069_NPMPBHHN.AT2	158.68
2	RSN1320_CHICHI_ILA016-N.AT2	RSN1320_CHICHI_ILA016-W.AT2	8.08
3	RSN268_VICT_SHP010.AT2	RSN268_VICT_SHP280.AT2	14.92
4	RSN8487_PARK2004_NPMPBHNE.AT2	RSN8487_PARK2004_NPMPBHNN.AT2	24.72
5	RSN2782_CHICHI.04_HWA034E.AT2	RSN2782_CHICHI.04_HWA034N.AT2	53.68
6	RSN1166_KOCAELI_IZN090.AT2	RSN1166_KOCAELI_IZN180.AT2	5.78
7	RSN1454_CHICHI_TAP090-E.AT2	RSN1454_CHICHI_TAP090-N.AT2	6.56
8	RSN1859_YOUNTVL_1445A090.AT2	RSN1859_YOUNTVL_1445B360.AT2	117.23
9	RSN1327_CHICHI_ILA035-E.AT2	RSN1327_CHICHI_ILA035-N.AT2	10.91
10	RSN1316_CHICHI_ILA012-N.AT2	RSN1316_CHICHI_ILA012-W.AT2	8.52
11	RSN1566_CHICHI_TTN010-E.AT2	RSN1566_CHICHI_TTN010-N.AT2	22.92
12	RSN6003_SIERRA.MEX_1924A360.AT2	RSN6003_SIERRA.MEX_1924B270.AT2	100.84
13	RSN1563_CHICHI_TTN007-E.AT2	RSN1563_CHICHI_TTN007-N.AT2	27.08
14	RSN11114_40187964_NCJPCHNE.AT2	RSN11114_40187964_NCJPCHNN.AT2	471.30
15	RSN1564_CHICHI_TTN008-E.AT2	RSN1564_CHICHI_TTN008-N.AT2	19.46
16	RSN921_BIGBEAR_PSA090.AT2	RSN921_BIGBEAR_PSA360.AT2	15.67
17	RSN9555_10410337_14028090.AT2	RSN9555_10410337_14028360.AT2	169.06
18	RSN8746_40204628_BKBDMHLE.AT2	RSN8746_40204628_BKBDMHLN.AT2	275.83
19	RSN1348_CHICHI_ILA064-N.AT2	RSN1348_CHICHI_ILA064-W.AT2	16.49
20	RSN1628_STELIAS_059V2090.AT2	RSN1628_STELIAS_059V2180.AT2	5.06